A Study of Heat and Mass Transfer in Porous Sorbent Particles

by

Nagendra Krishnamurthy

Dissertation submitted to the faculty of Virginia Polytechnic Institute and State University in partial fulfillment of the requirements for the degree of

Doctor of Philosophy
in
Mechanical Engineering

Danesh K. Tafti – Chair
Thomas E. Diller
Clinton L. Dancey
Kenneth S. Ball
David F. Cox

June 19, 2014
Blacksburg, Virginia, USA

Keywords: Immersed boundary method, Conjugate heat transfer, Porous media, Reaction-diffusion system, Heat and species diffusion, Surface adsorption kinetics

Abstract

A Study of Heat and Mass Transfer in Porous Sorbent Particles

Nagendra Krishnamurthy

This dissertation presents a detailed account of the study undertaken on the subject of heat and mass transfer phenomena in porous media. The current work specifically targets the general reaction-diffusion systems arising in separation processes using porous sorbent particles. These particles are comprised of pore channels spanning length scales over almost three orders of magnitude while involving a variety of physical processes such as mass diffusion, heat transfer and surface adsorption-desorption. A novel methodology is proposed in this work that combines models that account for the multi-scale and multi-physics phenomena involved. Pore-resolving DNS calculations using an immersed boundary method (IBM) framework are used to simulate the macro-scale physics while the phenomena at smaller scales are modeled using a 'sub-pore modeling' technique.

The IBM scheme developed as part of this work is applicable to complex geometries on curvilinear grids, while also being very efficient, consuming less than 1% of the total simulation time per time-step. A new method of implementing the conjugate heat transfer (CHT) boundary condition is proposed which is a direct extension of the method used for other boundary conditions and does not involve any complex interpolations like previous CHT implementations using IBM. Detailed code verification and validation studies are carried out to demonstrate the accuracy of the developed method.

The developed IBM scheme is used in conjunction with a stochastic reconstruction procedure based on simulated annealing. The developed framework is tested in a two-dimensional channel with two types of porous sections – one created using a random assembly of square blocks and another using the stochastic reconstruction procedure. Numerous simulations are performed to demonstrate the capability of the developed framework. The computed pressure drops across the porous section are

compared with predictions from the Darcy-Forchheimer equation for media composed of different structure sizes. The developed methodology is also applied to CO_2 diffusion studies in porous spherical particles of varying porosities.

For the pore channels that are unresolved by the IBM framework, a sub-pore modeling methodology developed as part of this work which solves a one-dimensional unsteady diffusion equation in a hierarchy of scales represented by a fractal-type geometry. The model includes surface adsorption-desorption, and heat generation and absorption. It is established that the current framework is useful and necessary for reaction-diffusion problems in which the adsorption time scales are very small (diffusion-limited) or comparable to the diffusion time scales. Lastly, parametric studies are conducted for a set of diffusion-limited problems to showcase the powerful capability of the developed methodology.

Dedicated to amma and aNNa

Acknowledgements

First of all, I would like to whole heartedly thank my advisor Dr. Danesh Tafti. He has been an enormous source of encouragement and support through the four year period. He has always had the patience to listen to me, even when we are not on the same page on things, and gave me the freedom to pursue my ideas. He has been a great source of knowledge and inspiration to me, and has taught me most of what I know about research and many other things about life in general. I will forever be indebted to him for taking me under his wing, and guiding and motivating me to do things the best way I probably could. I would like to thank him again, for all his efforts – if not for him, this work would not have been possible.

I also thank Dr. Thomas Diller, Dr. Clinton Dancey, Dr. Kenneth Ball and Dr. David Cox for taking time off their busy schedules to be on my committee and reviewing my work.

This work was performed as part of the National Energy Technology Laboratory's Regional University Alliance (NETL-RUA), a collaborative initiative of the NETL. This technical effort was performed under the RES grant number 4000.2.683.062.002/632. The research grant is gratefully acknowledged.

My colleagues in the lab through these four years – Pradeep, Sai, Naresh, Sunil, Amit, Kamal, Vivek (Sethapati), Surya, Sukhjinder, Vivek (Kumar), Handan, Husam, Deepu, Ravishankar, Long, Keyur, Joseph, Junwoo and Andrew have all helped me through the numerous technical arguments and brainstorming sessions we have had. I thank them all for making the lab a wonderful place to be working in. I would like to extend a special thanks to Kamal and Amit for teaching me aspects of parallelization, unix and helping with a lot of the code development ideas.

My stay in Blacksburg has been a particularly enriching experience and the times I have spent outside of the lab have greatly helped me shape myself into the person I am today. In the basketball group,

Cricket club at Virginia Tech (CCVT), Tang Soo Do Karate Organization (TSDKO) and New River Tang Soo Do (NRTSD), the 56ers, Asha – I have met many fantastic people and shared many unforgettable moments. I will always cherish these experiences and would like thank everybody who was part of this. Mahesh, my apartment mate for three years, deserves special credit for bearing with me and making our home the best place I could have wished for during my PhD.

Now, a few words for my close friends and family members who have stuck with me for all these years. *Niket* and *Bhajay*, both classmates from college, helped me get through the initial stages of my life as a graduate student which was, without a question, very hard and challenging to say the least. *Chikki*, *Karthik* and *TS* – all talked to me for hours together when I needed it the most, and inculcated the belief in me that I could indeed go the distance. They pushed and nudged, scolded, encouraged – did whatever it took to keep me on the path till this journey was complete. My brother – *Guru* – and my cousin – *Santhosh*, both on numerous shared their experiences on numerous occasions prepping me for the yet unknown, big things ahead in life. Last but not the least, I am blessed to have the selfless love, support and encouragement from my family – most of all from my wonderful parents and my wife *Sindhu* – all of them have spoilt me so much, it just feels like that's how it was all supposed to be anyway! The intangibles that these people and many, many more, whose names I have missed here provided, I do not have enough words to thank them all – just the feeling of being truly lucky in every sense of the word!

Table of Contents

Abstract ii

Dedication iv

Acknowledgements v

Table of Contents vii

List of figures xi

List of tables xvi

Chapter 1 Introduction 1

Chapter 2 A new approach for conjugate heat transfer problems using immersed boundary method for curvilinear grid based solvers 5

2.1 Abstract 5

2.2 Introduction 6

2.3 Nomenclature 9

2.3.1 English symbols 9

2.3.2 Greek symbols 10

2.3.3 Subscripts 11

2.3.4 Superscripts 12

2.3.5 Miscellaneous 12

2.4 Numerical methodology 12

2.5 Immersed boundary framework 14

2.5.1 Search-locate and interpolate (SLI) algorithm 14

2.5.2 Interface tracking 17

2.5.3 Definition of node types 17

2.5.4 Assigning node types 18

2.5.5 Node identification: Radial swirler in an annular combustor 19

2.5.6 Setting of boundary conditions at IB nodes 20
2.5.7 Conjugate heat transfer treatment 22
2.5.8 Implementation in a fractional-step algorithm 24
2.6 Results 28
2.6.1 Computational overhead and parallel scalability 28
2.6.2 Rotational flow between coannular cylinders 30
2.6.3 Uniform flow over stationary cylinder 32
2.6.4 Uniform flow over an oscillating cylinder 34
2.6.5 Conjugate heat transfer through developing micro-channel flows 34
2.7 Conclusions 36
Chapter 3 Flows Through Reconstructed Porous Media Using Immersed Boundary Methods 61
3.1 Abstract 61
3.2 Introduction 61
3.3 Nomenclature 65
3.3.1 English symbols 65
3.3.2 Greek symbols 66
3.3.3 Subscripts 66
3.3.4 Superscripts 66
3.4 Methodology 67
3.4.1 Fluid flow solver 67
3.4.2 Immersed boundary method 68
3.4.3 Stochastic reconstruction of porous media 70
3.5 Results and Discussion 72
3.5.1 Validation 72
3.5.2 Flow through porous channels 74

3.5.3 CO_2 diffusion through porous spherical particles 78
3.6 Influence of stochasticity on saturation times 79
3.7 Summary and Conclusions 79
Chapter 4 A Sub-pore Model for Multi-Scale Reaction-Diffusion Problems in Porous Media 95
4.1 Abstract 95
4.2 Introduction 96
4.3 Methodology 98
4.3.1 Elements of sub-pore geometry 98
4.3.2 Modeling macro-pore transport 105
4.3.3 Modeling sub-pore transport 109
4.3.4 Coupling schemes 115
4.3.5 Numerical implementation details 116
4.3.6 Assumptions 120
4.4 Sub-pore methodology application 121
4.5 Macro-pore/sub-pore interchangeability 123
4.6 Reaction-diffusion in porous circular particle 124
4.6.1 Pure diffusion 126
4.6.2 Pure adsorption 126
4.6.3 Canonical cases 128
4.6.4 CO_2 adsorption in amine-impregnated meso-porous silica 129
4.6.5 Base simulation – Diffusion-limited case 132
4.6.6 Effect of sub-pore model 134
4.6.7 Parametric studies 136
4.7 Summary and conclusions 138
Chapter 5 Summary and Conclusions 170

Bibliography 173

List of figures

Figure 2.1 A two-dimensional example of transformation of two arbitrary points x_1 and x_2 from physical coordinates to computational coordinates with respect to Ω_c 38

Figure 2.2 Identifying the node types in a curvilinear grid topology - (a) a body-fitted 5 block geometry for a circular domain, (b) zoomed-in view of node types identified for a conjugate heat transfer case 39

Figure 2.3 (a) A CAD representation of the radial swirler geometry; (b), (c) the fluid IB nodes assigned on an annular non-orthogonal grid 40

Figure 2.4 Dirichlet condition implementation involving the use of a single probe in the normal direction. The distances d_{IB} and d_{p1} are both measured from the immersed boundary 41

Figure 2.5 Neumann condition implementation with use of two probes both placed along the normal direction. All the distances d_{IB}, d_{p1} and d_{p2} are measured from the immersed boundary 42

Figure 2.6 Conjugate heat transfer treatment with use of probes and mirror probes. Distances are again measured from the immersed boundary and the mirror probes mp1 and mp2 are located at the same distance as p1 and p2 (that is at d_{p1} and d_{p2}, respectively). The gray and the blue circles in (b) represent the interpolation nodes used in the solid and fluid regions, respectively 43

Figure 2.7 Definition of domain types for (a) non-CHT and (b) CHT cases 44

Figure 2.8 Close-up view of the near wing domain decomposition showing the spread of the IB over multiple blocks on the background grid 45

Figure 2.9 Strong scaling performance of the implementation for a flow simulation involving bat flight aerodynamics 46

Figure 2.10 Coannular cylinder geometry used for code verification 47

Figure 2.11 L_2 error norms computed at various grid levels for application of velocity, constant temperature, constant heat flux and conjugate heat transfer boundary conditions at the immersed boundary 48

Figure 2.12 Temperature profiles obtained for rotational flow simulations with CHT boundary condition between coannular cylinders using different probe distances ranging from 0.6-1.4 Δp 49

Figure 2.13 Pressure coefficient distribution around the cylinder surface in the steady regime ($ReD \leq 40$). $\theta = 0$ represents the stagnation point. 50

Figure 2.14 Nusselt number variation for constant wall temperature case at different Reynolds numbers. For unsteady regime, the averaged Nusselt number value is plotted. 51

Figure 2.15 Local distribution of time-averaged Nusselt number computed around the cylinder surface for $Re_D = 120$. $\theta = 0$ represents the stagnation point. 52

Figure 2.16 Contour plots of vorticity for (a) low amplitude $A = 0.199$ and (b) high amplitude $A = 0.696$. The higher oscillation amplitude case shows a change in the vortex shedding pattern resulting from the change in sign in the overall energy transfer 53

Figure 2.17 Comparison of the variation of lift profiles obtained with time for the higher amplitude case at $Re_D = 200$ 54

Figure 2.18 A schematic of the problem geometry used along with the dimensions and the cross-flow directional grid distribution 55

Figure 2.19 Comparison of local Nusselt number distributions computed on two grid levels - $\Delta = 0.04D_i$ and $0.02D_i$ with the results of Nonino et al. [43] for a flow through thick-walled micro-channel ($Re_D = 50$) 56

Figure 2.20 Effect of increasing Reynolds numbers on the local Nusselt number distribution. All calculations are performed at the finer grid level ($\Delta = 0.02D_i$) 57

Figure 3.1 A schematic representation of the solid node, IB node and its probe for a circular IB surface 81

Figure 3.2 A 2-D reconstruction with porosity of 0.75 and average structure size of 0.25 generated on a 200×200 grid (black represents solid region) 82

Figure 3.3 Distribution of pressure coefficients obtained around the cylinder surface at various Reynolds numbers for the stationary cylinder 83

Figure 3.4 Schematic representation of the porous channel geometry 84

Figure 3.5 Porous channel geometry used for the grid sensitivity study showing the stream-wise velocity contour 85

Figure 3.6 Comparison of u velocity profiles obtained at the three grid levels at (a) section 1 and (b) section 2..... 86

Figure 3.7 Enlarged views of realizations obtained using stochastic reconstruction procedure for dp values of (a) 0.25, (b) 0.50 and (c) 1.00. The porosity for each of these cases is fixed at $\epsilon = 0.85$. 87

Figure 3.8 Comparison of pressure drops from simulations and Darcy-Forchheimer equation for porous channel constructed using square blocks 88

Figure 3.9 Comparison of pressure drops from simulations and Darcy-Forchheimer equation for porous channel constructed using stochastic reconstruction..... 89

Figure 3.10 A 3-D porous spherical particle of diameter 100 microns and porosity of 0.45..... 90

Figure 3.11 Computed diffusion times for porous spherical particles of varying porosities 91

Figure 4.1 A representation of the (a) pore branching structure and (b) hierarchical system composed of cylindrical structures used in the sub-pore system 140

Figure 4.2 A single cell representation within the sub-pore system 141

Figure 4.3 A schematic representing the cells within the sub-pore system and the interaction with the macro-pore system 142

Figure 4.4 A representative sketch of the problem set-up used in all the calculations. The colored region represents the solid volume. The particle shape is only representative – in the presented calculations, both circular and square shaped particles have been used)..... 143

Figure 4.5 The macro-pore geometries used for simulation (a) with macro-pores – the larger channels being modeled as macro-pores and (b) without macro-pores – both the channel sizes are modeled in the sub-pore system 144

Figure 4.6 Concentration profiles obtained for (a) the entire particle pore space, (b) all the larger channels (2 microns) and (b) all the smaller channels (1 micron) 145

Figure 4.7 Contributions of channels of different sizes to the overall volume and area of the sub-pore geometry 146

Figure 4.8 Concentration profiles obtained from the pure diffusion simulation plotted for (a) the full simulation time (b) the first 10 ms and (c) the full simulation time, averaged on a per-level basis 147

Figure 4.9 Adsorption profiles obtained for three different value of E_{des} while keeping E_{ads} constant in pure adsorption calculations 148

Figure 4.10 Adsorption profiles obtained for different values of E_{ads} and E_{des} while keeping the ΔE constant 149

Figure 4.11 Adsorption profiles obtained from pure adsorption calculations for simulations in the three different regimes 150

Figure 4.12 Comparison of transient profiles for (a) concentration and (b) adsorption for the three canonical cases (in (b), the dashed lines with hollow symbols are from the corresponding pure adsorption simulations presented earlier) 151

Figure 4.13 Area and volume contributions of a sub-pore geometry with $n_b = 10$, compared to the geometry used in earlier calculations with $n_b = 5$ 152

Figure 4.14 Averaged concentration levels in different regions of the particle pore space for the first 300 ms of simulation time 153

Figure 4.15 CO_2 adsorption profile obtained for pure adsorption calculation using the experimental rate equation proposed by Lee et al. [106] 154

Figure 4.16 Transient profiles of (a) concentration and (b) adsorption obtained for the base simulation for full simulation time 155

Figure 4.17 Transient profiles of (a) concentration and (b) adsorption plotted for the initial 50 ms for the base simulation 156

Figure 4.18 Transient profiles of (a) concentration and (b) adsorption averaged on a per-level basis for the full simulation time for the base simulation 157

Figure 4.19 Transient profiles of (a) concentration and (b) adsorption averaged on a per-level basis for the initial 50 ms for the base simulation 158

Figure 4.20 Transient profiles of concentration in the entire particle pore space for simulations with different mechanisms excluded for (a) the full simulation time and (b) the first 50 ms 159

Figure 4.21 Adsorption profiles obtained for cases 3 and 4 for (a) full simulation time and (b) first 50 ms 160

Figure 4.22 Transient profiles of (a) concentration and (b) adsorption obtained for different values of ΔE 161

Figure 4.23 Transient profiles of (a) concentration and (b) adsorption obtained for three different values of ambient temperature 162

Figure 4.24 Transient profiles of (a) concentration and (b) adsorption obtained for different values of ambient pressure 163

List of tables

Table 2.1 Comparison of drag coefficients C_D and lengths of recirculation zones L_w at different Reynolds numbers for uniform flow over a stationary cylinder 58

Table 2.2 Comparison of Strouhal numbers computed at different Reynolds numbers for flow over a stationary cylinder in the unsteady regime 59

Table 2.3 Computed Nusselt number values for constant temperature and heat flux boundary conditions at the cylinder surface 60

Table 3.1 List of coefficients of drag and wake lengths computed for uniform flow over a stationary cylinder at various Reynolds numbers 92

Table 3.2 Strouhal numbers obtained at different Reynolds numbers and the comparison with existing experimental and numerical results 93

Table 3.3 Non-dimensional pressure drops observed across the porous section 94

Table 4.1 Parameters used for sub-pore geometry creation for the circular porous particle 164

Table 4.2 Range of simulation parameters used in the different calculations 165

Table 4.3 Simulation parameters used in the pure diffusion calculation 166

Table 4.4 Range of simulation parameters used in the pure adsorption calculations 167

Table 4.5 Approximate time scales and regimes for different combinations of activation energies 168

Table 4.6 Comparison of saturation times by using extrapolation with the observed values for pure diffusion 169

Chapter 1
Introduction

Understanding the physics in processes involving porous media has generated tremendous interest from researchers due to their use in a variety of technologies. A technology that has found tremendous success is the use of porous particles for gas purification. In these processes, a stream of gaseous mixture is passed through sorbent particles which show preferential adsorption capacity towards the particular species that is to be separated. Adsorption, being a surface phenomenon, requires a large amount of surface area to exhibit high separation capacities and hence the particles used for this purpose are usually highly porous. Other desirable properties for sorbent material are selectivity towards certain species of interest, the adsorption/desorption kinetics, regeneration capacity and the overall sorbent costs [1]. One of the important applications of this technology is its use in separating carbon dioxide (CO_2) from flue gas streams as part of the carbon sequestration process. Among the many solid sorbents used for carbon capture, the use of amine-based adsorbents is of particular interest to this study. Apart from separation of CO_2, the solid sorbent technology is also used in a number of other bulk separation processes such as removal of suphur dioxide [2] and alkali vapor adsorption [3].

This work is primarily concerned with the computational modeling of heat and mass transfer in porous particles, a problem inherent to solid sorbent based separation processes. In doing so, there are numerous challenges are identified:

- the porous particles exhibit very intricate microstructural contours, hence a way of dealing with these complex surfaces is necessary
- the structures entailed in the particles also show a large range of length scales – usually 3-4 orders of magnitude, thus rendering the system to be multi-scale in nature

- the underlying physics in the system is governed by multiple phenomena – transport of heat and mass, and surface reaction of the adsorbate species with the adsorbent porous surface
- the possibility of widely differing time scales owing to the dominant physical mechanisms or the local length scale.

The main aim of this work is to develop the numerical tools necessary to study this complex multi-scale, multi-physics problem to quantify the flow of heat and mass into the porous particles, coupled with the reaction kinetics. The following are the major research questions answered as part of the current work:

1. *Is it possible to create a single framework that can account for all the multitude of scales and physical mechanisms?*

The porous geometry contained in any porous medium is generally composed of intricate microstructural contours. Additionally, the difference between the largest to the smallest channel sizes usually spans 3-4 orders of magnitude. The dominant physics at the different scales are also expected to be different. A two pronged approach is hence proposed in this work to account for the different length scales – directly resolve the larger channels and model any of the unresolved smaller scales. This will indeed allow the use of a single framework wherein the most relevant physical mechanisms are accounted for in the larger and smaller pore channels.

2. *How does one account for the complex microstructural nature of the porous particles and be able to perform accurate simulations through such surface contours?*

Even while only the larger channels are resolved directly, the complex nature of the geometry in these channels prohibits the use of traditional numerical techniques. To overcome this issue, a non-boundary conforming approach – the immersed boundary method (IBM) – will be used. IBM allows computational modeling of flow and heat transfer around arbitrarily shaped surfaces with relative ease owing to the simplified and straight-forward grid generation process.

3. *Can it be ensured that the porous geometries used at least for the larger pores that are directly resolved are representative of the real sorbent particles?*

In order to ensure use of realistic porous media geometries, a stochastic reconstruction procedure will be employed. This is an alternative to using experimentally obtained images directly, which are usually very hard to obtain, especially complex three-dimensional solids. Instead, two-dimensional experimental images can be used to extract statistical descriptors that can subsequently be used in conjunction with the stochastic reconstruction technique to obtain porous geometries. A combination of IBM and stochastic reconstruction will be used to simulate the physics occurring at the larger channels in the porous particles.

4. *Lastly, what are the physical mechanisms that govern the smaller scales and how can we account for these?*

A new methodology to include the effects of any unresolved smaller scales and the dominant physical mechanisms thereof will be developed. Along with transport of mass and energy, the surface adsorption effects become important as the smaller channels usually account for most of the surface area available in the porous medium. A hierarchical network of pore channels that are unresolved by the IBM framework will be created within which the effects of the aforementioned physical phenomena will be modeled using simplified one-dimensional governing equations.

The rest of the dissertation is presented in three independent chapters. In the second chapter, details of the IBM framework developed and the related test simulations are discussed. This includes the implementation in a curvilinear grid framework, and a new approach to solving conjugate heat transfer problems using IBM. In chapter three, the developed IBM framework is applied to realistic porous media geometries that are created using stochastic reconstruction techniques. In chapter four, a novel sub-pore modeling methodology is described which models the unresolved scales and the relevant physics. These chapters correspond to the last three research questions and are written in an independent fashion given

that the contents are mostly non-overlapping. Hence, every chapter has a separate introduction and conclusions section. The references however are merged into a single section to avoid repetitions and are presented at the end of the dissertation.

The work performed as part of this dissertation has resulted in peer-review journal publications and the details are as follows:

- "Flows Through Reconstructed Porous Media using Immersed Boundary Methods", K. Nagendra and D.K. Tafti, Journal of Fluids Engineering, 136 (4), 040908, 2014.
- "A Novel Approach for Conjugate Heat Transfer Problems Using Immersed Boundary Method for Curvilinear Grid Based Solvers", K. Nagendra and D.K. Tafti, Journal of Computational Physics, 267, 225-246, 2014.
- "A Sub-pore Model for Multi-Scale Reaction-Diffusion Problems in Porous Media", K. Nagendra and D. K. Tafti (manuscript under preparation).
- "Modeling CO_2 diffusion and adsorption in mesoporous silica particles", K. Nagendra and D. K. Tafti (manuscript under preparation).

Chapter 2

A new approach for conjugate heat transfer problems using immersed boundary method for curvilinear grid based solvers[1]

2.1 Abstract

Use of immersed boundary method (IBM) based techniques have helped considerably in easing the grid generation process in flows involving complex geometries and/or large boundary movements. Body fitting grid based techniques still, however, are advantageous in terms of accuracy and efficiency. In this work, we have developed an IBM scheme applicable to curvilinear coordinates, aiming at taking advantage of both the methodologies. The framework uses efficient algorithms for search, locate, and interpolate operations. A new method of implementing the conjugate heat transfer (CHT) boundary condition is proposed which is a direct extension of the method used for other boundary conditions and does not involve any complex interpolations like previous CHT implementations using IBM. The developed scheme is shown to be applicable to complex geometries on curvilinear grids, while also being very efficient, consuming less than 1% of the total simulation time per time-step. Very good scalability on massive computations is demonstrated using strong scaling study up to 1024 cores. Detailed code verification process is undertaken to show that the method is second-order accurate for both the velocity and temperature fields for all the boundary conditions considered. Further, validation studies involving uniform flow over stationary and oscillating cylinders are carried out to demonstrate the accuracy of the developed method. Lastly, simulations are performed to study flow and conjugate heat transfer through thick-walled micro-channels using body-fitted background grids and the results are shown to be in excellent agreement with previously published results.

[1] Reprinted from Journal of Computational Physics, vol. 267, Nagendra, K., Tafti, D.K. and Viswanath, K., "A new approach for conjugate heat transfer problems using immersed boundary method for curvilinear grid based solvers", pp. 225-246, with permission from Elsevier.

2.2 Introduction

In the last couple of decades, the use of boundary non-conforming techniques for computational fluid dynamics problems has gained considerable popularity, owing mainly to the versatile capabilities that such implementations offer in comparison to traditional CFD codes. The time spent on generation of body-fitting meshes requires a huge amount of user input for complex geometries. For moving boundary problems, the structured body-fitting grids require complex grid deformations and/or re-meshing algorithms, most of which still have limited allowable range of boundary movement. While unstructured solvers are better in terms of ease of grid generation and re-meshing, they are much harder to implement and require large amounts of book-keeping and memory usage. In contrast, the use of boundary non-conforming formulations allows simulations of fluid flow around bodies with complex features, large movements and surface deformations on a fixed background mesh with minimal overhead in setup.

Solvers based on such methodologies have the solid boundary "immersed" in a background mesh and generally utilize a series of special treatments applied near the solid surface. These methods are commonly termed immersed boundary methods (IBM). The idea originated from the work of Peskin [4] where this method was used to simulate blood flow through heart valves using a fixed Cartesian background grid. Following this work, several modifications and improvisations to this method have been proposed over the years showcasing its wide range of applicability. A wealth of literature is available on the range of capabilities that can be developed using immersed boundary techniques [5]. Here, we first present a brief review of the different types of implementations available. The implementations mainly vary in the way the boundary conditions are applied. In general, the use of IBM can be thought of as a modification applied to the governing Navier-Stokes equations. The exact nature of this modification distinguishes the different schemes from each other.

A widely used approach is the use of a forcing function – usually a Dirac delta function – as a source term in the momentum equations. Peskin and coworkers utilized a forcing function that is spread across a few

cells neighboring the immersed surface [4, 6-8]. In fact, numerous applications exist in the literature, especially for flows with elastic boundaries such as fluid-structure interaction problems involving blood flow through arteries, for which this approach is a natural choice. One drawback of such formulations, however, is the smearing of the boundaries due to the spreading nature of the forcing function. While this may not be an issue for elastic boundaries, this increases the grid resolution requirement substantially for flows with rigid immersed surfaces.

This issue can be avoided by directly computing the forcing function to be applied from the discretized momentum equations and using it as a source term for the nodes that lie in the immediate vicinity of the immersed boundary. This approach was pioneered by Mohd-Yusof and coworkers [9, 10] who proposed a second-order accurate scheme based on a locally dependent interpolation stencil. This method is applicable to sharp solid interfaces and does not suffer from the blurring which may occur in a continuous forcing approach. Several improvements have been proposed since, mainly with an aim of developing a general methodology applicable to wider spectrum of problems including arbitrarily shaped 3D surface contours with deformation and/or movement [11-14].

Another set of works that falls into this category is the cut-cell techniques used prominently by Udaykumar and collaborators [15, 16]. The methodology adopted in these works is to perform simulations on control volumes that are reshaped close to the immersed surface, thus simulating a sharp interface. The method has been successfully employed for a variety of problems both in 2D and 3D geometries, though it should be noted that the 3D implementations are not trivial due to complex polyhedral cells that are formed as a result of the cut-cell procedure.

The approaches discussed thus far focus on the use of Cartesian grids as background mesh due to the simplicity of mesh generation. In fact, that was one of the driving factors for the use of immersed boundary methods. While this is true in a number of situations, the use of a non-orthogonal mesh as the

background grid may also be desirable in some scenarios. Examples for these cases are problems involving internal flows through domains of relatively simple outer boundaries (non-orthogonal) while there are complex internal structures either stationary or moving within these domains. For the overall domain, it would be beneficial to use a curvilinear, body-fitted discretization scheme because of better computational efficiency as well accuracy in such cases, while still utilizing the advantages that the IBM schemes offer for the complex internal solid structure. There already exist a few works in the literature that have focused on developing such a hybrid framework [17, 18] including applications to pulsatile flows through bileaflet heart valve [19] and fluid-structure interaction problems [20, 21]. These are essentially extensions of the sharp interface method of Gilmanov and Sotiropoulos [14] to curvilinear coordinates. An important step in these implementations is tracking of the immersed boundary and is commonly known as the interface tracking problem. Borazjani et al. [22] note that this identification accounts for close to 5% of the total computational cost per time-step (for a simulation involving 10 million grid nodes and 2048 surface elements).

Extension of the immersed boundary methodology to the solution of energy equation is conceptually very similar. Numerous works are available in literature for the two commonly used boundary conditions – constant temperature (Dirichlet) and constant heat flux (Neumann) [18, 23-25]. The implementation of these two boundary conditions is a natural extension from the formulation developed for momentum equation solution. However, in heat transfer phenomena another commonly encountered situation is the need to solve the energy equation inside the solid, along with the fluid region. This phenomenon termed "conjugate heat transfer" (CHT) is in fact physically more realistic, when the conduction within the solid cannot be assumed to be infinitely faster compared to the fluid region. This boundary condition is a combination of the Dirichlet and Neumann boundary conditions which are both to be satisfied at the immersed surface. Modeling such a boundary condition requires the knowledge of temperature field on

both sides of the immersed surface. In contrast, both the velocity and constant temperature/heat flux boundary conditions require information of temperature field only on the fluid side.

One of the first such implementation of a CHT scheme using IBM was by Iaccarino and Moreau [26]. Iaccarino and Moreau applied the method to both natural and forced conjugate heat transfer problems using a RANS model. More recently, Kang and coworkers [27] developed an interpolation technique for the conjugate heat transfer implementation and applied the methodology to turbulent flows which are buoyancy dominated. This method involved interpolations around a disjointed fluid-solid interface to solve for the conjugate heat transfer problem. The accuracy of the scheme was also observed to drop due to the limited size of the interpolation scheme and stencil size used for the reconstruction. In this work, we aim to develop an IBM scheme for CHT problems that is formulated as a natural extension of the Dirichlet and Neumann boundary conditions without requiring any complex interpolations. Hence the CHT boundary condition is expected to present the same level of accuracy (second order) as Dirichlet or Neumann boundary conditions.

Summarizing, the major aims of the current study are: (1) to develop an efficient immersed boundary methodology for a curvilinear grid based solver and (2) to formulate an accurate and straight-forward implementation for conjugate heat transfer problems using IBM. In this paper, we present the details of the formulation developed for this purpose. A couple of example applications are presented to demonstrate the utility of the developed framework. The accuracy of the developed method is verified by using an analytical solution. This is followed by a series of validation studies to confirm the accuracy of the different capabilities.

2.3 Nomenclature

2.3.1 English symbols

A area

d	distance
D	diameter
L	length
n	surface normal (direction)
Nu	Nusselt number
p	pressure
p'	pressure correction
Pr	Prandtl number
q''	heat flux
R	radius
Re	Reynolds number
St	Strouhal number
t	time
T	temperature
T_c	characteristic temperature
u	velocity
U	cell-face flux

2.3.2 Greek symbols

Γ	surface entity

Δ grid size

Δ_p probe distance

κ thermal conductivity

μ absolute viscosity

ρ density

ϕ flow variable

Ω volume entity

2.3.3 Subscripts

BC boundary condition

c cell

e nearest element

f fluid

i inner wall

IB IB node

mp mirror probe

n node

o outer wall

p probe

ref reference value

s solid

w wall

2.3.4 Superscripts

$*$ dimensional value

2.3.5 Miscellaneous

a, b, g computational space coordinates

i, j, k structured grid indices

r, θ radial coordinates

x, y, z Cartesian coordinates

(bold) vector quantities

$\sim$ (overhead) intermediate value

$\mathfrak{F}(\cdot)$ time-stepping operator

$\mathfrak{G}(\cdot)$ boundary condition operator

$\mathfrak{M}(\cdot)$ mass conservation operator

2.4 Numerical methodology

All the calculations are performed in an in-house code – GenIDLEST [28] (Generalized Incompressible Direct and Large Eddy Simulation of Turbulence) – a parallelized fluid flow solver developed for time-dependent flow and heat transfer calculations. GenIDLEST solves the incompressible Navier-Stokes equations in generalized coordinate framework and is capable of handling temperature dependent property variations. For brevity, only the non-dimensional form of the governing equations abbreviated

using Einstein's index notation for low-speed constant property flows is given below. More details about the formulation can be found in [29, 30].

$$\frac{\partial u_i}{\partial x_i} = 0 \tag{2.1}$$

$$\frac{\partial u_i}{\partial t} + \frac{\partial}{\partial x_j}\left(u_i u_j\right) = -\frac{\partial p}{\partial x_i} + \frac{1}{Re}\left(\frac{\partial^2 u_i}{\partial x_j \partial x_j}\right) \tag{2.2}$$

$$\frac{\partial T}{\partial t} + \frac{\partial}{\partial x_j}\left(u_j T\right) = \frac{1}{Re \cdot Pr}\left(\kappa \frac{\partial^2 T}{\partial x_j \partial x_j}\right) \tag{2.3}$$

where the non-dimensionalizations are:

$$x_i = \frac{x_i^*}{L_{ref}^*};\ u_i = \frac{u_i^*}{u_{ref}^*}; t = \frac{t^* u_{ref}^*}{L_{ref}^*}; p = \frac{p^* - p_{ref}^*}{\rho_{ref}^* {u_{ref}^*}^2}; T = \frac{T^* - T_{ref}^*}{T_c^*};$$

$$Re = \frac{\rho_{ref}^* u_{ref}^* L_{ref}^*}{\mu_{ref}^*}; Pr = \frac{\mu_{ref}^* {C_p}_{ref}^*}{\kappa_{ref}^*}$$

The above equations are transformed to generalized coordinates and solved using a conservative finite-volume formulation on a non-staggered grid topology. The Cartesian velocities, pressure and temperature values are calculated and stored at the cell center, whereas the contra-variant mass fluxes are calculated and stored at the cell faces. For time integration, a projection method using second order predictor-corrector steps is employed. The predictor step calculates an intermediate velocity field and the corrector step calculates the updated divergence free velocity at the new time-step by solving a pressure-Poisson equation. Linear systems resulting in the implicit treatment of the momentum and energy equations, and the solution of the elliptic pressure equation are solved using a preconditioned BiCGSTAB method.

2.5 Immersed boundary framework

The proposed immersed boundary methodology is an extension of a scheme first proposed by Gilmanov and Sotiropoulos [14] to a curvilinear coordinate system on a non-staggered grid. In this implementation, no additional forcing term is used in the governing equations. Instead, solution to the governing equations is suitably modified at nodes that lie in the immediate vicinity of the immersed surface. The major steps in the implementation can be listed as follows: (1) identify the location of the immersed surface and determine which of the surrounding nodes are fluid and which are solid, (2) solve the governing equations at all nodes in the domain that are not in the immediate vicinity of the boundary and (3) at the nodes that are directly next to the IB, apply a special treatment to reflect the presence of an immersed surface.

2.5.1 Search-locate and interpolate (SLI) algorithm

Of the different tasks involved in our immersed boundary methodology, there are two general operations that are to be performed repetitively – relating an arbitrary Lagrangian point to the background Eulerian fluid grid and interpolating values onto this arbitrary point from known values at the background grid. Depending on the problem size, these tasks may need to be performed a large number of times every time-step and hence should be handled in an efficient manner. We use a search-locate and interpolate algorithm proposed originally by Allievi and Bermejo [31] for application in particulate flows for this purpose. This algorithm determines the cell in which an arbitrary Lagrangian point lies and also provides the weighting coefficients needed for tri-linear interpolation. Only a brief description of the algorithm is presented here – details of the full formulation and examples can be found in the original paper [31]. As the name suggests, the algorithm performs two main operations – identify the cell in which a given point lies (search-locate step) and compute the value of any variable of interest at a given point in the cell, provided the values are known at the surrounding vertices (interpolate step).

In order to determine whether a given point $\boldsymbol{x} = (x, y, z)$ lies within a hexahedral cell Ω_c, first the physical coordinates (x, y, z) are transformed into the computational space coordinates (a, b, g), defined with respect to the cell Ω_c. A two-dimensional example of the transformation is shown in Figure 2.1. It can be observed that the edges of the cell are represented by the lines $a = \pm 1$ and $b = \pm 1$ (and $g = \pm 1$ for the 3D case) in the local transformed coordinates. Hence, the point $\boldsymbol{x}$ lies within the bounds of the cell Ω_c only if the following locate condition is satisfied:

$$-1 \leq a, b, g \leq +1 \tag{2.4}$$

It follows that in the example provided, $\boldsymbol{x}_1$ lies within the cell whereas $\boldsymbol{x}_2$ is outside it.

The eight vertices that make up Ω_c are represented compactly as $\boldsymbol{x}_{\pm i, \pm j, \pm k}$, with the signed indices identifying the direction of the vertex in the structured grid framework. For example, in the 2D case shown in Figure 2.1, $\boldsymbol{x}_{-i,-j}$ represents the lower left vertex while $\boldsymbol{x}_{+i,+j}$ represents the upper right vertex. Using the widely used tri-linear interpolation function, the coordinates of location $\boldsymbol{x}$ can be expressed in terms of $\boldsymbol{x}_{\pm i, \pm j, \pm k}$'s and a set of computational space coordinates (a, b, g) that correspond to $\boldsymbol{x}$:

$$\boldsymbol{x}(a, b, g) = \frac{1}{8}\left(\begin{array}{c} \left\{\begin{array}{c} \left(\boldsymbol{x}_{-i,-j,-k}(1-a) + \boldsymbol{x}_{+i,-j,-k}(1+a)\right)(1-b) \\ + \\ \left(\boldsymbol{x}_{-i,+j,-k}(1-a) + \boldsymbol{x}_{+i,+j,-k}(1+a)\right)(1+b) \end{array}\right\}(1-g) \\ + \\ \left\{\begin{array}{c} \left(\boldsymbol{x}_{-i,-j,+k}(1-a) + \boldsymbol{x}_{+i,-j,+k}(1+a)\right)(1-b) \\ + \\ \left(\boldsymbol{x}_{-i,+j,+k}(1-a) + \boldsymbol{x}_{+i,+j,+k}(1+a)\right)(1+b) \end{array}\right\}(1+g) \end{array}\right) \tag{2.5}$$

It is easy to observe that the computational space coordinates of the vertices would be $\boldsymbol{x}_{\pm i, \pm j, \pm k} \equiv (\pm 1, \pm 1, \pm 1)$. Numerically, an iterative scheme is required, however, to invert the above function to determine the values of (a, b, g)'s. The Newton-Raphson method is employed for this purpose.

In the event that the locate condition mentioned earlier is satisfied, the obtained (a, b, g) values also can be directly used to compute interpolation factors for tri-linear interpolation. Assuming that the variable of interest is known at the eight vertex locations, we just replace $\boldsymbol{x}$ by the scalar value $\phi(\boldsymbol{x})$ and the vertex vectors $\boldsymbol{x}_{\pm i,\pm j,\pm k}$'s by the corresponding known values of the scalar variable at these locations $\phi_{\pm i,\pm j,\pm k}$. The simplified expression for the weights attached to each of the vertices will be:

$$\alpha_{\pm i,\pm j,\pm k} = \frac{(1 \pm a)(1 \pm b)(1 \pm g)}{8} \tag{2.6}$$

In case the locate condition is not satisfied (i.e., the location $\boldsymbol{x}$ does not lie within the cell Ω_c), then the SLI algorithm needs to perform the search-locate operation on other cells in the domain. Since the number of cells is likely to be large, an efficient way to determine the cell that is most likely to contain the location of interest is necessary. The output of the search-locate operation above gives a good estimate which neighboring cell is most likely to contain the location of interest. Since the obtained (a, b, g)'s are the cell based computational coordinates, on a structured grid we can use these to obtain the (i, j, k) indices of the next most likely cell. For example, if (i, j, k) are the indices of the currently search cell Ω_c and the values of a, b, g are all > 1, then the cell most likely to contain $\boldsymbol{x}$ would be $(i + 1, j + 1, k + 1)$. Similarly, if $a, b \leq -1$ while $-1 \leq g \leq 1$ would indicate the next cell is most likely $(i - 1, j - 1, k)$ and so on.

In summary, the described SLI algorithm provides an efficient algorithm of determining the indices of the cell in a structured grid where a given location $\boldsymbol{x}$ lies. Also, without any additional computations, the weighting factors for a tri-linear interpolation at $\boldsymbol{x}_p$ based on known surrounding vertex values can be determined. The steps in the SLI algorithm can be listed as follows:

1. Start with an initial guess for the cell Ω_c in which location $\boldsymbol{x}$ is likely to reside.

2. Iteratively determine the cell-based computational space coordinates (a, b, g) of $\boldsymbol{x}$ with respect to Ω_c.

3. Check if the location lies within Ω_c – if yes, go to 5; else, go to 4.

4. Change the guess cell Ω_c to be the next most likely cell based on the values of (a, b, g). Go to 2.

5. If desired, compute the tri-linear interpolation coefficients based on the values of (a, b, g).

2.5.2 Interface tracking

The first step in the proposed IBM scheme is the identification of the immersed surface represented in a Lagrangian fashion with respect to the background Eulerian grid. This identification step comprises of locating the individual triangular surface elements (or line segments in 2D) using the SLI algorithm described before. The centroid of every surface element is used as the Lagrangian marker representing the element and the background cell in which it lies is determined. This step is to be performed once at the beginning of the simulation for stationary immersed boundaries and at the beginning of every time-step for moving immersed boundaries. This is followed by assigning of node types to all the nodes in the calculation domain. Here, it should be noted that the term node is the same as a cell and the two terms are used interchangeably in the following descriptions.

2.5.3 Definition of node types

We define three primary types of nodes – fluid, solid and IB. The fluid and solid node definitions are trivial – any node that lies in the fluid region is a fluid node and if not, it is a solid node. An IB node, on the other hand, is any node that lies in the immediate vicinity of the immersed boundary.

For any non-CHT simulation, solution to the governing equations using the iterative solvers is necessary only at the fluid nodes. No solution is needed at the solid nodes, while at the IB nodes, values of the solution variables are obtained by applying the desired BC (discussed later) at the immersed boundary.

For CHT simulations though, the temperature field is solved both in the fluid and solid regions. Hence, IB node assignment is necessary on either side of the immersed boundary as opposed to only fluid side for non-CHT simulations. The solid nodes that lie directly next to the immersed boundary are called solid IB nodes.

For clarity on these definitions, a two-dimensional example of different node types for a CHT case is shown in Figure 2.2. The background mesh is a structured body-fitted circular grid with a concentric circular solid immersed in it. It is important to note that the fluid IB and solid IB nodes are the first set of nodes lying direct next to the immersed boundary. Outer set of fluid nodes (and solid nodes, for energy equation) are affected by the presence of the immersed boundary through their interaction with the fluid (and solid) IB nodes.

2.5.4 Assigning node types

As it is evident from the above definitions, the first task in node identification is to determine whether a given node is a fluid or solid node. It should also be noted that, by definition, all the IB (fluid and solid) nodes will lie in the immediate vicinity of the immersed boundary. Since the IB nodes exist only next to the immersed boundary, we restrict all our identification operations to the vicinity of the boundary. The following are the steps followed to assign node types:

1. For every surface element, define a stencil around the cell on the background grid containing the element centroid (identified during the interface tracking step). Determination of node type will be performed only for nodes that lie within this stencil. The stencil size is proportional to the relative size of the surface element with respect to the size of the cell in which it lies. For a locally resolved drag/heat transfer calculation on the immersed surface, it is necessary to have surface elements to be approximately the same size as the cells and in this case, the stencil size will be 3 nodes in every direction.

2. For every node in the stencil, identify the surface element closest to it. For this, the sign of the normal distance to this element computed based on the following dot product is used to determine whether the node lies towards the solid or fluid side:

$$d = (\boldsymbol{x_n} - \boldsymbol{x_e}) \cdot \hat{\boldsymbol{n}} = \begin{cases} \geq 0 & fluid \\ < 0 & solid \end{cases}$$

   where $\boldsymbol{x}_n$ and $\boldsymbol{x}_e$ are the coordinates of the node and the centroid of the nearest element, respectively and $\hat{\boldsymbol{n}}$ is the surface normal directing outwards from the element.

3. Next, of these nodes, all the fluid nodes that have at least one face-sharing neighboring solid node are marked as fluid IB nodes. Similarly, all the solid nodes that have at least one face-sharing neighboring fluid node are marked as solid IB nodes.

4. At this point, we have assigned node types to all nodes that lie close to the immersed boundary. For assigning node types to nodes that lie farther away from the IB, we use an efficient "burning algorithm" [32] which is applied recursively and can be summarized as follows: looping over all nodes of known type (solid or fluid), assign the same node type to any unassigned nodes that are its face-sharing neighbors; repeat this process for every such newly assigned node until no unassigned nodes are left in the domain.

2.5.5 Node identification: Radial swirler in an annular combustor

We look at a representative example to demonstrate the application of the described identification procedure to a realistic geometry involving complex features. For this purpose, we consider a radial swirler in an annular combustor. Here, a periodic section of this geometry consisting of one such swirler is chosen. A body-fitted non-orthogonal mesh is created to encompass the volume within the annular combustor while the swirler is modeled as an immersed surface. Figure 2.3 shows a CAD representation of the swirler geometry as well as the identified fluid IB nodes. The surface is triangulated using a total of

approximately 10^6 surface elements while the background mesh is composed of around 4×10^6 cells. It is observed that all the features of the swirler geometry have been correctly captured by the node identification method outlined in this section.

2.5.6 Setting of boundary conditions at IB nodes

In order for the outer nodes (both solid and fluid) to see the presence of an immersed boundary, the values of flow variables at the IB nodes need to be suitably modified. For this, depending on the type of boundary condition, a solution reconstruction procedure is used. Three types of boundary conditions are considered at the immersed boundary – Dirichlet, Neumann and conjugate heat transfer.

Similar to other sharp interface IBM schemes, to be able to reconstruct the solution at the IB nodes, we need to define probes which extend into the domain from the IB nodes. Solution variables are interpolated at the probe location using a tri-linear interpolation scheme and these values are used in conjunction with the desired boundary condition at the immersed boundary to obtain the IB node values. The obvious choice for the location of the probes is to choose them to lie along the surface normal direction further into the calculation domain. Mathematically, the probe location $\boldsymbol{x}_p$ for an arbitrary point $\boldsymbol{x}$ (can be either a fluid or solid IB node) in the vicinity of the IB is given by:

$$\boldsymbol{x}_p = \begin{cases} \boldsymbol{x} + \Delta_p\, \hat{\boldsymbol{n}} & fluid\ IB\ node \\ \boldsymbol{x} - \Delta_p\, \hat{\boldsymbol{n}} & solid\ IB\ node \end{cases} \tag{2.7}$$

where Δ_p is the distance of the probe from the IB node and $\hat{\boldsymbol{n}}$ is the surface normal.

In choosing the value of Δ_p, it must be ensured that the probe is far enough from the IB node not to be significantly affected by the IB node itself (in the interpolation) and yet, close enough for the near boundary assumptions to be valid. In spite of the possible curvilinear nature of the background grid, it is generally desirable that the grid distribution in the different directions is usually of roughly the same size

in the vicinity of the IB for a complex randomly oriented immersed surface. For such a case, a good approximation for Δ_p is the average cell size which is computed locally for every IB node. However, it is likely that for certain cases, a mesh with varying aspect ratios is used as the background grid. For such cases, the probe distance Δ_p can be calculated as the absolute value of the dot product of the IB surface normal and the longest diagonal of the IB cell. This is a more general definition which can account for varying grid distributions in different directions as well as the arbitrary nature of the IB orientation.

2.5.6.1 Dirichlet condition

Interpolated values at probe locations are used for implementing the desired boundary condition at all IB nodes. The probe location, as stated earlier, is chosen to be at a cell distance away along the surface normal direction. Figure 2.4 illustrates the implementation of Dirichlet boundary condition in our framework. Interpolated value of the flow variable ϕ_{p1} at the probe location is obtained using the tri-linear interpolation coefficients obtained using the SLI algorithm. Nodes that are part of the interpolation stencil are highlighted in Figure 2.4 (b), using blue circles. A second-order accurate formulation for ϕ_{IB} is then obtained by using the Taylor expansions for ϕ_{IB} and ϕ_{p1} defined about the value at the wall ϕ_{BC} and eliminating the first gradient.

$$\phi_{IB} = \frac{d_{IB}\phi_{p1} + \left(d_{p1} - d_{IB}\right)\phi_{BC}}{d_{p1}} \tag{2.8}$$

The assumption in the above implementation is that a constant gradient exists between the IB and the probe location. The above equation is applicable for the velocity and constant temperature boundary conditions.

2.5.6.2 Neumann condition

In a Neumann condition specification, the gradient of the flow variable at the IB is known instead of the actual value. The most obvious choice in such a case is to use the specified gradient value to compute the value of flow variable at the IB and then use the Dirichlet condition formulation presented earlier. However, if the value at just one probe is used to perform this operation, the accuracy of the scheme was observed to drop to first order. In order to preserve the second order accuracy, it is necessary to define a second probe which is located another probe distance Δ_p away from the first probe continuing along the surface normal direction. The arrangement of probes and applied profile is shown in Figure 2.5. As before, Taylor series expansions for ϕ_{IB}, ϕ_{p1} and ϕ_{p2} about the value at the wall ϕ_w are used – eliminating ϕ_w and a higher order gradient term to obtain the following expressions for ϕ_{IB}.

$$\phi_{IB} = \frac{\left(d_{IB}^2 - d_{p2}^2\right)\phi_{p1} + \left(d_{p1}^2 - d_{IB}^2\right)\phi_{p2} - \left(d_{IB} - d_{p1}\right)\left(d_{IB} - d_{p2}\right)\left(d_{p1} - d_{p2}\right)\left.\frac{\partial \phi}{\partial n}\right|_{BC}}{d_{p1}^2 - d_{p2}^2} \tag{2.9}$$

On the other hand, if a first-order formulation is sufficient, only information of the flow variable at the first probe ϕ_{p1} is necessary. The formulation in that case reduces to:

$$\phi_{IB} = \phi_{p1} - \left(d_{p1} - d_{IB}\right)\left.\frac{\partial \phi}{\partial n}\right|_{BC} \tag{2.10}$$

2.5.7 Conjugate heat transfer treatment

For simulations involving conjugate heat transfer (CHT), the energy equation is to be solved in the fluid region as well as the solid region. To accomplish this, the solid material properties are used to compute the value of $Re \cdot Pr$ for nodes that lie in the solid region. Along with this, a special treatment to handle the immersed boundary implementation is necessary.

The CHT boundary condition is different than the Dirichlet/Neumann conditions discussed earlier because the solid side of the immersed surface also needs to be taken care of while handling the presence of an IB. We have already discussed the definition of IB nodes on the solid side of the immersed surface for a CHT simulation which is necessary since solid nodes are also part of the governing equations. A main difficulty in IBM-CHT implementations is that IB nodes on either side do not coincide onto the same location on the surface and hence, this requires interpolations on the surface to determine the boundary condition. For instance, Kang et al. [27] use projections of the solid and fluid IB nodes onto the immersed surface and reconstruct the temperature field on the IB using second-order polynomials. This is a non-trivial operation and can be complicated, especially if we are dealing with arbitrarily shaped surface contours. In contrast, the scheme proposed here is a direct extension of the other boundary condition implementations presented earlier and does not involve any complex interpolation schemes. The treatment of solid and fluid IB nodes is done independently, coupled only by the multiple iterations which we do in order to make sure that we approach a converged solution.

For CHT simulations, two boundary conditions are to be satisfied at the IB simultaneously – (1) a Dirichlet condition at the IB which ensures the continuity of the temperature field across the interface between the two media and (2) a Neumann condition at the wall location which accounts for the balance of energy transferred across the interface. It is evident that this requires, for every IB node (fluid or solid), information from the other side (solid or fluid) of the surface. Hence, additional probes called mirror probes are defined at geometrical mirror locations about the IB. Mirror probes are defined for all IB nodes (fluid and solid) as illustrated in Figure 2.6 for a two-dimensional example. Further discussion is provided with respect to fluid IB nodes only, but exactly the same procedure applies to solid IB nodes as well.

The first condition used is the equality of heat flux across the fluid-solid interface.

$$\kappa_s \left.\frac{\partial T}{\partial n}\right|_{w,s} = \kappa_f \left.\frac{\partial T}{\partial n}\right|_{w,f} \tag{2.11}$$

where, n is the surface normal direction, pointing outwards from the solid. The gradients on the fluid and solid sides are obtained using Taylor series expansions of the IB probes and mirror probes, respectively. From the above equality, an expression for the wall temperature is obtained.

$$T_w = \frac{-d_{p2}^2\left(\kappa_s T_{mp1} + \kappa_f T_{p1}\right) + d_{p1}^2\left(\kappa_s T_{mp2} + \kappa_f T_{p2}\right)}{\left(d_{p1}^2 - d_{p2}^2\right)\left(\kappa_f + \kappa_s\right)} \tag{2.12}$$

For the corresponding formulation for solid IB nodes, we only need to swap κ_f and κ_s in the above expression. Then, the value at the IB node can be expressed in terms of the temperature values at the two probe locations and wall as:

$$T_{IB} = \frac{d_{IB}d_{p2}\left(d_{IB} - d_{p2}\right)T_{p1} + d_{IB}d_{p1}\left(d_{p1} - d_{IB}\right)T_{p2} + \left(d_{IB} - d_{p1}\right)\left(d_{IB} - d_{p2}\right)\left(d_{p1} - d_{p2}\right)T_w}{d_{p1}d_{p2}\left(d_{p1} - d_{p2}\right)} \tag{2.13}$$

2.5.8 Implementation in a fractional-step algorithm

Based on the node identification performed, the computational domain is divided into different regions for the purpose of calculations. These demarcations are depicted in Figure 2.7 for both non-CHT and CHT cases. For non-CHT case, three regions are defined – (i) the solid region Ω_s that is completely encompassed by the immersed surface Γ_{IB}, (ii) the fluid IB region Ω_{IB-f} covering the space between the IB and an imaginary stair-case interface Γ_{IB-f} formed by the shared faces between the fluid nodes and IB nodes and (iii) the fluid region Ω_f covering the remaining portion of the calculation domain. For a CHT case, an additional region Ω_{IB-s} is defined on the solid side representing the region between Γ_{IB} and the imaginary stair-case interface Γ_{IB-s} which is the solid counterpart of Γ_{IB-f}. The solid region Ω_s in this

case represents only the region encompassed by Γ_{IB-s}. These demarcations clearly distinguish the type of nodes that lie within them as well – fluid, fluid IB, solid IB and solid nodes make up the regions Ω_f, Ω_{IB-f}, Ω_{IB-s} and Ω_s, respectively. Now, we describe the implementation of the IB methodology described thus far in the framework of a fractional-step algorithm. Following are the main steps performed within the time-loop integration.

2.5.8.1 IB movement and node identification

For a moving boundary problem, tracking of the IB as well as the assignment of node types is to be performed at every time-step. This implies that the definitions of Γ_{IB}, Γ_{IB-f} and Γ_{IB-s} are reevaluated and correspondingly the different regions in the domain are redefined. Also, the boundary conditions for velocity components are updated based on the movement of the IB during the current time-step.

2.5.8.2 Intermediate velocity field

In the IBM framework, the discretized forms of the momentum equations are solved only for the cells that lie within Ω_f. The equations solved in these regions are without any modifications to the original formulations. The appropriate boundary conditions are applied to the cells contained within Ω_{IB-f} (fluid IB nodes).

$$\begin{aligned} &\text{For } \Omega_f: && \tilde{u} = \mathfrak{F}(u^n, \tilde{u}) = u^n + \Delta t\, H(u^n, \tilde{u}, p^n) \\ &\text{For } \Omega_{IB-f}: && \tilde{u} = \mathfrak{G}(\tilde{u}_p) \\ &\text{For } \Omega_s \text{ (and } \Omega_{IB-s}): && \tilde{u} = 0 \end{aligned} \tag{2.14}$$

where, $\mathfrak{F}(\cdot)$ is the time-stepping operator for the discretized momentum equations and $\mathfrak{G}(\cdot)$ is the boundary condition operator, which for velocity is usually the Dirichlet condition given in Eq. (2.8). The boundary condition value would be non-zero if the IB is moving or has surface blowing/suction.

Application of IBM related boundary condition is performed within the linear solver iteration loop. The overhead $\sim$ represents the iterative nature of the solution field and these iterations are continued until a desired level of convergence criteria is satisfied.

2.5.8.3 Temperature field

When solving for energy equation for a non-CHT simulation, the solution methodology to be followed is exactly the same as for the momentum equations with either a constant temperature or heat flux boundary condition applied as given by Eqs. (2.8) and (2.9), respectively. For CHT simulations though, we require solution to the temperature field within the solid as well. Adopting the same nomenclature as before, the following methodology is adopted:

$$\begin{aligned} &\text{For } \Omega_f \text{ and } \Omega_s: && \tilde{T} = \mathfrak{F}\left(T^n, \tilde{T}\right) \\ &\text{For } \Omega_{IB-f} \text{ and } \Omega_{IB-s}: && \tilde{T} = \mathfrak{G}\left(\tilde{T}_p, \tilde{T}_{mp}\right) \end{aligned} \tag{2.15}$$

where, $\mathfrak{G}(\cdot)$ now represents the CHT boundary condition operator given by Eq. (2.13).

2.5.8.4 Satisfying mass conservation

The velocity field obtained at this stage however does not satisfy continuity yet. Solution to the pressure equation is to be used subsequently to obtain the corrections to the pressure and velocity fields computed earlier which will render the field divergence-free. With the introduction of an immersed surface, it has been observed in the past studies that satisfying mass conservation can be a non-trivial issue and results in spurious pressure oscillations near the IB. The approach adopted here is similar to the approximated domain method proposed by Kang et al. [33].

As with the intermediate velocity field calculation before, we have different approaches for the two fluid regions of interest – Ω_{IB-f} and Ω_f. No solution is necessary in the solid regions. The first mass

conservation condition to be satisfied is to ensure that total mass flux out of the IB is the same as the mass coming out of the stair-case interface Γ_{IB-f}.

$$\sum_{\Gamma_{IB-f}} \widetilde{U} \Delta A_c = \sum_{\Gamma_{IB}} (\boldsymbol{u}_{IB} \cdot \hat{\boldsymbol{n}}) \Delta A_e \tag{2.16}$$

where, $\widetilde{U}$'s are the cell face fluxes computed based on the intermediate velocity field and, ΔA_c and ΔA_e are the discretized areas of the cells faces and surface elements, respectively. In order to accomplish this, the error in the satisfaction of the above condition is calculated and an average correction δU so computed is applied to all the cell faces that make up Γ_{IB-f}.

For all faces $\in \Gamma_{IB-f}$: $$U^{n+1} = \widetilde{U} + \delta U \tag{2.17}$$

The pressure equation can now be solved as is in the outer fluid region Ω_f. Since the fluxes at Γ_{IB-f} are already updated to satisfy conservation, we set the pressure corrections at the cells within Ω_{IB-f} to be zero. This, along with the corrected fluxes at the stair-case boundary, ensures that the outer fluid region instead sees a physically realistic flow field inside the near-IB region.

For Ω_f: $$\nabla^2 p' = \mathfrak{M}(\widetilde{U})$$

For Ω_{IB-f}: $$p' = 0 \tag{2.18}$$

For Ω_s (and Ω_{IB-s}): $$p' = 0$$

where, $\mathfrak{M}(\cdot)$ is the mass source calculated in terms of the cumulative cell face fluxes for every cell. The final pressure field can then be calculated by using the correction term p' for cells in the Ω_f region while a Neumann condition for pressure derived from the momentum equations is applied for cells within Ω_{IB-f}.

For Ω_f: $$p^{n+1} = p^n + p'$$

For Ω_{IB-f}:

$$\left.\frac{\partial p^{n+1}}{\partial n}\right|_{IB} = -n_i \left.\frac{du_i}{dt}\right|_{IB} \tag{2.19}$$

For Ω_s (and Ω_{IB-s}): $$p^{n+1} = 0$$

If the IB is stationary, then the condition for Ω_{IB-f} reduces to a zero pressure gradient condition at the IB. The cell-face fluxes and nodal velocities (in Ω_f) are then corrected using the pressure correction values. The final flux values obtained then satisfy the divergence-free condition.

For Ω_f: $$u^{n+1} = \tilde{u} + \delta u$$

For Ω_{IB-f}: $$u^{n+1} = \mathfrak{G}\left(u_p^{n+1}\right) \tag{2.20}$$

For Ω_s (and Ω_{IB-s}): $$u^{n+1} = 0$$

2.6 Results

We now present a few example calculations to showcase the capabilities of the proposed IBM framework. Specifically, calculations are performed to compute the order of accuracy of the developed method followed by a few validation simulations involving both stationary and moving immersed boundaries.

2.6.1 Computational overhead and parallel scalability

Including IBM framework in the solution methodology involves additional computational overheads and it is important to ensure that these costs are insignificant compared to the overall simulation times. It is necessary to account for overheads especially for moving IB simulations wherein there are certain IBM related operations to be performed every time-step. A previous IBM implementation in generalized coordinate systems reported approximately 5% computational cost for the node identification procedure

alone when using an IB made up of 2000 surface elements and 10M background grid cells [22]. We performed flow simulation of similar magnitude to establish a comparison of the computational requirement of our identification algorithm. In addition to node type identification, redetermination of the surface element location and the subsequent re-computing of different element and nodal properties such as surface normal directions, probe locations and the corresponding interpolation coefficients add to this repetitive expense. Since these operations are integral to a simulation involving a moving IB, we include the computational costs incurred due to these steps as part of the identification related expense.

For this purpose, a problem involving the flight aerodynamics study of a bat wing is considered [34]. While a discussion of the involved physics is out of the scope of this paper, we use this simulation to study the additional computational cost incurred due to inclusion of IBM. The domain consisted of approximately 23M fluid cells on the background while the wing is composed of roughly 18.4K surface elements. The entire identification procedure for this calculation accounted for less than 1% of the overall computational cost every time-step. This demonstrates the inexpensive nature of the implemented algorithm for a reasonably sized problem of interest.

Application of IBM framework for realistic problems also dictates the grid resolution strategy and this brings in the aspect of parallelization. Studies in the past have shown the feasibility of IBM framework to parallelization by demonstrating impressive scalability for large problems [35, 36]. The current IBM scheme has been implemented within the MPI-based domain decomposition framework of GenIDLEST. Unlike the flow solver though, the immersed boundary is usually spread across only a few of the blocks in the domain. For IBM related computations, this implies dynamic load imbalance. However, given that the time spent on these computations is relatively small, we expect the introduction of IBM to have a minimal effect on overall scalability of the code. To assess the parallel performance of the current IBM implementation, a strong scaling study is undertaken. All calculations are performed on Virginia Tech's supercomputing facility – Blueridge. This machine houses two octa-core Intel Sandy Bridge CPUs and 64

GB of memory per node with InfiniBand interconnects. The bat flight problem described earlier is used for the simulations and the performance is investigated from 32 to 1024 cores. The number of cells on the background mesh contained per core varies approximately from 718K to 22K, respectively. During the simulation, the wing undergoes complex movements through its flapping cycle traversing through multiple blocks. Figure 2.8 shows the near wing block decomposition for the simulation performed on 1024 cores. Computational times for 50 time-steps are recorded and the results are presented in Figure 2.9. It is observed that the scalability is excellent up to 1024 cores with the parallel efficiency being 75% even at 1024 cores.

2.6.2 Rotational flow between coannular cylinders

2.6.2.1 Order of accuracy

For the code verification procedure, a two-dimensional problem of rotational flow between two coannular cylinders is considered. A schematic of the used geometry is shown in Figure 2.10. The problem setup consists of a solid region Ω_s contained between the inner cylinder and the solid-fluid interface which is modeled using an immersed boundary. The space Ω_f between the IB and the outer cylinder wall consists of the fluid which is set in rotational motion due to the rotating outer wall. For the velocity field, no-slip condition is enforced at the IB while the rotational speed of outer wall is $u_\theta = 1$.

For all simulations, the outer wall is maintained at a constant temperature of $T_o = 0$ while three types of thermal boundary conditions are considered at the IB – constant temperature, constant heat flux and conjugate heat transfer. For the constant temperature case, the IB wall (and hence the solid) is maintained at a constant non-dimensional temperature of $T_{IB} = 1$, while for the constant heat flux case, the IB is set to have an outward heat flux $q''_{IB} = 1$. In the CHT simulations, the inner wall is maintained at $T_i = 1$. For each of these cases, analytical solutions can be derived for both velocity and temperature fields and are given here [27].

Velocity field:

$$u_r = 0;\ u_\theta(r) = \begin{cases} 0 & for\ R_i < r < R_{IB}\ (solid) \\ -\dfrac{R_o R_{IB}^2}{R_o^2 - R_{IB}^2} \cdot \dfrac{1}{r} + \dfrac{R_o}{R_o^2 - R_{IB}^2} \cdot r & for\ R_{IB} < r < R_o\ (fluid) \end{cases} \tag{2.21}$$

Temperature field:

Constant temperature BC at IB

$$T(r) = \begin{cases} - & for\ R_i < r < R_{IB}\ (solid) \\ T_o - \dfrac{(T_o - T_{IB})\, log(R_o/r)}{log(R_o/R_{IB})} & for\ R_{IB} < r < R_o\ (fluid) \end{cases} \tag{2.22}$$

Constant heat flux BC at IB

$$T(r) = \begin{cases} - & for\ R_i < r < R_{IB}\ (solid) \\ \dfrac{T_{IB}\, log(R_o/r) + T_o\, log\left(r/R_{IB}\right)}{log(R_o/R_{IB})} & for\ R_{IB} < r < R_o\ (fluid) \end{cases} \tag{2.23}$$

where, $T_{IB} = T_o - q''_{IB} \log(R_o/R_{IB})$.

Conjugate heat transfer BC at IB

$$T(r) = \begin{cases} T_i + \dfrac{(T_o - T_i)\, log\left(r/R_i\right)}{log(R_{IB}/R_i) + \left(\kappa_s/\kappa_f\right) log(R_o/R_{IB})} & for\ R_i < r < R_{IB}\ (solid) \\ T_o - \dfrac{(T_o - T_i)\, log(R_o/r)}{log(R_o/R_{IB}) + \left(\kappa_f/\kappa_s\right) log(R_{IB}/R_i)} & for\ R_{IB} < r < R_o\ (fluid) \end{cases} \tag{2.24}$$

For all the calculations, a body-fitting structured grid that conforms to the outer and inner walls of the geometry is created. Four systematic mesh refinements are considered with every successive level being half of its previous level. This corresponds to grid sizes Δ = 0.1, 0.05, 0.025 and 0.0125 in the radial direction. In order to examine the global discretization error behavior, L_2 norms of errors in velocity and

temperature fields are computed with respect to the derived analytical solutions for each grid level. The obtained error norms are plotted in Figure 2.11 for different cases. It is observed that second order convergence is exhibited by both the velocity field and the temperature field for all boundary conditions at the IB.

2.6.2.2 Sensitivity to probe distance

The same problem set-up is considered next to study the dependence of the results on the location of the IB node probes. A total of five probe distances are considered – $0.6\Delta_p$, $0.8\Delta_p$, Δ_p, $1.2\Delta_p$ and $1.4\Delta_p$, where Δ_p is the standard probe distance computed as described in section 2.5.6. Results from these simulations are used to compare the radial variation of the solution variables. Only a plot of the temperature profiles obtained with a CHT boundary condition is presented in Figure 2.12. It is observed that in spite of a $\pm$40% variation in the probe distance, the profiles essentially overlap each other with the maximum difference of less than 0.5%, showing that the results are not very sensitive to the exact location of the probes.

2.6.3 Uniform flow over stationary cylinder

Uniform flows over bluff bodies – specifically cylinders (2D) and spheres (3D) – are used for validation of many IBM codes. We first consider the two-dimensional case of flow over a stationary cylinder. Simulations are performed for different inflow velocities corresponding to Reynolds numbers (based on the inflow velocity and cylinder diameter) in the range 10-200. This range covers both the steady and unsteady flow regimes.

A rectangular domain of size 45D × 30D is used where D is the cylinder diameter. In the stream-wise direction, the inlet and outlet boundaries are at distances of 20D and 25D, respectively so as to avoid any influence on the near body flow structures. The boundaries in the cross-flow direction are 15D away from the cylinder and have walls sliding at inflow velocity. A uniform grid resolution of Δ = 0.0125D in the

vicinity of the cylinder is used and the resolution is relaxed away from the body according to a hyperbolic tangent distribution.

2.6.3.1 Steady flow regime ($Re_D \leq 40$)

In the steady regime, the wake is characterized by a recirculation zone consisting of two symmetric vortices attached to the immersed cylinder. The observed coefficient of drag and the size of the recirculation zone size have been well documented in literature. For comparison, results from numerical simulations of Park et al. [37] are used. The simulations of Park et al. are performed on a body-fitted staggered grid framework using a total of 128 grid points around the cylinder surface. Table 2.1 presents the comparison of coefficients of drag and recirculation zone lengths for three Reynolds numbers – 10, 20 and 40. In Figure 2.13, the local distribution of pressure coefficient for the same three Reynolds numbers are compared against the results of Dennis and Chang [38]. Excellent agreement is seen in all cases.

2.6.3.2 Unsteady flow regime ($Re_D > 40$)

For higher Reynolds numbers ($Re_D > 40$), the wake of the cylinder becomes unsteady and results in the Karman vortex street. The shedding pattern is characterized by the Strouhal number defined in this case as $St = fD \,/\, u_\infty$, where f is the frequency of vortex shedding and u_∞ is the approach velocity. The Strouhal numbers obtained for various cases are presented in Table 2.2 and as can be seen, compare very well with existing results in literature (from Silva et al. [39]).

2.6.3.3 Heat transfer results

Simulations are performed for all the Reynolds numbers presented so far with both constant temperature and constant heat flux boundary conditions at the cylinder surface. Table 2.3 presents Nusselt number data for the two boundary conditions in the steady regime in comparison to the numerical results of Bharti et al. [40]. Very good agreement is observed for both the types of boundary conditions. For the unsteady regime, average Nusselt number values are calculated. The computed values of Nusselt number are

plotted for the entire Re_D range considered in Figure 2.14 and the comparison with available results from literature (Lange et al. [41]) is excellent. For $Re_D = 120$, the local Nusselt number values are averaged over multiple vortex shedding cycles. The distribution so obtained is compared to the numerical results of [23] as shown in Figure 2.15.

2.6.4 Uniform flow over an oscillating cylinder

In continuation with the study of flow over bluff bodies, a moving boundary problem is considered next. The problem set-up is similar to that used in the stationary cylinder case, albeit with the oscillation of cylinder perpendicular to the flow direction. The cylinder is prescribed a cosine oscillation given by $y(t) = A\cos(2\pi f t)$, where A and f are the non-dimensional amplitude and frequency, respectively. For a cylinder oscillating near the natural shedding frequency, the vortex shedding pattern changes depending on the oscillation frequency. In this lock-in regime, the average energy transfer from fluid to the solid changes from positive to negative value when the amplitude of oscillation is increased beyond a certain threshold. Simulations are performed for a Reynolds number of 200 for oscillation amplitudes of A = 0.199 and 0.696 while the frequency is maintained at $f = 0.2$. At the higher amplitude, the reduced velocity exceeds the threshold frequency resulting in a change in the vortex shedding pattern as shown in Figure 2.16. The variation of lift profiles at various times is plotted in Figure 2.17 and compared to the results obtained by Leontini et al. [42], noting that the change in the shedding pattern which affects the lift profile is predicted correctly in our calculations.

2.6.5 Conjugate heat transfer through developing micro-channel flows

In order to demonstrate the validity of the developed method in a more general problem setup, we consider the case of flow through a circular micro-channel tube with thick walls. A body-fitted structured grid is generated encompassing the whole domain till the outer wall of the tube. The inner wall of the tube with which the fluid will be in contact is modeled using IBM. The background fluid grid is intentionally

created in a way that the IB is located completely in the non-orthogonal region of the domain. A schematic representation of the grid used along with the immersed surface is shown in Figure 2.18.

The problem set-up is similar to that used by Nonino et al. [43] to facilitate one-on-one comparison of the results. A uniform velocity profile is used at the inlet. At the outer wall, a constant heat flux boundary condition is used while the end walls of the tube at the entrance and exit faces are adiabatic. A CHT boundary condition is used at the immersed surface and the appropriate properties are used for calculation of the Prandtl number, Pr in the solid and fluid regions. The diameter of the outer wall is set at $D_o = 2D_i$ while the length of the tube is $L = 25D_i$. The ratio of thermal conductivities κ_s / κ_f is set at 25 while the density and specific heat of the solid are taken to be the same as that of fluid. Simulations are performed assuming that these properties are constant. The triangulated tubular surface consists of approximately 109K surface elements.

Two grid levels are considered for the background mesh. The grid size near the IB is maintained to be approximately $\Delta = 0.04D_i$ and $0.02D_i$ in the cross-flow directions. Since the domain involves developing flow near the entrance region, the grid distribution in the stream-wise direction near the inlet is set to be $\Delta = 0.04D_i$ and $0.02D_i$ (same as that in the other two directions) and is gradually increased along the flow direction. Simulations are performed for a Reynolds number of 50, defined based on the inner tube diameter and the inlet velocity. The value of Pr number for the fluid is set at 5 – hence the thermal field is expected to take much longer to attain a fully developed state compared to the velocity field. A comparison of the stream-wise distribution of local Nusselt number obtained using these two grids is presented in Figure 2.19 along with the computational results of Nonino et al. [43]. It is observed that the results at both the grid levels agree very well with results of [43]. The local Nusselt number values obtained across the inner wall surface is averaged along the cross-flow directions since the flow is axisymmetric.

Lastly, the effect of the flow velocities on the heat transfer characteristics is studied by considering two higher Reynolds numbers – 100 and 200. Same conditions are retained for all other parameters. For these calculations only the finer grid ($\Delta = 0.02D_i$) is used. The thermal development length x_L for laminar flow in a tube can be approximated as [44]:

$$\frac{x_L}{D_i} \approx 0.05\, Re \cdot Pr \tag{2.25}$$

This evaluates to lengths of 25 and 50, respectively, for $Re = 100$ and 200. The effect of entrance and exit regions on the Nusselt number distribution is hence expected to be significant. The obtained Nusselt number distributions plotted in Figure 2.20 clearly highlight this aspect. Unlike the $Re = 50$ case, the local Nusselt number distributions for both the cases are not fully developed, especially evident for the $Re = 200$ case.

2.7 Conclusions

In the current paper, a new methodology for implementing IBM on multi-block curvilinear grids is described in the framework of an existing in-house code. The main contributions of the work are: (1) an efficient methodology that can combine the advantages of both IBM and body-fitted grid techniques and (2) development of a straight-forward method of implementing conjugate heat transfer boundary condition in the described framework.

Search, locate and interpolate algorithms based on discrete phase modeling techniques are used to perform the tasks of identifying any arbitrary Lagrangian point on the background Eulerian grid and subsequently interpolating values onto this point. These are utilized in the interface tracking and node identification steps, which in the past have been observed to be the most time-consuming operations of the whole IBM scheme. Since they may have to be repeated every time-step, these tasks are critical to the efficiency of the implemented IBM scheme and are shown to consume less than 1% of the total

computational time per time-step. As a result, the scalability of the fluid solver is unaffected even for cases where the immersed surface is spread unevenly across the computational domain and/or the immersed boundary is moving. The versatility of the implementation is demonstrated in identifying the surface contours of a complex radial swirler.

To implement conjugate heat transfer boundary condition, a new method of extending the same idea as used for other boundary conditions (Dirichlet and Neumann) is described. This is done by defining additional 'mirror' probes on the other side of the IB while keeping the other details of the methodology the same. Extensive verification studies are performed using a rotational flow problem between coannular cylinders. Both velocity and temperature fields show second-order error convergence for all the boundary conditions. These are followed by a range of simulations validating the flow and heat transfer results for a variety of cases involving stationary and moving IB on both orthogonal and body-fitted grids.

Consequently, it is established that the current IBM scheme implemented in a body-fitted grid framework provides a versatile and powerful framework for simulating flow and heat transfer in complex dynamic problems.

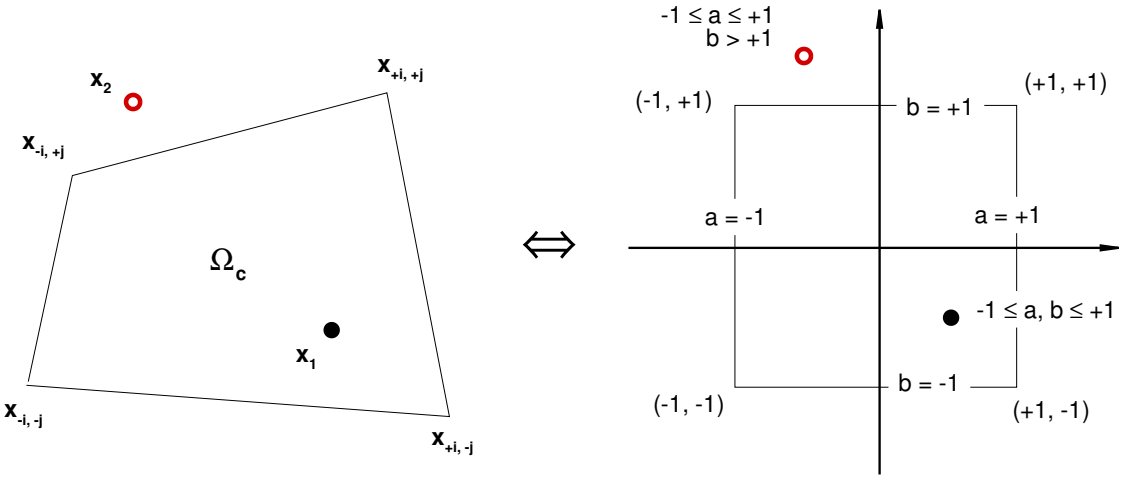

Figure 2.1 A two-dimensional example of transformation of two arbitrary points $\boldsymbol{x_1}$ and $\boldsymbol{x_2}$ from physical coordinates to computational coordinates with respect to $\boldsymbol{\Omega_c}$

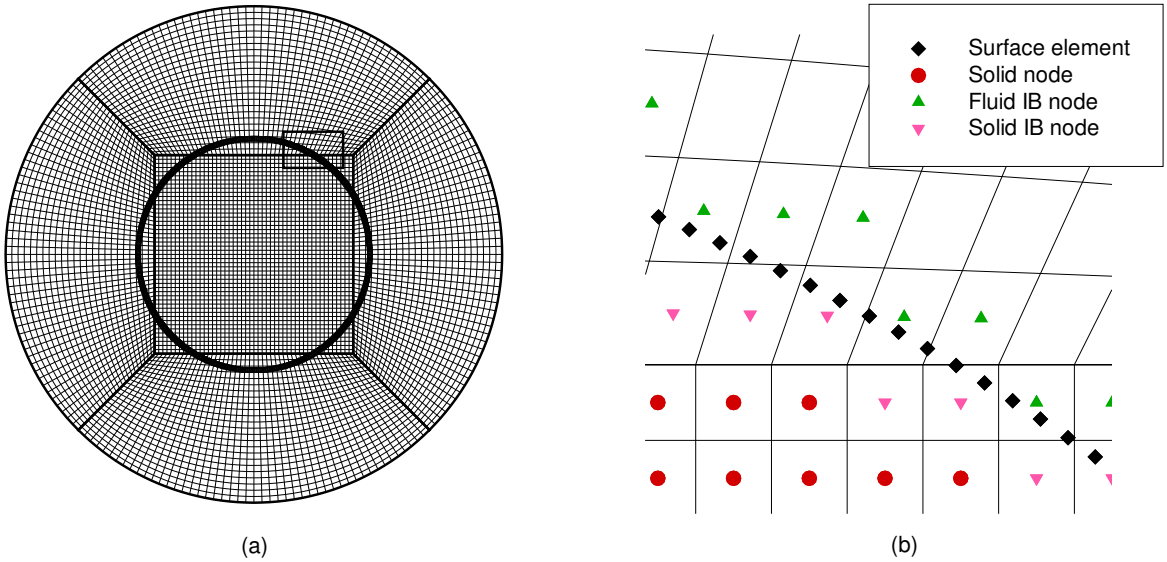

Figure 2.2 Identifying the node types in a curvilinear grid topology - (a) a body-fitted 5 block geometry for a circular domain, (b) zoomed-in view of node types identified for a conjugate heat transfer case

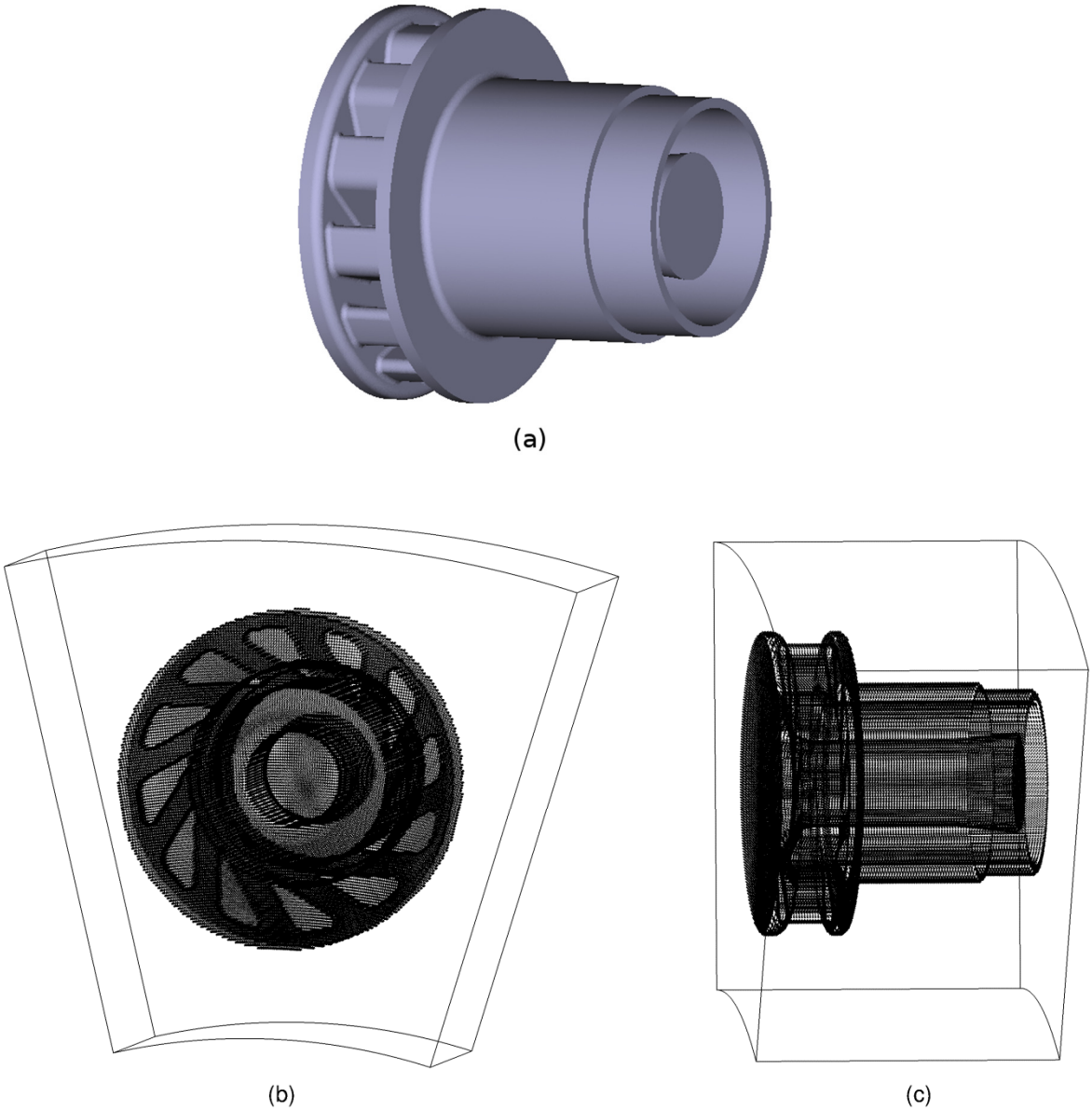

Figure 2.3 (a) A CAD representation of the radial swirler geometry; (b), (c) the fluid IB nodes assigned on an annular non-orthogonal grid

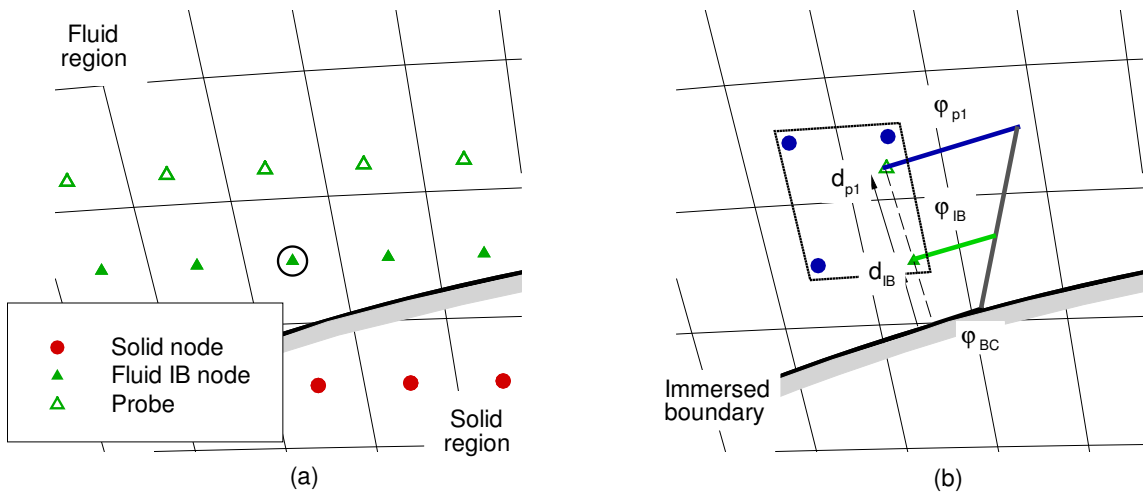

Figure 2.4 Dirichlet condition implementation involving the use of a single probe in the normal direction. The distances d_{IB} and d_{p1} are both measured from the immersed boundary

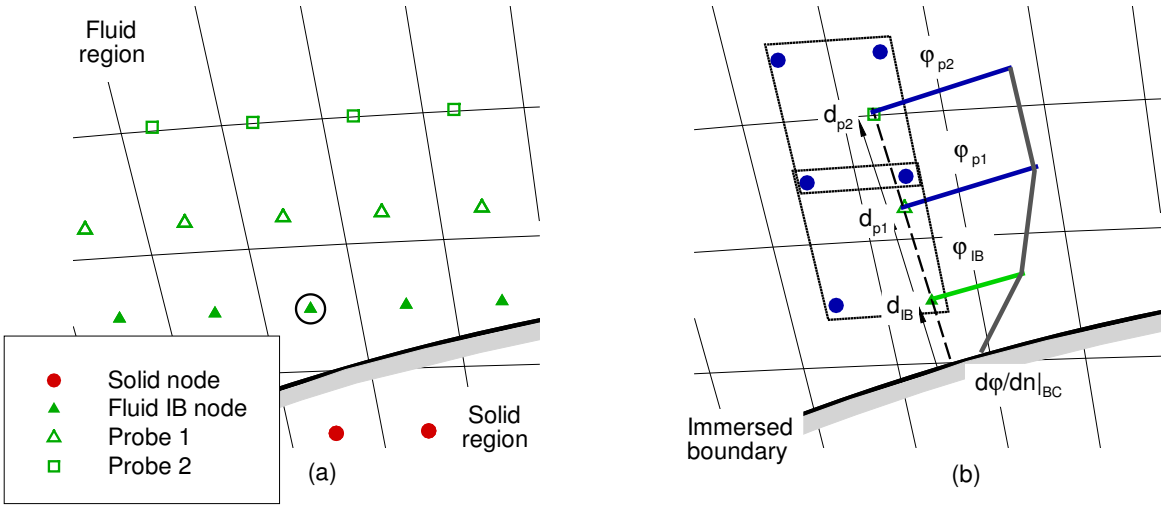

Figure 2.5 Neumann condition implementation with use of two probes both placed along the normal direction. All the distances d_{IB}, d_{p1} and d_{p2} are measured from the immersed boundary

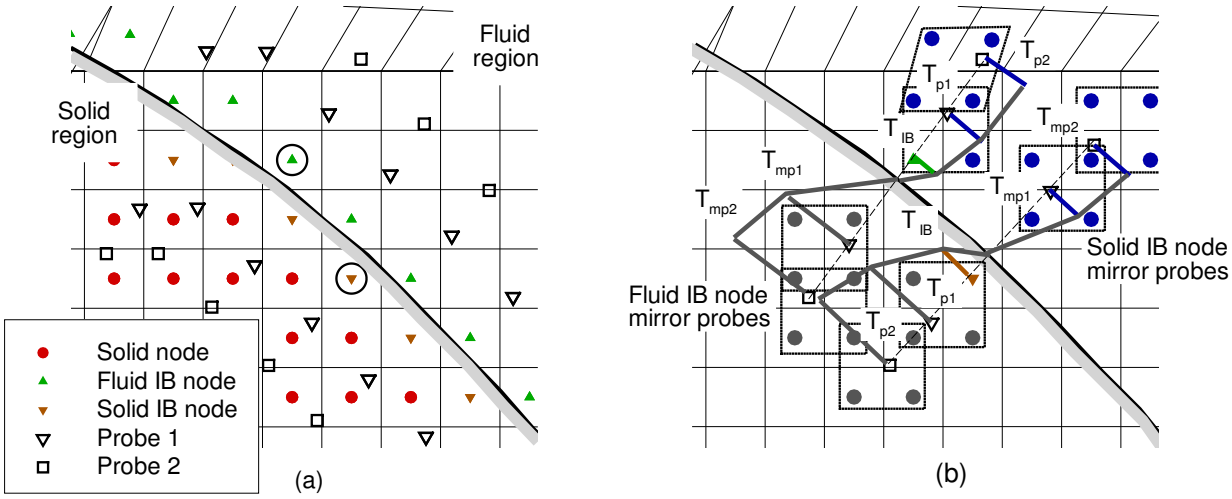

Figure 2.6 Conjugate heat transfer treatment with use of probes and mirror probes. Distances are again measured from the immersed boundary and the mirror probes mp1 and mp2 are located at the same distance as p1 and p2 (that is at d_{p1} and d_{p2}, respectively). The gray and the blue circles in (b) represent the interpolation nodes used in the solid and fluid regions, respectively

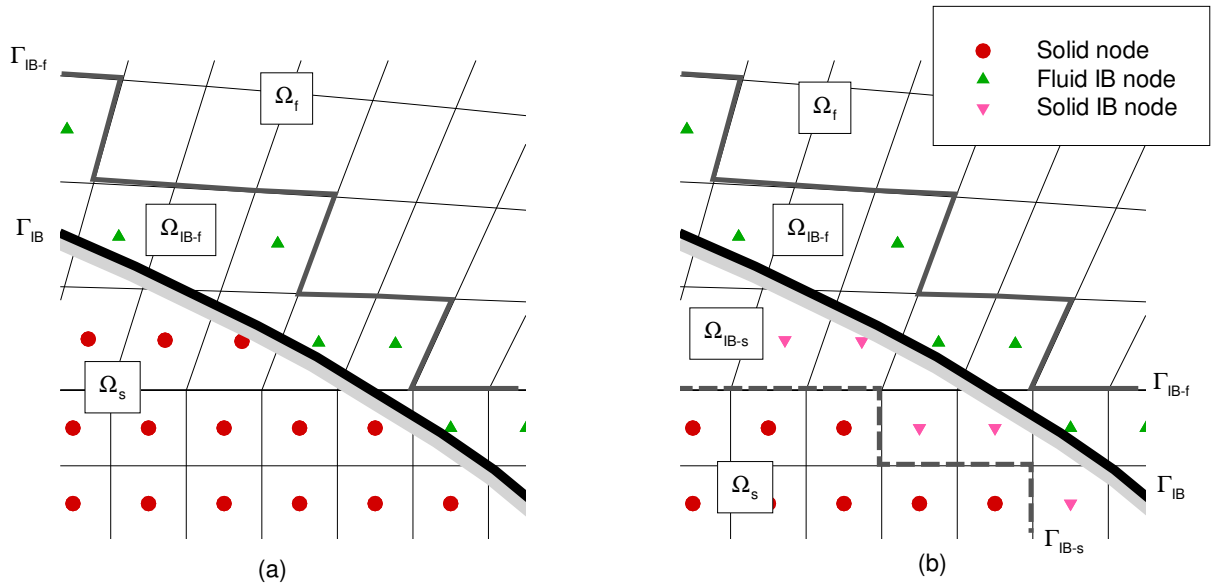

Figure 2.7 Definition of domain types for (a) non-CHT and (b) CHT cases

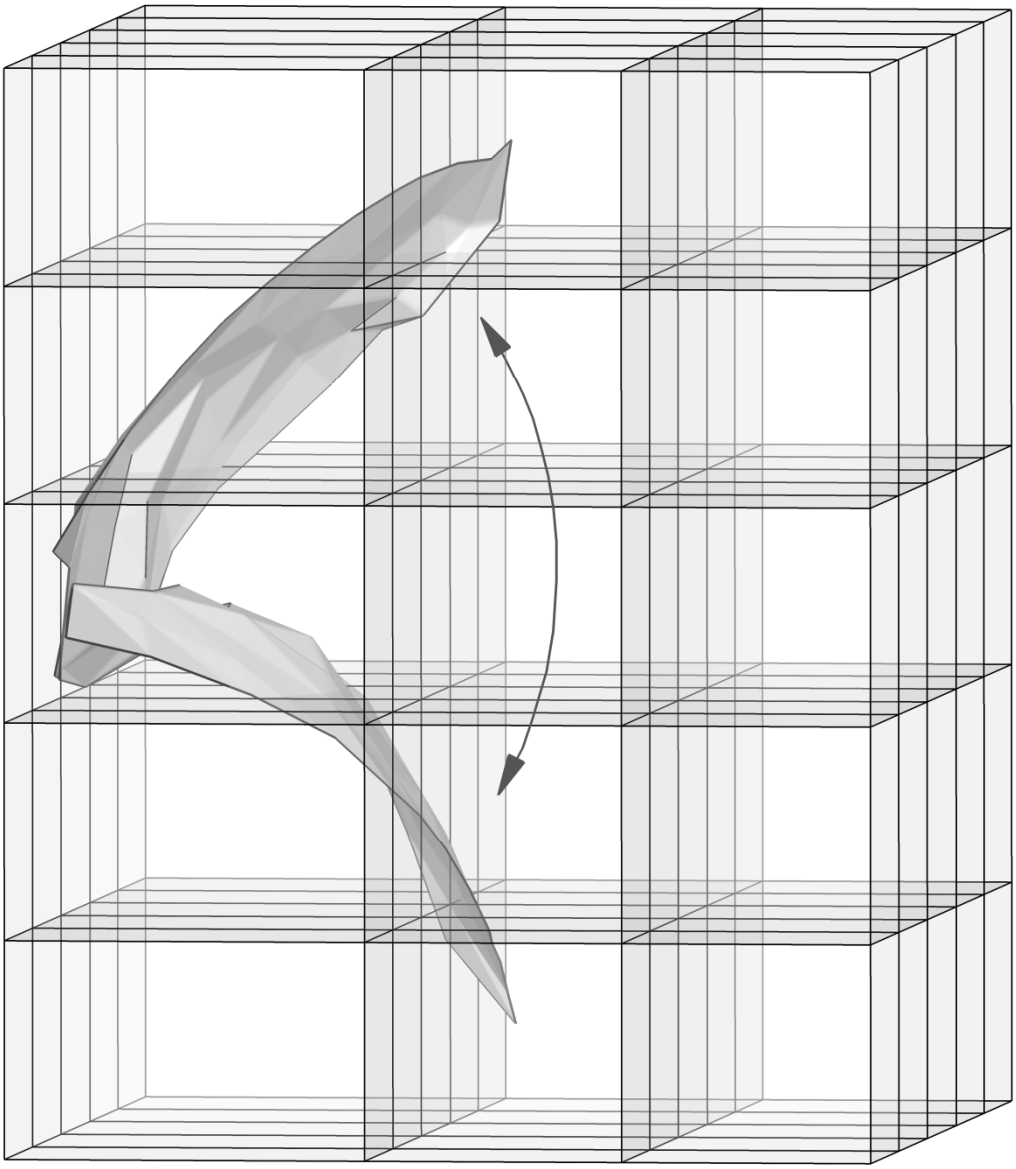

Figure 2.8 Close-up view of the near wing domain decomposition showing the spread of the IB over multiple blocks on the background grid

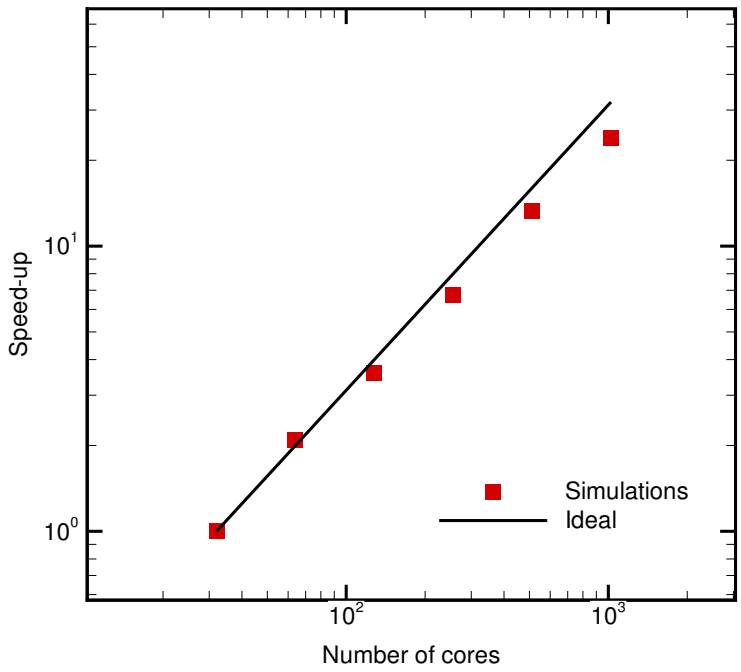

Figure 2.9 Strong scaling performance of the implementation for a flow simulation involving bat flight aerodynamics

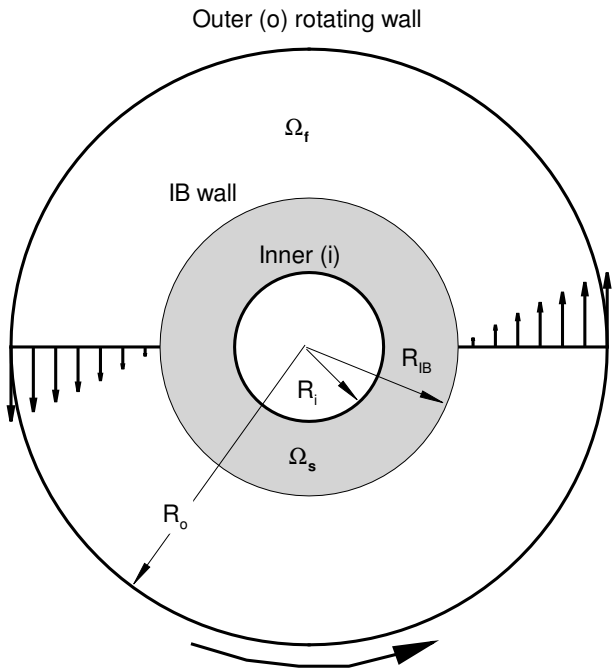

Figure 2.10 Coannular cylinder geometry used for code verification

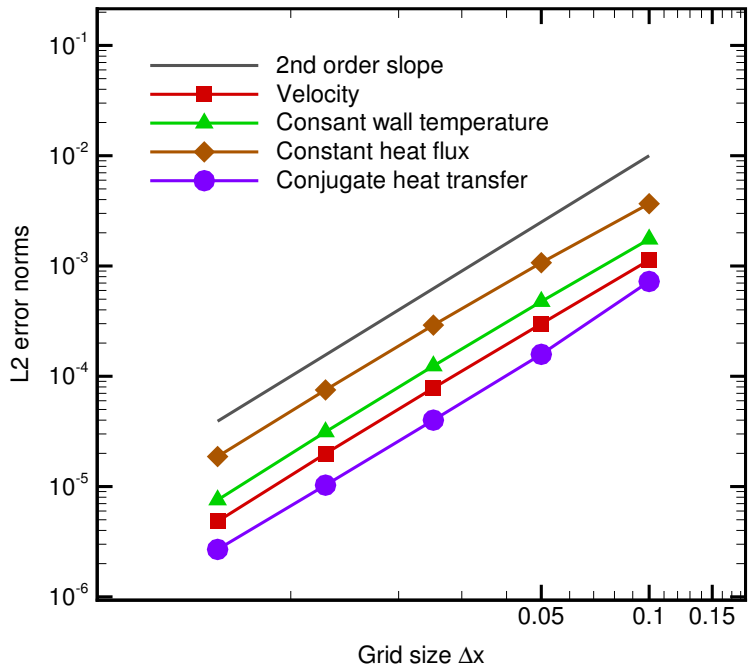

Figure 2.11 L_2 error norms computed at various grid levels for application of velocity, constant temperature, constant heat flux and conjugate heat transfer boundary conditions at the immersed boundary

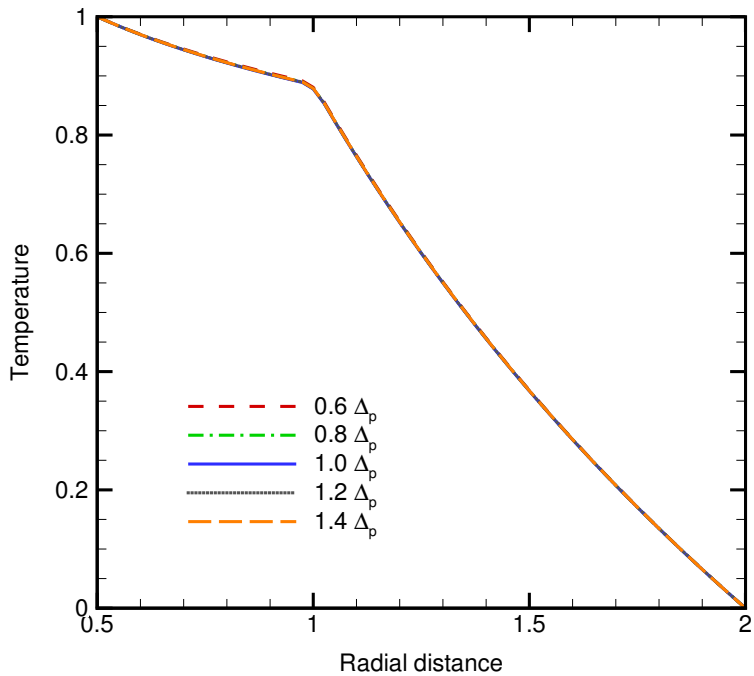

Figure 2.12 Temperature profiles obtained for rotational flow simulations with CHT boundary condition between coannular cylinders using different probe distances ranging from 0.6-1.4 Δ_p

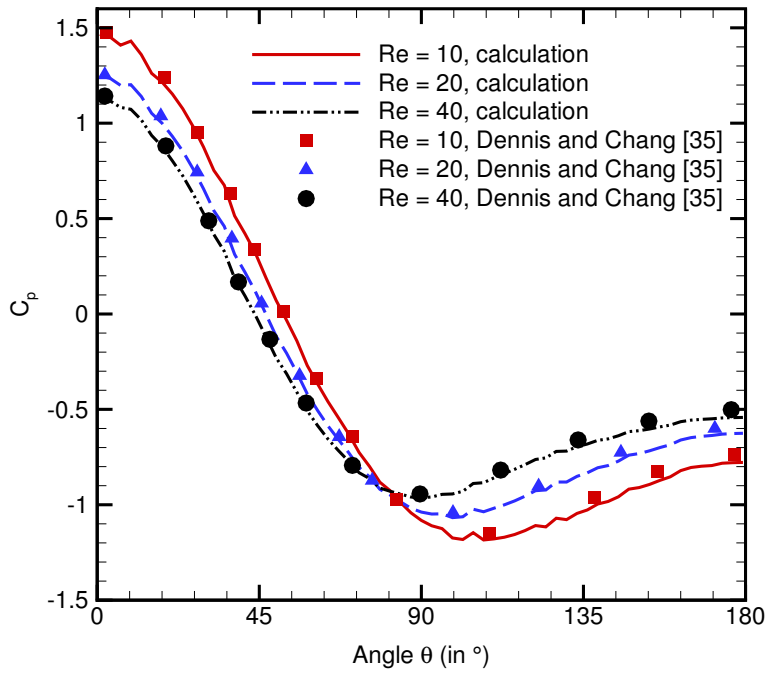

Figure 2.13 Pressure coefficient distribution around the cylinder surface in the steady regime ($Re_D \leq 40$).

$\theta = 0$ represents the stagnation point.

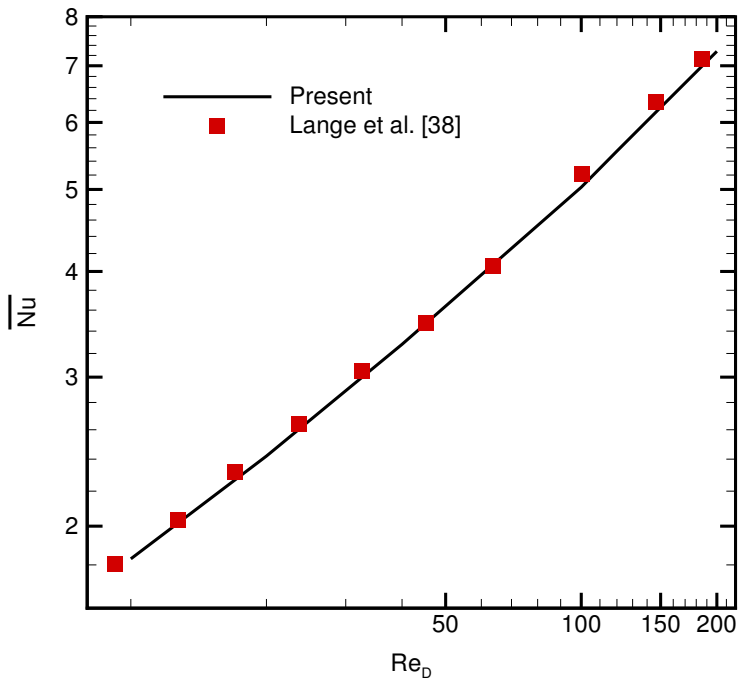

Figure 2.14 Nusselt number variation for constant wall temperature case at different Reynolds numbers. For unsteady regime, the averaged Nusselt number value is plotted.

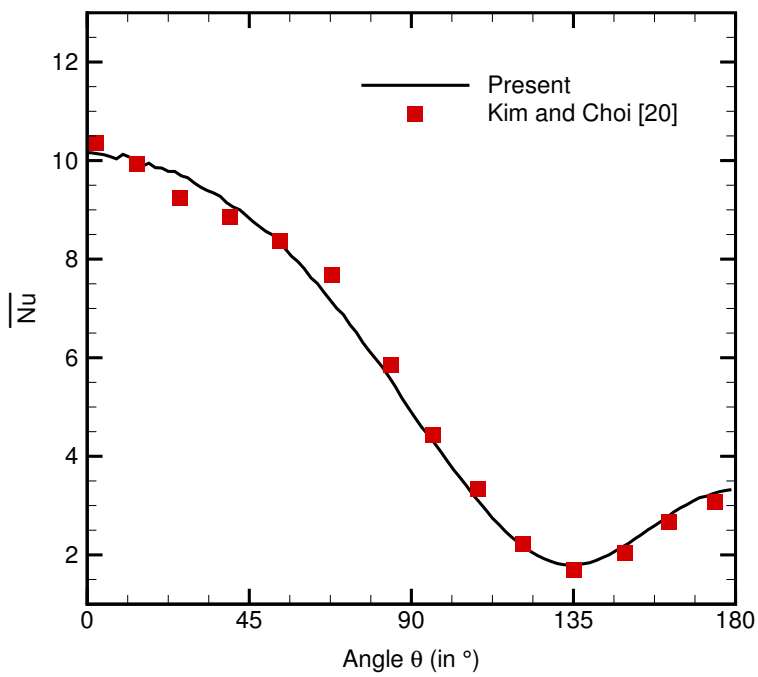

Figure 2.15 Local distribution of time-averaged Nusselt number computed around the cylinder surface for $Re_D = 120$. $\theta = 0$ represents the stagnation point.

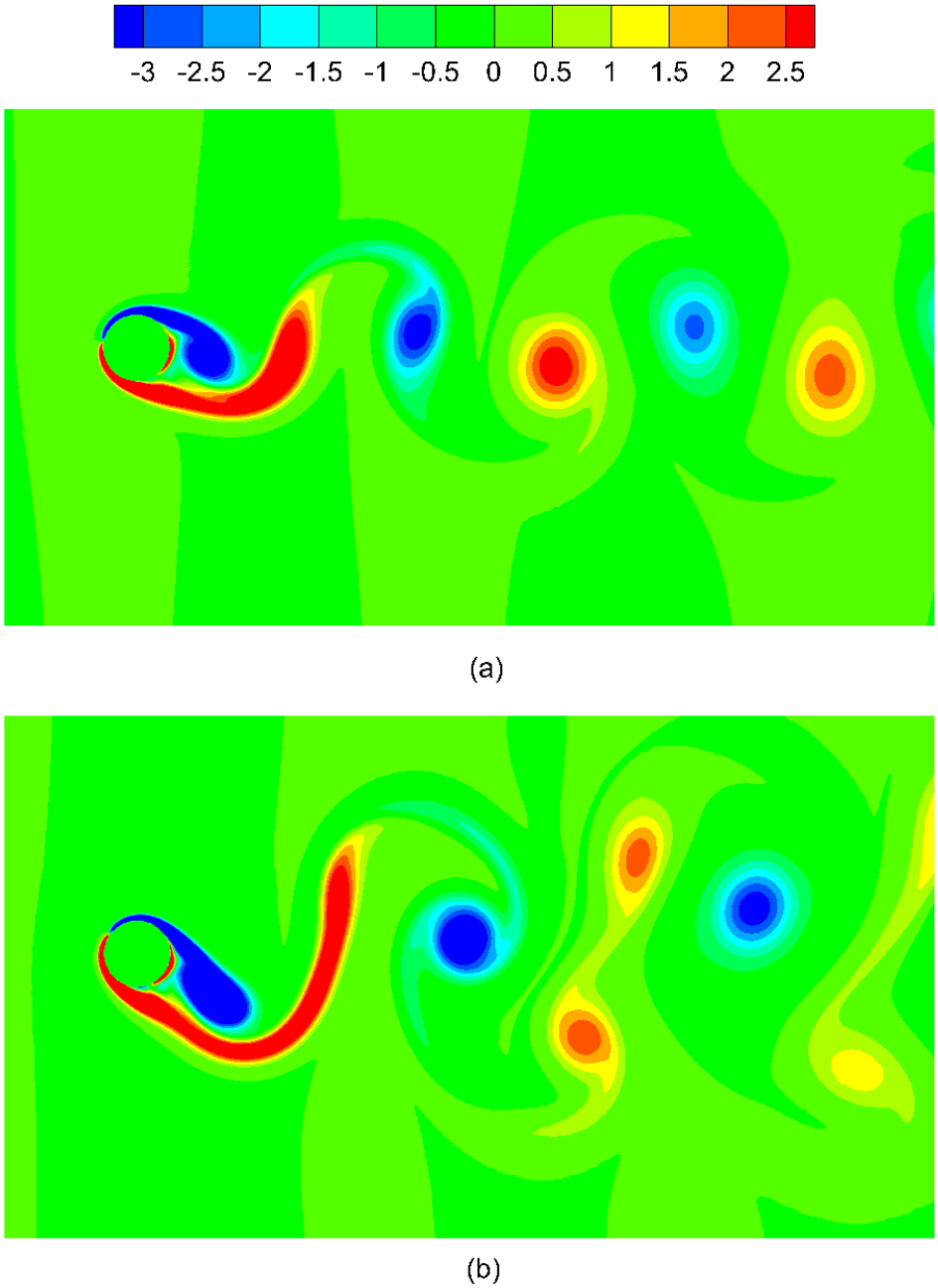

Figure 2.16 Contour plots of vorticity for (a) low amplitude $A = 0.199$ and (b) high amplitude $A = 0.696$. The higher oscillation amplitude case shows a change in the vortex shedding pattern resulting from the change in sign in the overall energy transfer

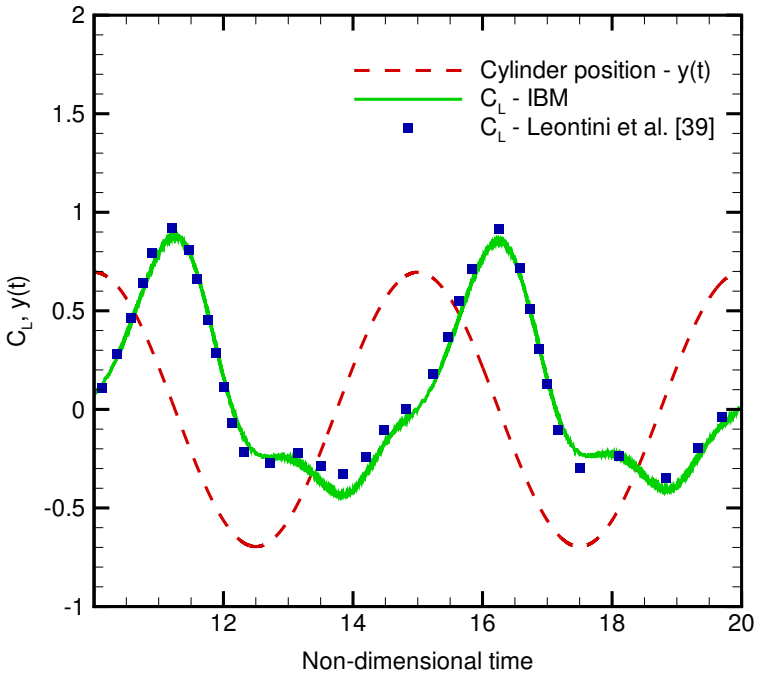

Figure 2.17 Comparison of the variation of lift profiles obtained with time for the higher amplitude case at $Re_D = 200$

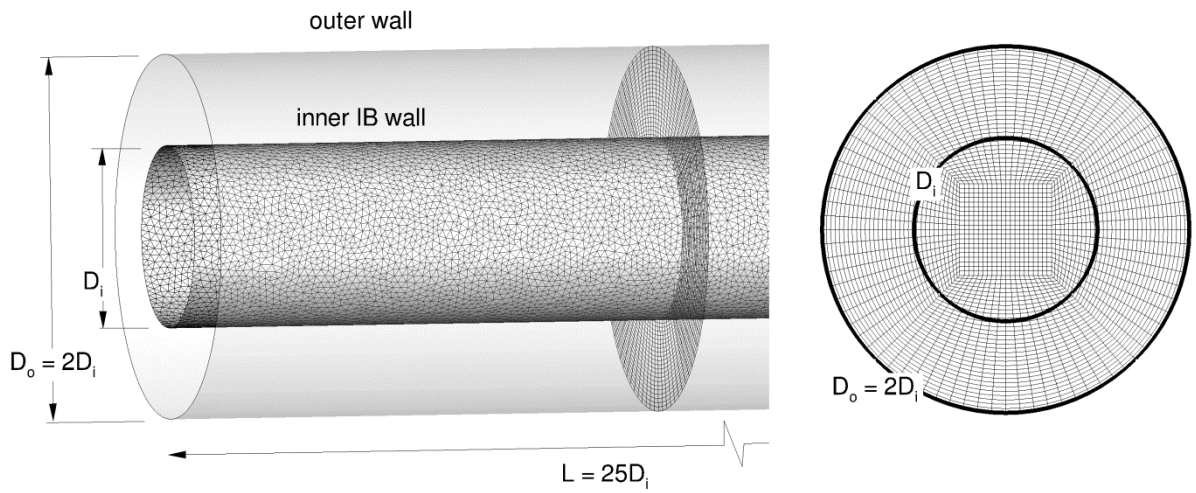

Figure 2.18 A schematic of the problem geometry used along with the dimensions and the cross-flow directional grid distribution

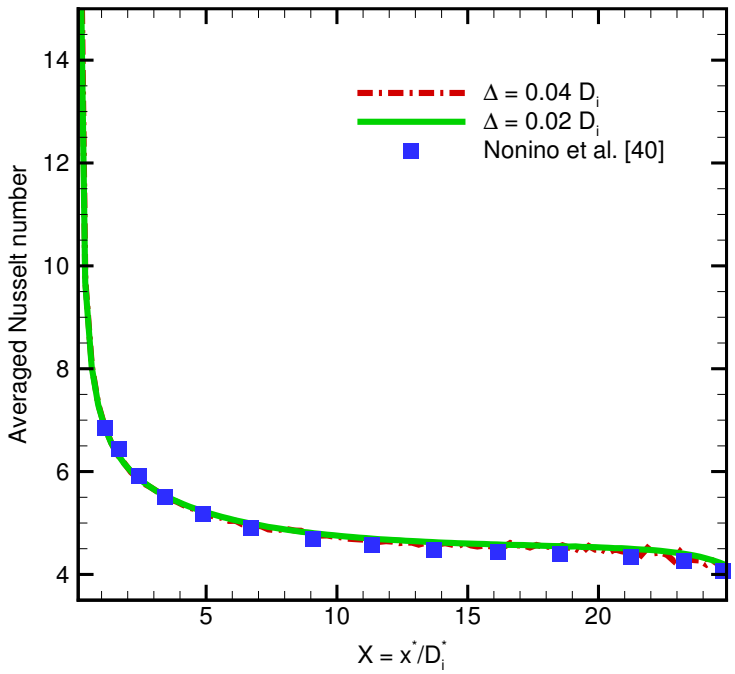

Figure 2.19 Comparison of local Nusselt number distributions computed on two grid levels - $\Delta = 0.04D_i$ and $0.02D_i$ with the results of Nonino et al. [43] for a flow through thick-walled micro-channel ($Re = 50$)

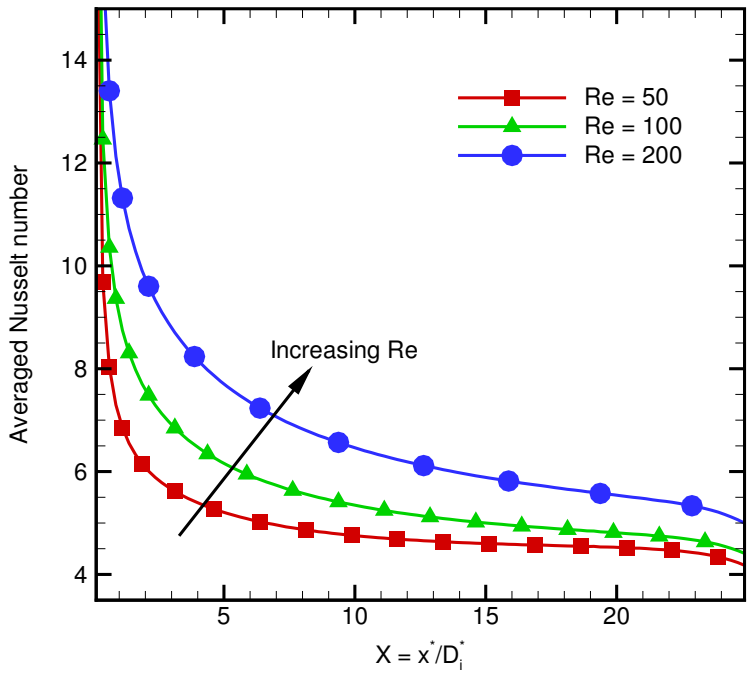

Figure 2.20 Effect of increasing Reynolds numbers on the local Nusselt number distribution. All calculations are performed at the finer grid level ($\Delta = 0.02D_i$)

Table 2.1 Comparison of drag coefficients C_D and lengths of recirculation zones L_w at different Reynolds numbers for uniform flow over a stationary cylinder

Reynolds number	$\boldsymbol{C_D}$		$\boldsymbol{L_w}$	
	[37]	**Present**	**[37]**	**Present**
10	2.78	2.80	0.25	0.25
20	2.01	2.00	0.95	0.93
40	1.51	1.54	2.30	2.26

Table 2.2 Comparison of Strouhal numbers computed at different Reynolds numbers for flow over a stationary cylinder in the unsteady regime

Reynolds number	**Strouhal number**	
	Silva et al. [39]	**Present**
100	0.16	0.166
150	0.18	0.185
200	0.20	0.198

Table 2.3 Computed Nusselt number values for constant temperature and heat flux boundary conditions at the cylinder surface

Reynolds number	$\boldsymbol{Nu_D}$ **(CWT)**		$\boldsymbol{Nu_D}$ **(CHF)**	
	[40]	**Present**	**[40]**	**Present**
10	1.86	1.83	2.04	2.00
20	2.46	2.42	2.78	2.71
40	3.28	3.20	3.77	3.67

Chapter 3
Flows Through Reconstructed Porous Media Using Immersed Boundary Methods[2]

3.1 Abstract

Understanding flow through real porous media is of considerable importance given their importance in a wide range of applications. Direct numerical simulations of such flows are very useful in their fundamental understanding. Past works have focused mainly on ordered and disordered arrays of regular shaped structures such as cylinders or spheres to emulate porous media. More recently, extension of these studies to more realistic pore spaces are available in the literature highlighting the enormous potential of such studies in helping the fundamental understanding of pore-level flow physics. In an effort to advance the simulation of realistic porous media flows further, an immersed boundary method (IBM) framework capable of simulating flows through arbitrary surface contours is used in conjunction with a stochastic reconstruction procedure based on simulated annealing. The developed framework is tested in a two-dimensional channel with two types of porous sections – one created using a random assembly of square blocks and another using the stochastic reconstruction procedure. Numerous simulations are performed to demonstrate the capability of the developed framework. The computed pressure drops across the porous section are compared with predictions from the Darcy-Forchheimer equation for media composed of different structure sizes. Finally, the developed methodology is applied to CO_2 diffusion in porous spherical particles of varying porosities.

3.2 Introduction

Studies related to fluid flow and heat transfer through porous media attract significant interest from researchers due to their application in a variety of problems such as those related to the geothermal,

[2] Reprinted from Journal of Fluids Engineering, vol. 136(4), Nagendra, K. and Tafti, D.K., "Flows Through Reconstructed Porous Media Using Immersed Boundary Methods", pp 040908, with permission from ASME.

mechanical and material sciences. Flows through porous media, as seen in most of the literature, are generally modeled using modified governing equations with correction terms to account for the porosity. Resolving flows through porous media with direct simulations using conventional CFD techniques is often quite challenging given the task of generating grids around intricate microstructures through which the flow is to be simulated.

Early works on porous media flows mainly involved modifications being applied to the basic governing equations based on volume-averaged simplifying assumptions. These modified equations are shown to be applicable to a wide variety of problems including saturated and unsaturated flows [45]. On the other hand, the initial numerical works generally studied flows through ordered arrays of regular structures [46]. A main reason for the choice of such simulations was the use of periodic boundary conditions that allowed such simulations in a much smaller geometry thus saving large amounts of computational time. In the last couple of decades, flows through porous media constituting randomly arranged simple-shaped obstacles are seen in the literature [47-49] and have proven to be immensely useful in the fundamental understanding of porous flows. With the improvement in computational capabilities, more studies related to disordered porous media have become feasible. The thrust is slowly shifting towards simulations that can resolve the pore structures by means of direct numerical simulations [50-53].

Different methods have been employed for simulation of pore-resolving porous media flows in the past. These include use of lattice-Boltzmann [54, 55], smoothed particle hydrodynamics (SPH), moving particle semi-implicit (MPS) [51, 56] methods among others. A viable alternative to the above mentioned solution methodologies is to perform pore-resolved simulations solving complete Navier-Stokes equations in conjunction with immersed boundary methods (IBM). IBM has already been used by Smolarkiewicz and Winter [50] and Malico and de Sousa [57] for porous media flows. In order to account for realistic pore spaces, it is common practice to use high resolution imaging techniques to reproduce the porous geometries, both by directly using the available measurements and by using statistical procedures

to produce faithful reconstructions of the original samples. For instance, Zaretskiy et al. [58] used X-ray CT reconstructed geometry in conjunction with a finite element solver while Ovaysi and Piri [51, 56] employed a particle based solution methodology for porous media flows for solute transport. While use of direct experimental imaging for pore space geometry creation is ideal, in many cases it is hard to perform these measurements. In such cases, use of stochastic reconstruction procedures provides a very viable way of obtaining good replicas of the real pore space. Indeed, the quality of the resulting geometries is directly limited by the accuracy and resolution of the available experimental measurements (which are used to produce the necessary statistical descriptors). It is the primary goal of this work to establish a straight-forward methodology for simulating fluid flows through complex microstructures that exist in real porous media, by way of using a combination of stochastic reconstruction procedure with direct numerical simulations using IBM framework. From a CFD point of view, the problem at hand is two-fold: (1) capability to recreate three-dimensional porous structures which closely match real porous media and (2) being able to perform numerical simulations of flows through such complex structures. The objective of this work is to develop a suitable framework which can perform high-fidelity direct numerical simulations of flows through real porous media and study the related effects in different flow regimes. The paper details the work undertaken in this regard.

The simulation of random heterogeneous media from limited statistical data is an intriguing problem that has attracted a lot of interest recently. Such procedures are useful in reconstruction of three-dimensional structures using the information obtained from experimentally obtained two-dimensional slices. Among the many approaches that have been used in the past, one technique that stands out from the rest due to the ease of implementation and the generality of the procedure is the use of stochastic reconstruction using statistical methods [59-61]. Following these, Politis et al. [62] developed a hybrid method that uses a process-based initialization procedure with a simulated annealing algorithm to produce microstructures. It is shown that this method is able to produce structures that show a better match to the original than with

just the simulated annealing algorithm while at the same time being significantly computationally less intensive. Also, implementing additional statistical descriptors is straight-forward, though computationally expensive, making it a very attractive procedure.

While generation of microstructures that mimic realistic porous media in itself is a challenging task, simulation of flow through these geometries using traditional CFD techniques is also a non-trivial problem. The time spent on generation of body-fitting meshes for structured grids requires a huge amount of user input, especially with increasing geometric complexity, and in many cases may be a fruitless task. Unstructured solvers are better in terms of ease of grid generation but are much harder to implement and require large amounts of book-keeping and memory. These difficulties have led to the development of non-boundary conforming techniques for CFD problems which have gained considerable popularity, owing mainly to the versatile capabilities that such implementations offer in comparison to traditional CFD codes. In contrast to the body-fitting techniques, the use of non-boundary conforming formulations allows simulations of fluid flow around bodies with complex features on a relatively simple fixed background mesh. A class of such techniques known as the "Immersed Boundary Methods" (IBM) was first proposed and popularized by Peskin and coworkers [4, 6] who used this method for blood flow simulation through heart valves on a fixed background Cartesian grid. Numerous implementations have been presented since with applications ranging from diffusion dominated flows to direct numerical simulations of turbulent flows through complex moving geometries. A wealth of literature is available on the range of capabilities that can be developed using IBM. For a detailed review of the different flavors of IBM, the reader is directed to the detailed review by Mittal and Iaccarino [63]. Only a brief review of the most relevant works is presented here.

The basis of any immersed boundary (IB) scheme is to solve the governing equations with the addition of a force field in and around the solid surface. Typically, the grid is non-conformal to the solid boundaries and an additional forcing is applied to the flow near these boundaries to enforce the appropriate boundary

conditions. The different IBM techniques differ in the exact way in which the forcing is applied in the vicinity of the immersed boundary. The implementation used in the current work is based on a forcing approach first proposed by Mohd-Yusof and coworkers [9, 10] and later extended to a more general 3D framework by Gilmanov and Sotiropoulos [14]. This scheme involves usage of an unstructured triangular mesh for surface discretization allowing the description of arbitrarily shaped 3D contours. It is applicable to sharp solid interfaces and does not suffer from blurring of the interface which may occur in a continuous forcing approach originally proposed by Peskin and coworkers.

The outline for the rest of the paper is as follows: (1) discussion of a suitable immersed boundary framework for simulation of flows through complex geometries, (2) a brief description of the adapted scheme for generation of realistic porous media geometries, (3) details of validation studies on the developed numerical framework and (4) simulation of simple test flows through porous geometries.

3.3 Nomenclature

3.3.1 English symbols

A Forchheimer term

d distance

d_p average size of porous structure

D cylinder diameter; diffusion coefficient

f friction factor

H channel height

n normal direction

P pressure

Re Reynolds number

Re_p particle Reynolds number

t time

u velocity

x coordinate direction

y^c component mass-fraction

3.3.2 Greek symbols

ϵ porosity

κ permeability

ρ density

ϕ flow variable

μ absolute viscosity

3.3.3 Subscripts

BC boundary-condition (value at the wall)

in inlet

p probe

ref reference value

3.3.4 Superscripts

$*$ dimensional quantity

3.4 Methodology

All the calculations presented in this work are performed using an in-house code Generalized Incompressible Direct and Large Eddy Simulation of Turbulence (GenIDLEST) [28]. As part of the current work, a framework is developed to simulate flows through real porous media using a combination of immersed boundary techniques and stochastic reconstruction. A brief description of the numerical methodology used is presented here.

3.4.1 Fluid flow solver

GenIDLEST is an incompressible fluid flow solver capable of simulating flows with temperature dependent property variations on a generalized coordinate framework. It uses a hybrid structured mesh with unstructured multi-block topology for simulations in complex non-orthogonal geometries. The program uses state-of-the-art linear solvers, specifically designed for modern hierarchical memory sub-systems, based on Krylov methods (CG, BICGSTAB and GMRES) with multi-level additive/multiplicative Schwarz preconditioners.

The governing Navier-Stokes equations for incompressible fluids with temperature dependent property variation based on Sutherland's law are written as follows in non-dimensional form using index notation [29]:

Mass conservation

$$\frac{\partial \rho}{\partial t} + \frac{\partial}{\partial x_i}(\rho u_i) = 0 \tag{3.1}$$

Momentum conservation

$$\frac{\partial}{\partial t}(\rho u_i) + \frac{\partial}{\partial x_j}(\rho u_i u_j) = -\frac{\partial P}{\partial x_i} + \frac{1}{Re}\frac{\partial}{\partial x_j}\left[\mu\left(\frac{\partial u_i}{\partial x_j} + \frac{\partial u_j}{\partial x_i}\right) - \frac{2}{3}\mu\left(\frac{\partial u_k}{\partial x_k}\right)\delta_{ij}\right] \tag{3.2}$$

where the non-dimensionalizations are given by $\rho = \rho^* / \rho^*_{ref}$, $t = t^* U^*_{ref} \,/\, L^*_{ref}$, $x = x^* \,/\, L^*_{ref}$, $u = u^* \,/\, U^*_{ref}$, $Re = \rho^*_{ref} U^*_{ref} L^*_{ref} \,/\, \mu^*_{ref}$, $P = \left(P^* - P^*_{ref}\right) / \rho^* {U^*_{ref}}^2$ and $\mu = \mu^* \,/\, \mu^*_{ref}$.

The above mentioned governing equations are transformed to generalized coordinates and solved using a conservative finite-volume formulation on a non-staggered grid topology. The Cartesian velocities and pressure values are calculated and stored at the cell center, whereas contravariant volume fluxes are calculated and stored at the cell faces. For time integration, a projection method using second order predictor-corrector steps is used. The projector step calculates an intermediate velocity field and the corrector step calculates the updated divergence free velocity at the new time-step.

For a multi-component system involving species diffusion, the same governing equations are applicable albeit with the use of average properties for the mixture. In addition, the following species continuity equation needs to be solved to ensure mass conservation of the individual components.

$$\frac{\partial(\rho y^c)}{\partial t} + \frac{\partial}{\partial x_i}(\rho y^c u_i) = \frac{\partial}{\partial x_i}\left(\rho D \frac{\partial(y^c)}{\partial x_i}\right) \tag{3.3}$$

where, y^c is the component mass fraction and D is the binary diffusion coefficient.

3.4.2 Immersed boundary method

For immersed boundary modeling, a sharp interface approach capable of handling complex 3D surface contours is implemented. This is based on a scheme first proposed by Gilmanov and Sotiropoulos [14] and has been modified suitably to conform with the non-staggered generalized coordinate framework of GenIDLEST. The major steps in the current IBM implementation are summarized below.

3.4.2.1 Definition of surface grid

The solid boundary to be modeled as IB surface is provided as input in a discretized form. Each of the discrete surface element (hereafter referred to as element) is associated with information regarding its

location with respect to the fixed background fluid grid, surface normal and area. The areas of the elements are maintained at roughly the same size as the cells on the background mesh.

3.4.2.2 Identification of nodes

Each of the nodes existing in the calculation domain is categorized as a – fluid, solid or an IB node. The determination is based on location of the cell center of each node with respect to the IB surface. If a cell center lies within an IB surface, it is termed as solid node while if it lies outside of it, it is termed as fluid. A new type of node is then defined called the IB node, which is any fluid node that lies directly adjoining the IB surface and thus, will have at least one of the six neighboring cells to be a solid cell.

The essence of our method is that no calculations are performed on the solid and IB nodes, thus necessitating the above mentioned determination of node types. The iterative solvers provide solution to the flow variables only at the fluid nodes while a special treatment is employed for boundary condition setting at the IB nodes which is discussed next.

3.4.2.3 Boundary treatment for IB nodes

Since the governing equations are solved at the fluid nodes without any modification, the values of flow variables at the IB nodes essentially act as the boundary conditions. The IB nodes hence are provided with values so as to reflect the presence of a solid surface next to them. For this purpose, every IB node is associated with a probe which will be used in the setting of boundary condition as shown in Figure 3.1. The location of the probe is taken to be at one cell distance from the IB node in a direction along the surface normal. A tri-linear interpolation scheme is used to determine the value of the desired primitive flow variable from the surrounding nodes. The value so obtained at the probe is then utilized in the computation of the value at IB node satisfying the appropriate boundary condition.

It is to be noted that among the surrounding nodes for every IB node probe, at least 1 of the surrounding nodes is an IB node. Thus, multiple inner iterations are performed for computation of IB node values to

overcome any implicit dependence on other IB node values. The convergence criteria used for the inner iterations are the same as those for outer iterations (linear solvers) and it is observed that convergence occurs within the first two inner iterations for all the simulations.

For Dirichlet boundary condition (used for velocity components), a constant gradient in the region between the IB surface and the probe location is assumed. This leads to the following formulation for Dirichlet condition:

$$\phi = \frac{d_1 \cdot \phi_p + d_2 \cdot \phi_{BC}}{d_1 + d_2} \tag{3.4}$$

On the other hand for Neumann boundary condition (used for pressure), an application of a one-sided difference equation leads to:

$$\phi = \phi_p - d_2 \cdot \left.\frac{\partial \phi}{\partial n}\right|_{BC} \tag{3.5}$$

The normal pressure gradient at the IB surface is taken to be zero. In order to ensure a divergence free velocity field, averaged flux corrections (computed based on error in global mass conservation) are applied at all the cell faces that lie between an IB node and a fluid node. This enforces the mass conservation in the approximated fluid domain that lies outside of these cell faces at which the corrections are applied [33].

3.4.3 Stochastic reconstruction of porous media

In the current work, a reconstruction procedure based on the hybrid method developed by Politis and coworkers [62] is adapted. The method is capable of recreating two- and three-dimensional structures with prescribed statistical characteristics of the porous medium. A great many studies are available in literature that describe in detail the development of such methodologies [64]. Generation of “realistic”

structures which match the original structure depends strongly on the type of statistical correlations used for reconstruction. While the porosity and two-point correlation function are the necessary descriptors, they are by themselves insufficient in providing the pore connectivity information, thus resulting in porous morphologies with poor pore space connectivity. The lineal path and two-point cluster functions are additional descriptors commonly used in the literature to improve the connectivity of the generated structures [65]. Though computationally expensive, use of these additional correlations in the simulated annealing procedure is straight-forward. In this study, our primary objective is to demonstrate the capability developed using porous media that are stochastically reconstructed. Hence, in order to keep the computational requirements of reconstruction step to a bare minimum, we have used only the porosity and two-point correlation function for reconstruction. A brief listing of the step-by-step methodology used is provided here:

1. Provide the medium porosity and n-point autocorrelation function as the inputs. For generation of correlation functions, a randomly packed array of circular structures whose diameter d_p is the same as the expected average size of each porous structure is used.
2. Initialize the reconstruction process by generating a random field of desired porosity across the domain consisting of 0's and 1's (0 is porous region and 1 is solid).
3. Compute the energy of the system E, defined as the sum of the squared differences between input correlations and those of the generated structure. Store E as the energy of the old state E_o.
4. A new structure is obtained by interchanging two randomly selected pixels of opposite phases. Selection of pixels of different phases ensures that the porosity of the structure is maintained at the original value.
5. Compute energy of the new configuration E_t.
6. The new configuration is accepted based on a probability given by the Metropolis rule:

$$P(\Delta E = E_t - E_o) = \begin{cases} exp\left(-\frac{\Delta E}{k_B T}\right) & if\ \Delta E > 0 \\ 1 & if\ \Delta E \leq 0 \end{cases} \tag{3.6}$$

7. Steps 4-6 are applied at the same temperature T (used in the Metropolis rule) N times.

8. Decrease the temperature by a very slow rate and repeat steps 4-7.

9. Exit when the number of successful swaps becomes less than a specified value.

The output of this procedure is to produce node-based binary information about the domain representing all the solid nodes as 0 and fluid nodes as 1. Figure 3.2 shows an example structure created on a domain of size 10×10 with a porosity of 0.85 and an average structure of 0.25. The procedure described above is capable of generating both two-dimensional and three-dimensional microstructures. For generation of realistic microstructures, statistical descriptors obtained from experimental measurements will have to be used and will need to include additional correlations to ensure adequate connectivity.

3.5 Results and Discussion

This section presents a detailed account of the results obtained using the numerical framework described in the previous section. A few validation studies performed as part of the work are presented first, followed by calculations performed on 2D porous channels.

3.5.1 Validation

As part of the validation exercise of the IBM method, the case of uniform flow over a stationary cylinder is considered. Numerous simulations are performed and the results are compared to experimental or high-resolution numerical results available in the literature. The extent of the domain considered is 45D in the stream-wise direction and 30D in the cross-flow direction. The inlet is maintained at a distance of 20D from the cylinder while the exit is at 25D to avoid any influence of the inflow or outflow boundaries on the flow-field. Calculations are performed for a Reynolds number range of 10-200 based on the cylinder

diameter and inlet velocity. This encompasses both the steady (attached recirculation zones) and unsteady (shedding Karman vortex street) flow regimes. A non-uniform Cartesian grid with hyperbolic tangential vertex distribution is utilized in the flow domain while maintaining a uniform distribution in the vicinity of the IB surface with a total of 80 grid points ($\Delta = 0.0125D$) in each direction across the cylinder.

3.5.1.1 Steady flow regime ($Re \leq 40$)

There is a wealth of experimental and numerical results available in literature for this case. The results from the numerical results of Park et al. [37] who have discussed results in the range of Reynolds numbers matching with the current work and shown good agreement with other experimental works is chosen here for validation. The simulations of Park et al. are performed on a body-fitted mesh on a staggered-grid framework using 128 grid points around the cylinder surface. Table 3.1 presents the coefficients of drag and the lengths of the recirculation zones calculated at various Reynolds numbers and the corresponding numerical results from [37]. Figure 3.3 shows the distribution of coefficient of pressure obtained for each of the three Reynolds numbers around the cylinder. A good agreement is observed in all the cases.

3.5.1.2 Unsteady flow regime ($Re > 40$)

It is well known that for higher Reynolds numbers (> ~40), the recirculation zones become unsteady and shed alternating vortices in the wake called the Karman vortex street. The shedding pattern is characterized by the Strouhal number – a non-dimensional measure of the shedding frequency. For comparison of these results, the experimental results from Norberg [66] and numerical results of Zhang et al. [67] are used. The comparison of the average coefficients of drag and Strouhal numbers are presented in Table 3.2. It is seen that the agreement of current work with past results is good. The difference in Strouhal number compared to the experiments of [66] for Re_D = 200 is due to setting in of three-

dimensional effects in the flow field, while the calculations are performed in a two-dimensional setup. This discrepancy is well documented in the literature [67, 68].

3.5.2 Flow through porous channels

Next, a series of calculations are performed using the developed IBM framework to simulate flows through porous channels. The porous media used are created using either a random arrangement of square blocks or the stochastic reconstruction procedure discussed earlier. This section presents in detail the results obtained from various calculations and related discussions.

3.5.2.1 Computational details

For all the calculations, a two-dimensional channel flow as shown in Figure 3.4 is considered. The length of the channel is three times the channel height H – the first and the last sections are plain channels while the middle section consists of the porous medium. The channel geometry consists of top and bottom stationary walls and inlet and outlet conditions. The measurement of pressure drop is made across the middle section by computing the average pressure across a cross-section perpendicular to the flow direction before and after the porous section. A uniform Cartesian grid is used in all the calculations.

3.5.2.2 Grid sensitivity study

A grid sensitivity study is conducted to ensure the sufficiency of grid resolution in the flow field. The porous medium is generated using stochastic reconstruction procedure described earlier for a porosity of 0.75 and average structure size of $d_p = H/10$. The Reynolds number based on the channel height and inlet velocity is 100. Calculations are performed on three grid levels with grid resolutions of $\Delta/H = 0.005, 0.0025$ and 0.00125. Figure 3.5 shows the reconstructed porous medium geometry used in the calculations. The locations of two cross-sections considered for velocity profile comparison are also shown. The stream-wise velocity profiles at two cross-sections inside the porous medium shown in Figure

3.5 are compared at the three grid levels and plotted in Figure 3.6. It is seen that the agreement among profiles at the three grid levels is good.

In the discussions presented next, the pressure-drop observed across the porous medium is compared with the theoretical predictions using Darcy-Forchheimer equation. Hence a comparison of the pressure drops obtained across the porous section of the channel is provided in Table 3.3. It is seen that the values obtained for pressure drop are in good agreement with each other. Hence for all the calculations presented next, a grid resolution of $\Delta = 0.005H$ in each direction is used.

3.5.2.3 Darcy-Forchheimer equation for pressure drop

The classical way to calculate pressure drop across a homogenous porous medium is to use the Darcy equation with Forchheimer correction [52] given by (dimensional form):

$$-\nabla^* p^* = \frac{\mu^*}{\kappa^*} U_{in}^* + A^* \cdot \rho^* {U_{in}^*}^2 \tag{3.7}$$

where, U_{in} is the average inlet velocity (also termed the superficial velocity), κ^* is the permeability and A^* is the Forchheimer function. The viscous and inertial effects are accounted for by the first and second terms, respectively. The inertial term becomes negligible for very low velocity (Darcy) flows and this equation reduces to the standard form of pressure drop given by Darcy law. Numerous experimental studies have been undertaken in the past to estimate the permeability and Forchheimer's function for a variety of porous geometries. Based on these studies, correlations relating these quantities to the structural characteristics of the porous media such as the porosity and average structure size have been developed and are widely used under certain simplifying assumptions. The permeability is commonly estimated using the Carman-Kozeny equation $\kappa^* = \epsilon^3 {d_p^*}^2 \,/\, 175(1-\epsilon)^2$, while the Forchheimer function is given by $A^* = 1.75(1-\epsilon) \,/\, \epsilon^3 d_p^*$ [69]. Though the Carman-Kozeny equation was developed for spherical particles, it has been used extensively for porous media in the limit of homogeneity and isotropy [70-72].

For porous flow calculations, it is common to use the average size of the porous structures d_p and the porosity ϵ in the definition of Reynolds number, called the particle Reynolds number, given by $Re_p = \rho U_{in} d_p \epsilon \,/\, \mu$. We compare the pressure drop predicted by the simulations to a non-dimensional form of Eq. (3.7), expressed in terms of Re_p, ϵ and d_p given by:

$$\frac{\partial p}{\partial x} = \frac{\epsilon d_p}{Re_p} \cdot \frac{1}{\kappa} + A \tag{3.8}$$

where, the κ and A are non-dimensional equivalents of κ^* and A^*, respectively. In addition to ϵ and d_p found in Eq. (3.8), the values of κ and A are also dependent on the structural characteristics of the porous medium. We would like to study the influence of the porous structure sizes at different flow velocities and hence, in order to reduce the number of independent parameters, we use a fixed porosity value of $\epsilon = 0.85$ for all the calculations presented here.

3.5.2.4 Pressure drop from simulations

Two kinds of porous medium geometries are considered for numerical simulations – the first one composed of square blocks of a specified size that are randomly placed to obtain the required porosity and the second type which is generated using the stochastic reconstruction procedure described in section 3.4.3. Three structure sizes are considered – $d_p = H/40$, $H/20$ and $H/10$. For every structure size, calculations are performed for different inlet velocities and for each of these cases, we create a new configuration of square blocks with appropriate structure size and porosity. Though the statistical descriptors used may be the same for different cases, the actual resultant structures may "look" completely different between different configurations. To highlight this aspect and also the complex nature of the structures generated, the reconstructed geometries for the three d_p values are shown in Figure 3.7 for two cases each.

Figure 3.8 shows the pressure drop values predicted by numerical simulations in comparison to the theoretical values calculated using Eq. (3.8). The plot is provided on a log-log scale for purpose of clarity and hence the actual differences are larger than they appear. It is observed that the agreement with the prediction from Darcy-Forchheimer equation is good for $d_p = H/40$ and $H/20$ and the maximum deviation is within 15% for all the cases considered. For $d_p = H/10$ however, the deviations become relatively larger with a largest value of around 35%. This increase in deviation can be attributed mainly to the increase in the relative size of the porous structures in comparison to the channel geometry. The correlations used for computation of permeability and Forchheimer's function may no longer be accurate since localized effects of fluid flow around the structures start dominating The increased discrepancy especially shows up in the inertial term which exhibits a strong dependence on the geometry of the porous structures. Indeed, the applicability of Darcy-Forchheimer equation (and the two correlations) should be limited to fine-grained homogeneous porous media; the increased structure sizes clearly violate these assumptions. It is in these scenarios that the use of accurate direct numerical simulations to predict flow features becomes a necessity, even when the porous media is only composed of same sized square blocks.

Figure 3.9 shows the computed pressure drops across reconstructed porous channel for different values of Re_p. It is seen that relatively, the deviations from theoretical predictions are larger in these simulations, especially for the two larger structure sizes. Also, the differences are observed to be case dependent; for example, the largest deviation for $d_p = 0.5$ (~50%) is for $Re_p = 1$ while for $d_p = 1.0$, $Re_p = 2.5$ (~110%) and 5 (~62%) exhibit larger differences. Knowing that different geometries are used for each of these simulations, this shows the highly geometry dependent nature of these problems and emphasizes the importance of accurate prediction of localized flow features. As the structure sizes are increased to be comparable to the channel dimensions, the local geometric characteristics dominate the flow field and hence influence the observed pressure drops, highlighting the need for direct numerical simulations to accurately predict flow in realistic porous media. In conclusion, as has been shown in the past [72-74], the

use of macroscopic relations like Darcy-Forchheimer equation is limited to homogeneous and isotropic porous media. In the case of any increased geometric complexity or higher flow rates which may result in unsteadiness and eventually turbulence, use of accurate direct numerical simulations maybe the only way forward.

3.5.3 CO_2 diffusion through porous spherical particles

Next, to demonstrate the applicability of the developed framework to a three-dimensional problem, we consider calculations to simulate diffusion of CO_2 through porous spherical particles and study the total time to saturation for different particle porosities. The particle geometry is created using the stochastic reconstruction procedure explained earlier. A random arrangement of spheres is used to generate the input correlations. Figure 3.10 shows a reconstructed porous spherical particle of diameter 100 microns and porosity of 0.45. In these calculations, it is assumed that the diffusion process is driven purely by the presence of local concentration gradients and hence the convective terms in the governing equations are neglected.

A uniform discretization consisting of 200 mesh points across the diameter is used in the vicinity of the particle. The particle is placed within a cubic domain consisting of 15% CO_2 and 85% N_2 initially. The boundaries of the domain are set up to enforce equilibrium with the ambient conditions and thus act as infinite sources of 15% CO_2 while a zero-gradient (Neumann) boundary condition for the species concentrations is used at thepore surfaces. The mass fraction of CO_2 is initially set to 0% in the pore space of the particle, while the remainder is constituted by the carrier species (N_2). The particle is said to be saturated with CO_2 when the average mass fraction of CO_2 inside the particle is 95% of the ambient CO_2 mass fraction. Porosities in the range 0.2-0.6 are considered for the simulations and the computed diffusion times are shown in Figure 3.11. It is observed that for higher porosities (> 0.4), the total time for saturation shows an asymptotic behavior. As the porosity of the particle is decreased below 0.4, a steep

increase in the diffusion time is observed. This is expected due to reduction in the number of approach paths to the pore spaces in the interior of the particle. While these are only preliminary calculations, they demonstrate the use of the developed methodology in complex three-dimensional pore spaces. In future, such simulations can explore a broad spectrum of porous media flow problems and improve our fundamental understanding of the subject.

3.6 Influence of stochasticity on saturation times

Use of a stochastic procedure for the porous geometry creation affects the simulation behavior. For example, in the previous section, the particular geometry used for the diffusion simulations affects the overall saturation times. In order to assess the effect of the stochasticity of the geometry, simulations are performed through two-dimensional porous circular particles. The problem set-up is similar to the CO_2 diffusion in porous spherical particles explained earlier. The particle considered is 100 microns in diameter and a total 200 grid points are used across the particle diameter. The particle porosity is 0.6. A total of 25 simulations are performed and the time to saturation is computed for each of the simulations. From these computations, the average time to saturation is observed to be 0.30 ms while the standard deviation is calculated to be 0.02 ms. Hence, the distribution of the values for different geometries is within a small range – the standard deviation is less than 7% of the mean value while the maximum absolute deviation from the mean is 18%. Consequently, it is established that the results indeed converge to an average value and that the deviation from the mean value is also within acceptable limits given the inherent random nature of the geometry creation process.

3.7 Summary and Conclusions

The primary contribution of this work is development of a framework for performing computations through complex pore-space geometries in a straight-forward way and studying flow regimes wherein application of empirical formulations may be inaccurate. In order to create realistic porous media, a

stochastic reconstruction procedure based on simulated annealing algorithm is used. The framework is applied to porous channel flows and the computed pressure drops are compared to predictions using Darcy-Forchheimer equations. Use of analytical expressions is subject to inaccuracies when the porous geometry tends towards heterogeneity. The simulations demonstrate the capability of the developed methodology in simulating flows through complex porous morphologies and the importance of performing such studies. This lays a foundation for studying macroscopic properties of realistic porous media such as permeability in relation to the various flow regimes, including turbulence. CO_2 diffusion simulations are performed on reconstructed spherical porous particles for varying porosities showing the extension of the developed framework to three-dimensional problems.

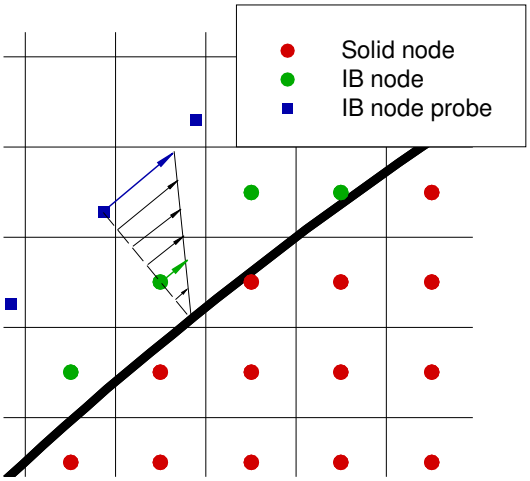

Figure 3.1 A schematic representation of the solid node, IB node and its probe for a circular IB surface

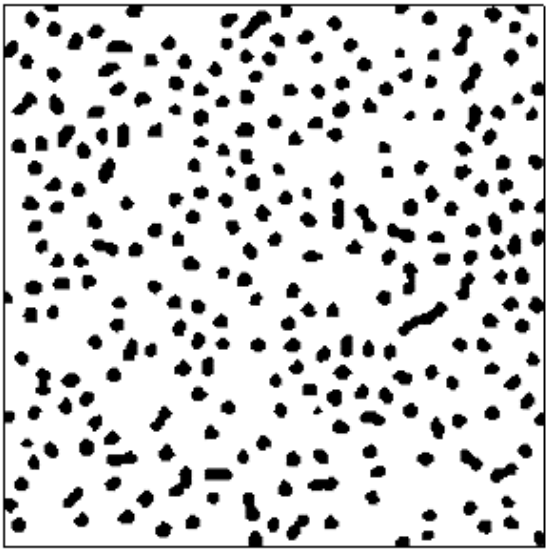

Figure 3.2 A 2-D reconstruction with porosity of 0.75 and average structure size of 0.25 generated on a 200×200 grid (black represents solid region)

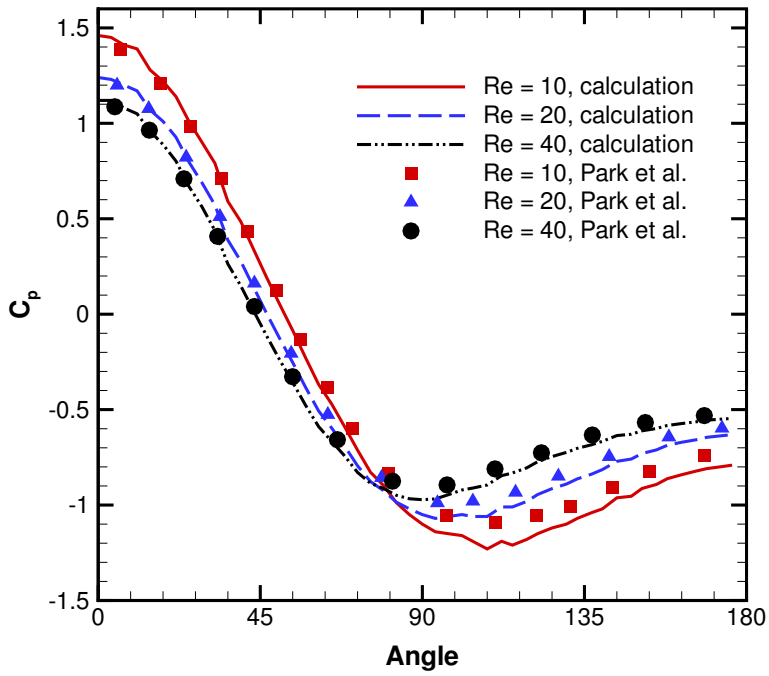

Figure 3.3 Distribution of pressure coefficients obtained around the cylinder surface at various Reynolds numbers for the stationary cylinder

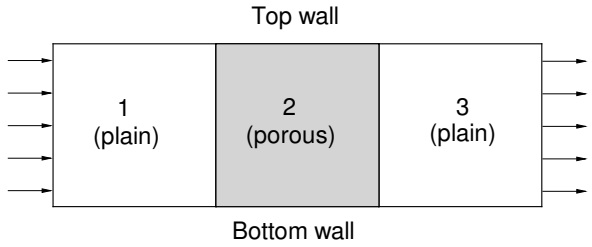

Figure 3.4 Schematic representation of the porous channel geometry

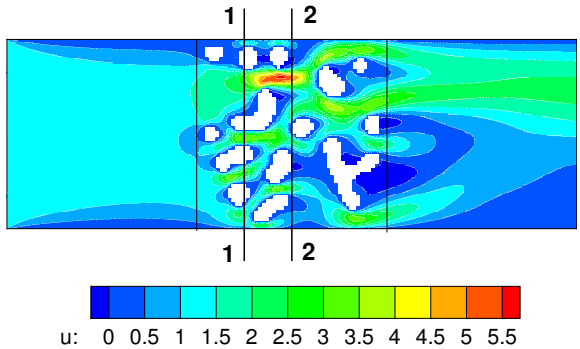

Figure 3.5 Porous channel geometry used for the grid sensitivity study showing the stream-wise velocity contour

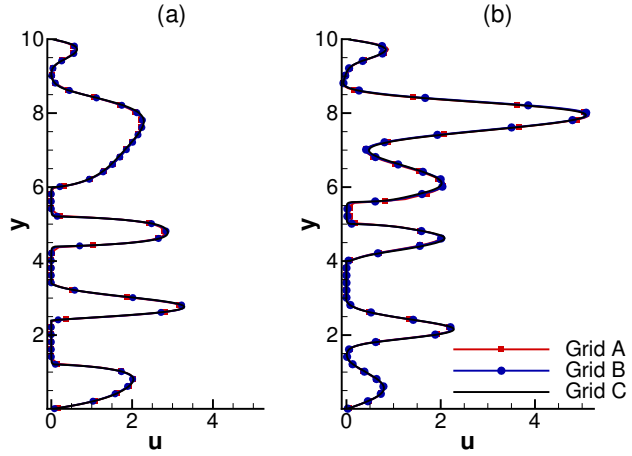

Figure 3.6 Comparison of u velocity profiles obtained at the three grid levels at (a) section 1 and (b) section 2

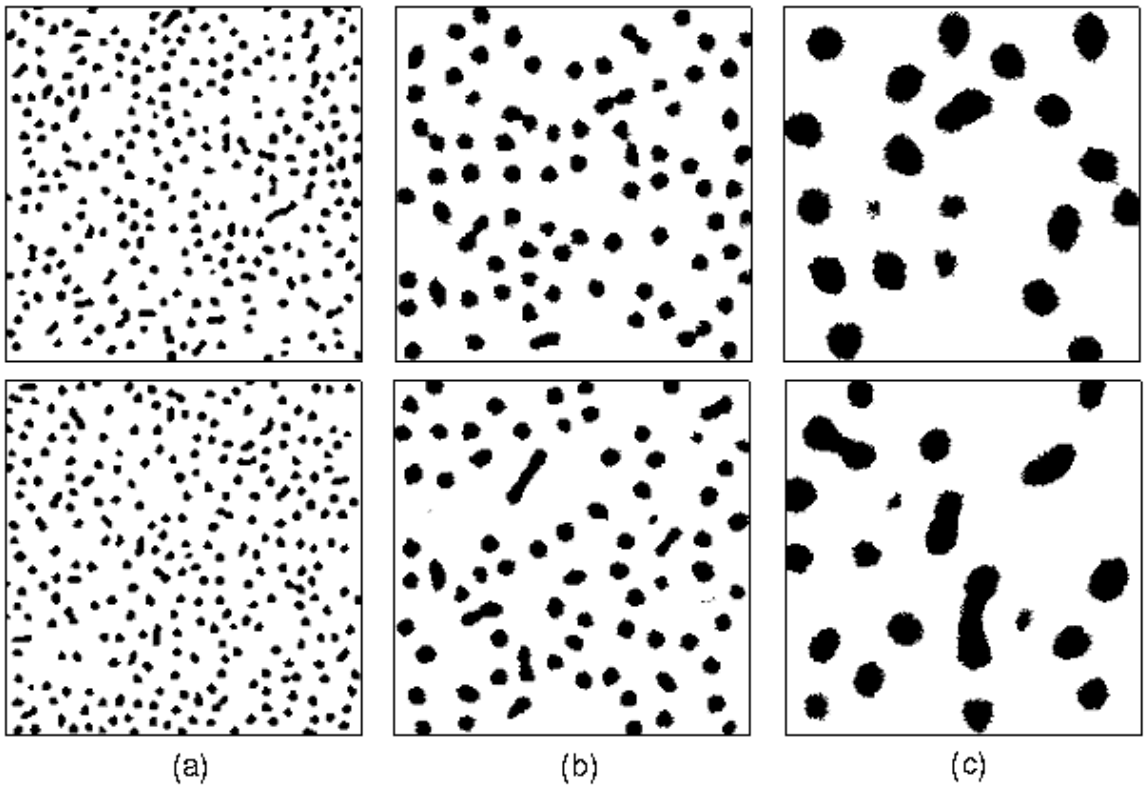

Figure 3.7 Enlarged views of realizations obtained using stochastic reconstruction procedure for d_p values of (a) 0.25, (b) 0.50 and (c) 1.00. The porosity for each of these cases is fixed at ϵ = 0.85.

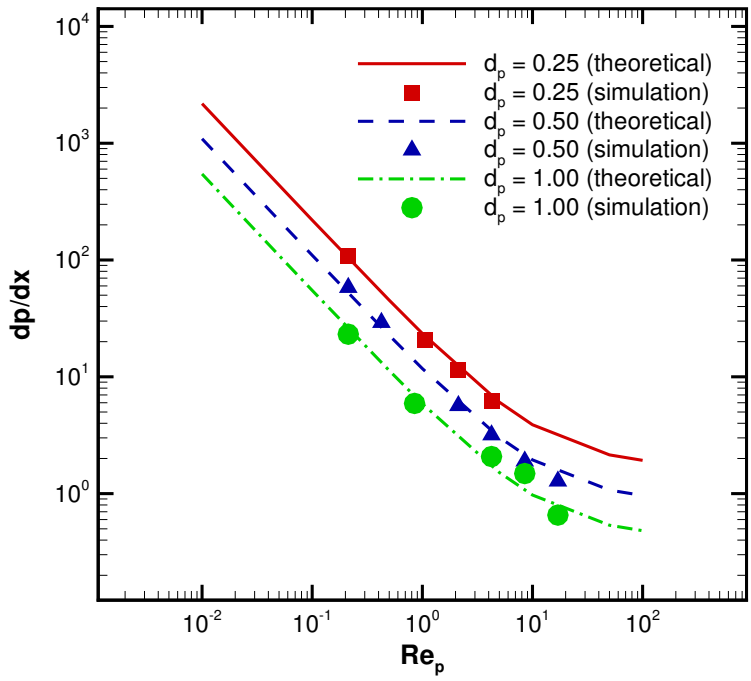

Figure 3.8 Comparison of pressure drops from simulations and Darcy-Forchheimer equation for porous channel constructed using square blocks

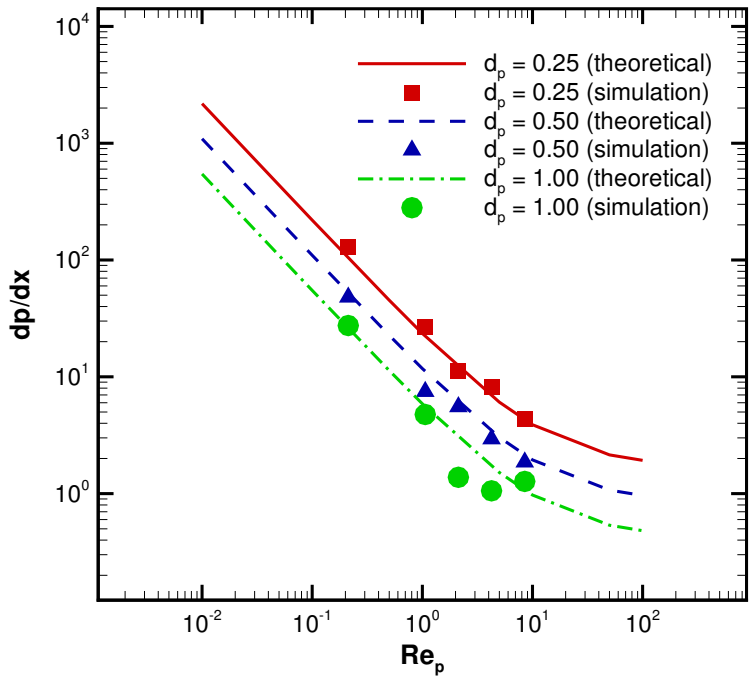

Figure 3.9 Comparison of pressure drops from simulations and Darcy-Forchheimer equation for porous channel constructed using stochastic reconstruction

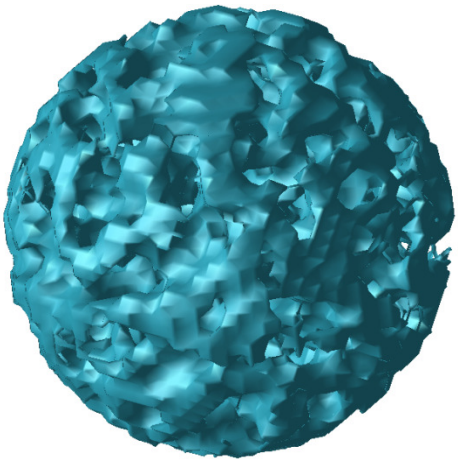

Figure 3.10 A 3-D porous spherical particle of diameter 100 microns and porosity of 0.45

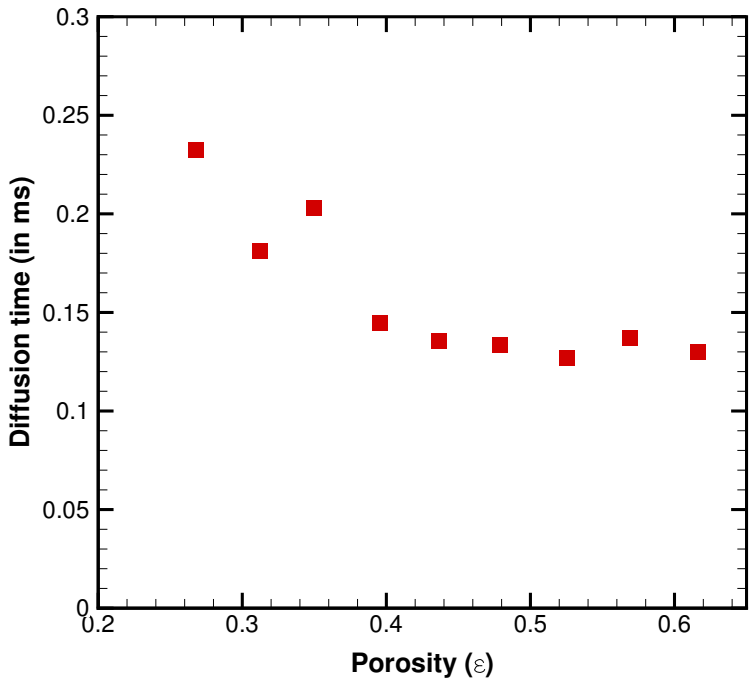

Figure 3.11 Computed diffusion times for porous spherical particles of varying porosities

Table 3.1 List of coefficients of drag and wake lengths computed for uniform flow over a stationary cylinder at various Reynolds numbers

Reynolds number	**Coefficient of drag**		**Wake length**	
	[37]	**Present**	**[37]**	**Present**
10	2.78	2.80	0.25	0.25
20	2.01	2.00	0.95	0.94
40	1.51	1.54	2.30	2.27

Table 3.2 Strouhal numbers obtained at different Reynolds numbers and the comparison with existing experimental and numerical results

Reynolds number	C_D		**Strouhal number**		
	[67]	**Present**	**[66]**	**[67]**	**Present**
100	1.45	1.43	0.165	0.170	0.166
150	1.40	1.39	0.185	0.190	0.185
200	1.40	1.38	0.181	0.202	0.198

Table 3.3 Non-dimensional pressure drops observed across the porous section

Grid	**Total grid size**	**Resolution** $\boldsymbol{\Delta/H}$	**Pressure-drop** ($\boldsymbol{dp/dx}$)
A	600×200	0.005	2.35
B	1200×400	0.0025	2.36
C	2400×800	0.00125	2.36

Chapter 4
A Sub-pore Model for Multi-Scale Reaction-Diffusion Problems in Porous Media

4.1 Abstract

Applications of reaction-diffusion systems in porous media pose a challenging problem for computational modeling approaches due to their multi-physics and multi-scale nature. In this work, a length scale based dual approach is proposed – the larger pore channels (macro-pores) are resolved using conventional numerical techniques and a novel 'sub-pore' model is used to account for the unresolved pore channels (sub-pores) and the important physics therein. This chapter provides the details of the sub-pore modeling technique. In this chapter, a novel methodology that accounts for all the length scales and physical phenomena involved in a single framework is described. The porous network in the sub-pore system is composed of a fractal-like hierarchical system of straight cylindrical pores. Simplified governing equations for mass and energy transport are solved for within the sub-pore system along with a reaction kinetics model to account for surface adsorption. An implicit coupling strategy is used to couple the macro-pore and the sub-pore systems so as to ensure conservation. The developed methodology is then applied to a number of test cases. This includes pure diffusion and adsorption simulations which are performed to assess the individual process time scales. It is established that the proposed framework is necessary for problems where the adsorption time scale is much smaller than (diffusion-limited) or comparable to the diffusion time scale. The diffusion-limited case is shown to be applicable to CO_2 adsorption process on meso-porous silica. This case is explored further by way of parametric studies, demonstrating the capabilities of the proposed methodology.

4.2 Introduction

Diffusion and adsorption in porous media have found a number of successful applications in processes involving separation of a variety of gaseous mixtures [75-78]. One of the prime examples for the use of these technologies is its application to carbon capture [1, 79-81]. These processes involve use of highly porous materials which, owing to the large amount of surface area, are ideal for a surface phenomenon like adsorption. Porous media are typically categorized based on the size of the predominant pore channels that they are composed of and are divided into three types – macro-porous (> 50 nm), meso-porous (2-50 nm) and micro-porous (< 2 nm) solids. Smaller pore channels result in increased surface area available per unit mass of the material and hence meso-porous and micro-porous solids find numerous applications in a variety of adsorption-based separation processes.

In terms of physical phenomena involved, these systems involve diffusion of mass (and possibly energy) into a network of pore channels and a subsequent adsorption reaction with the surfaces of the porous media. The mathematical and numerical aspects of the classic reaction-diffusion problem that these systems represent have been studied in great detail in the past [82, 83]. It is routinely observed that the time scales governing the reaction and diffusion terms can be quite different [84] and hence these problems pose a challenging task for any computation-based approach.

The next issue, also related to scaling, is that of widely differing pore channel sizes contained in porous media. Porous materials generally exhibit a distribution of pore channel sizes rather than being composed of uniformly sized pores. In fact, the length scales in many porous media used for adsorption usually span over 3-4 orders of magnitude. For example, meso-porous silica particles that are used as sorbent material for CO_2 separation from flue gases are sized around 100-200 microns while the smallest channels contained in them are as small as 25-30 nm. The impact of such a wide-ranging length scale variation is dual – it introduces additional time-scale disparity and affects the dominant physical phenomena. It follows that it is near impossible to perform numerical simulations resolving all these length scales and

the relevant physics in a single framework. The main objective of this work is to develop a feasible and cost-effective numerical approach which is geared towards such multi-scale reaction-diffusion problems involving porous media.

Considering the effect of the complex network of pore channels on mass transport alone, it has been shown in the past that the diffusion process depends strongly on the nature of the porous structure underneath [85, 86]. Attempts have been made in the past to account for these varying pore channel sizes in a number of ways. Most common approaches include modeling them as a network of interacting or non-interacting capillaries [87, 88] and their subsequent use in either homogeneous or heterogeneous single porous particle systems wherein the effect of the pore size distribution is modeled using integrations performed over the entire pore size range [76]. For example, flux expressions for the diffusion into the void space of porous particles have been derived by assuming a network of cylindrical capillaries capable of satisfying arbitrary pore size distributions [89, 90]. Simons and coworkers [85, 91, 92] described the use of a "pore tree" structure to model gasification in coal char. In the pore tree, the network of capillaries form a river- or tree-like system wherein the larger channels break down into smaller ones and so on, and the diffusion and reaction processes are modeled analytically (using suitable integrations). Another alternative approach is to look at porous media as being composed of fractal pores [86, 93, 94] and use an effective diffusion coefficient in the formulation of the species diffusion equation.

In the current work, a contrasting approach, in terms of handling of the pore structure, is presented by attempting to resolve all the important length scales directly in a single numerical framework. This task is however not straight-forward given the multi-scale nature of the problem and the multiple physical phenomena involved. The main aim of the present paper is to develop a numerical methodology which captures all the important scales and dominant physical phenomena in a general reaction-diffusion system in porous media.

4.3 Methodology

It is essential that the proposed scheme is computationally tractable for practical applications and yet captures the dominant physics at all the length scales involved. In view of this, it is proposed to approach the problem using a length scale based modeling strategy – the larger channels are simulated using a pore-resolving approach by employing immersed boundary method (IBM) while the remaining pore channels that are unresolved are modeled using a 'sub-pore' modeling methodology. The idea of dual modeling is analogous to the sub-grid scale modeling used in simulation of turbulent flows wherein the large, energy carrying flow structures are resolved on a relatively coarse grid and any of the unresolved scales are modeled to include the important physics that dominate these smaller length scales.

4.3.1 Elements of sub-pore geometry

The geometry in the sub-pore system is constructed as a hierarchical system of pore channels with larger channels branching into smaller ones and so on. This is similar in essence to the "pore tree" geometry proposed by Simons and coworkers [91, 92]. While the geometry construction is similar, it should be pointed out that the pore tree model presents a continuous size distribution (termed 'continuous branching model' by the authors in [92]). In comparison, the current model approaches the problem in a discrete fashion, thus rendering it ideal for numerical simulations. Figure 4.1(a) shows an illustration of the pore branching model used for the sub-pore geometry. Every 'level' defines the structures of a particular size with level 1 representing the largest channels and higher levels representing incrementally smaller channels. In the example schematic, structures at every level branch into two structures of the next level and so on and once the entire structure is constructed, it can be imagined to form a tree-like structure. Like in any self-similar fractal structure, the geometric entities at all levels are similar except for a length scaling factor which is provided as part of the sub-pore geometry definition. In order to keep the implementation of the physical models to be satisfied within this system tractable, the channels are chosen to be cylindrical which allow one-dimensional assumption for the models. A schematic of such a structure

is shown in Figure 4.1(b). The sub-pore system is present at the solid surface of the macro-pore geometry and hence can be imagined to exist underneath every macro-pore cell that forms a boundary with the solid surface of the macro-porous medium.

In construction of the sub-pore geometry, it is essential to identify the minimum set of input geometrical parameters necessary to create this geometry. Since the eventual goal of this framework is to represent the pore channel network that cannot be directly resolved, it is best to utilize experimental data that helps perform this operation. It is common practice to characterize a given porous medium by an experimentally measured pore size distribution (PSD). A pore size distribution provides the contribution of channels of different sizes in the porous medium to the overall pore space volume. Hence, given a PSD, the size range of pore channels that will need to be modeled using the sub-pore methodology can be derived. Once the size range is known, the data from the PSD can be used in the following manner.

Assuming that n_l number of levels are used in the sub-pore system, and that the length scaling of level i with respect to the base level (that is level 1) is given by s_i. This means that any length L_i belonging to level i can be computed using the corresponding length L_1 belonging to level 1 and s_i to get the value of $L_i = L_1 s_i$. By extension, any area element will scale as the square of s_i, while any volume element will scale as the cube of s_i. The values of s_i's can be derived from the PSD as has been discussed next.

The total volume contributed by channels of level i in all the sub-pores through the porous medium can be calculated as:

$$\Delta \mathbb{V}_i = n s_i^3 \mathbb{V}_1 n_{b_i} \tag{4.1}$$

where, n is the total number of sub-pores, $\mathbb{V}_1$ is the pore-space volume of one channel of level 1 and n_{b_i} is the number of branches of level i existing in every sub-pore. In the above expression, the values of n and n_{b_i} are yet to be determined. In order to relate the actual volume contribution of a given level to the PSD, the fractional contribution of the given level to the total volume needs to be calculated:

$$\theta_i = \frac{\Delta \mathbb{V}_i}{\sum_{i=1}^{n_l} \Delta \mathbb{V}_i} = \frac{n_{b_i} s_i^3}{\sum_{i=1}^{n_l} n_{b_i} s_i^3} \tag{4.2}$$

The above equation when written out for all the n_l levels forms a simultaneous set of equations satisfying a trivial solution with all the n_{b_i}'s being equal to 0. In order to avoid the trivial solution, one of the n_{b_i}'s needs to be constrained and then any n_l – 1 equations be solved to obtain a non-trivial solution. The definition of the sub-pore geometry requires that the every sub-pore starts with a single structure of level 1. Hence in Eq. (4.2) above, the number of branches for the first level i.e., n_{b_1} is equal to 1. Also, since the scaling is performed with respect to the level 1, s_1 is equal to 1. Assuming the values of n_{b_1} and s_1 to be known quantities and rearranging leads to a linear equation in terms of n_{b_i}'s:

$$(s_2^3\theta_i)n_{b_2} + (s_3^3\theta_i)n_{b_3} + \cdots + \left(s_i^3\theta_i - s_i^3\right)n_{b_i} + \cdots + \left(s_{n_l}^3\theta_i\right)n_{b_{n_l}} = -(s_1^3\theta_i)n_{b_1}$$

Using the values of $s_1 = 1$ and $n_{b_1} = 1$, and dividing by θ_i throughout:

$$(s_2^3)n_{b_2} + (s_3^3)n_{b_3} + \cdots + \left(s_i^3(1 - 1/\theta_i)\right)n_{b_i} + \cdots + \left(s_{n_l}^3\right)n_{b_{n_l}} = -1 \tag{4.3}$$

The ith term, ass seen in Eq. (4.3) above, has an additional term in the coefficient. A set of n_l – 1 simultaneous equations are obtained by writing the above equation for i = 2 to n_l. The final form is as follows:

$$\begin{pmatrix} s_2^3(1-1/\theta_2) & s_3^3 & s_4^3 & \cdots & & \ddots & \\ s_2^3 & s_3^3(1-1/\theta_3) & s_4^3 & & & \vdots & \\ & \vdots & & \ddots & & & \\ & \ddots & & \cdots & s_{n_l-2}^3 & s_{n_l-1}^3(1-1/\theta_{n_l-1}) & s_{n_l}^3 \\ & & & & s_{n_l-2}^3 & s_{n_l-1}^3 & s_{n_l}^3(1-1/\theta_{n_l}) \end{pmatrix} \times \begin{pmatrix} n_{b_2} \\ n_{b_3} \\ n_{b_4} \\ \vdots \\ n_{b_{n_l-1}} \\ n_{b_{n_l}} \end{pmatrix} = \begin{pmatrix} -1 \\ -1 \\ -1 \\ \vdots \\ -1 \\ -1 \end{pmatrix} \tag{4.4}$$

The number of branches at each level n_{b_i} can be hence computed using a solution to the above matrix formulation. Given that the number of levels is usually a small number, the matrix size is expected to be small and hence direct inversion works well for most cases.

The other physical parameter that is desirable to be matched is the specific surface area available, especially for surface phenomena such as adsorption on the porous surface. To help ensure that the constructed geometry matches a given specific surface area A_s, the number of sub-pores on the porous medium n is used.

The total additional surface area available per sub-pore is the summation of the surface areas available due to structures at every level and can be expressed as:

$$\Delta A_{sp} = A_1 + A_2 + \cdots + A_{n_l}$$

where, A_i's are the total additional areas available at each level. As mentioned earlier, the area element will vary as the square of the scaling factor s_i. Noting that a hierarchical geometry is used, each of the levels are composed of geometries that are similar but scaled according to the scaling ratio s_i. Also, since these are the total areas, contributions due to all the branches present at a particular level are to be accounted for.

$$\Delta A_{sp} = A_1\left(s_1^2 n_{b_1}\right) + A_1\left(s_2^2 n_{b_2}\right) + A_1\left(s_3^2 n_{b_3}\right) + \cdots + A_1\left(s_{n_l}^2 n_{b_{n_l}}\right)$$

$$\Delta A_{sp} = A_1 \sum_{i=1}^{n_l} \left(s_i^2 n_{b_i}\right) \tag{4.5}$$

The amount of surface area added for one sub-pore configuration is then used to determine the number of such sub-pore configurations that should exist underneath unit area of the macro-porous surface. In order to this, an expression for the total area on the porous medium is written as:

$$A = A_{mp} + A_{sp} = A_{mp} + n\,\Delta A_{sp} \tag{4.6}$$

where, the subscripts mp and sp indicate contributions due to macro-pore and sub-pore channels, respectively. The addition of the sub-pore system however also introduces additional pore space in the medium. This change in the pore space should hence be reflected in the calculation of the specific surface area as well. An expression similar to Eq. (4.6) can be written for the total pore volume in the porous medium:

$$\mathbb{V} = \mathbb{V}_{mp} + \mathbb{V}_{sp} = \mathbb{V}_{mp} + n\,\Delta\mathbb{V}_{sp} \tag{4.7}$$

Now, if $\mathbb{V}_p$ represents the total volume and ρ_t the true density of the porous medium, the specific surface area is given by:

$$A_s = \frac{A}{\rho_t\left(\mathbb{V}_p - \mathbb{V}\right)} \tag{4.8}$$

As mentioned earlier, the specific surface area is an input parameter to the determination of the sub-pore geometry and hence is a known quantity. After substituting Eqs. (4.6) and (4.7), expansion and simplification of Eq. (4.8) above can be used to compute n_{sp}, the total number of sub-pore systems per unit area of the macro-pore surface, to obtain a desired value of the specific surface area A_s.

$$n_{sp} = \frac{n}{A_{mp}} = \frac{\rho A_s\left(\mathbb{V}_{par} - \mathbb{V}_{mp}\right) - A_{mp}}{\Delta A_{sp} + \rho A_s \Delta \mathbb{V}_{sp}} \cdot \frac{1}{A_{mp}} \tag{4.9}$$

4.3.1.1 Example 1: A uniform pore-size distribution

In this example, a macro-porous medium of porosity 0.5 is considered which exhibits a uniform PSD across all the pore channel sizes ranging between 1000 and 62.5 nm. Also, the macro-porous volume of the medium is 10^{-10} m^3 and the surface area is 10^{-5} m^2. Assuming a true density of ρ_t = 1000 kg/m^3, the specific surface area of the macro-porous medium is 200 m^2/kg while the desired value is 50000 m^2/kg, i.e., a 250 times increase in the value due to introduction of the sub-pore geometry. Details about deducing the sub-pore geometry are discussed next.

For sake of simplicity, the scaling ratio between successive levels is assumed to be a constant. The scaling ratio is equal to 0.25 and there are 3 levels in all. The corresponding values of scaling ratios will hence be s_1 = 1; s_2 = 0.25; s_3 = 0.0625. The first level structures have a diameter of 1 micron and consequently, the second and third level structures will have diameters of 0.25 and 0.0625 microns, respectively. A uniform PSD means that the volume contribution of the individual levels is equal to a constant value – i.e., $\theta_1 = \theta_2 = \theta_3 = 1/3$ – the value being a result of the total number of levels being 3.

For the current example, the two equations obtained by substituting the above values into Eq. (4.3) presented earlier will be:

$$0.25^3\left(1 - \frac{1}{3}\right)n_{b_2} + 0.0625^3 n_{b_3} = -1$$

$$0.25^3 n_{b_2} + 0.0625^3\left(1 - \frac{1}{3}\right)n_{b_3} = -1$$

Upon solving these equations, the values of n_{b_2} and n_{b_3} come out to be 64 and 4096, respectively. Using the values of n_b's and the other input data, value of n_{sp} is determined to be 9.58×10^5 sub-pores per m^2 area of the macro-pore surface, which ensures that the desired value of specific surface area is satisfied.

4.3.1.2 Example 2: An ad-hoc geometry

Now, an example is considered wherein the PSD is not known. For this case, geometrically self-similar structures are assumed at all levels with a constant ratio s between successive levels, the following can be written about the scaling ratios' s_i:

$$s_2/s_1 = s_3/s_2 = \cdots = s_{n_l}/s_{n_l-1} = s$$

$$s_i = s_1 \cdot s^{i-1} = s^{i-1}$$

The value of s can be calculated using the smallest and largest channel diameters in the sub-pore geometry:

$$s = \left(\frac{d_{min}}{d_{max}}\right)^{\frac{1}{n_l-1}}$$

Also, if the PSD is not known a priori, the values of n_{b_i} also will have to be specified. Here, a simplified geometry is created assuming that the n_{b_i} values increase as per a geometric progression with the increasing level number. This means that the ratio between the number of branches at successive levels is a constant equal to n_b:

$$n_{b_2}/n_{b_1} = n_{b_3}/n_{b_2} = \cdots = n_{b_{n_l}}/n_{b_{n_l-1}} = n_b$$

$$n_{b_i} = n_{b_1} \cdot n_b^{i-1}$$

For this case, the final expression for the total surface area available per sub-pore given in Eq. (4.5) simplifies as a geometric series. Using $n_{b_1} = 1$, the total additional area per sub-pore can be written as follows:

$$\Delta A_{sp} = \sum_{i=1}^{n_l} A_1\left(s_i^2 n_{b_i}\right) = A_1 \sum_{i=1}^{n_l} (s^2 n_b)^{i-1} = A_1 \cdot \frac{(s^2 n_b)^{n_l} - 1}{s^2 n_b - 1}$$

Similarly the increase in overall pore space volume due to introduction of one sub-pore is written below:

$$\Delta \mathbb{V}_{sp} = \sum_{i=1}^{n_l} \mathbb{V}_1\left(s_i^3 n_{b_i}\right) = \mathbb{V}_1 \sum_{i=1}^{n_l} (s^3 n_b)^{i-1} = \mathbb{V}_1 \cdot \frac{(s^3 n_b)^{n_l} - 1}{s^3 n_b - 1}$$

If desired, even for this simplified geometry, the values of s and n_b can be selected such that additional physical constraints are satisfied. For example, if it is desired that the surface area contribution of the smaller levels should be larger, but the volume contribution should be lesser, the following conditions are to be satisfied:

$$s^2 n_b > 1$$

$$s^3 n_b < 1$$

4.3.2 Modeling macro-pore transport

The larger pore channels, here onwards referred to as the macro-pore channels, are resolved directly in the current approach. Any porous structure is typically composed of a complex network of interconnected pore channels and it is a challenging task to perform pore-resolved simulations through these intricate structures. In this work, the immersed boundary method (IBM) is employed for this purpose. IBM offers a boundary non-conforming approach to resolving flows through complex geometries. The current IBM implementation is within the framework of an in-house code GenIDLEST [28] (Generalized Incompressible Direct and Large Eddy Simulation of Turbulence) and has been extensively validated and

applied in a wide range of fluid flow and heat transfer problems [34, 95, 96]. The applicability of this framework to complex reconstructed porous media geometries including to problems involving species diffusion has been shown to be a promising avenue for simulations involving realistic porous media [96].

At the macro-pore level, governing equations are solved to compute the transport of mass and energy. The general form of the diffusion equation that is solved numerically is given below using Einstein's index notation:

$$\frac{\partial \phi}{\partial t} + \frac{\partial}{\partial x_j}\left(u_j \phi\right) = \frac{\partial}{\partial x_j}\left(\alpha \frac{\partial \phi}{\partial x_j}\right) + \omega \tag{4.10}$$

where, ϕ represents the quantity of interest, u is the velocity, α is the diffusivity and ω is a source term. While solving for energy diffusion, ϕ is replaced by the total energy $\rho C_p T$ where ρ and C_p are the mixture density and specific heat, respectively, T is the temperature and α represents the thermal diffusivity. For the diffusion of species in a multi-component system, ρy^c is the system variable wherein y^c is the component mass fraction and α is replaced by the binary diffusion coefficient D, computed with respect to the carrier species.

It is assumed that the individual components except the carrier species are present in a dilute proportion thus eliminating the need to consider diffusion coefficient for a multi-component system. Since the main goal of this paper is to highlight the different aspects of the sub-pore modeling methodology, the velocity components are assumed to be negligible. This means that the problems considered are purely diffusive in nature and hence the convective term in the equation above is eliminated. The linear systems resulting in the implicit treatment of the above equations are solved using a pre-conditioned BiCGSTAB method.

The above formulation involves use of certain physical properties of the gaseous mixture under consideration – i.e., the specific heat C_p, the density ρ, the thermal conductivity κ and the binary diffusion

coefficient D. Of these, the values of C_p, ρ and κ can depend on the mixture composition and also the temperature, while the value of D varies only with temperature.

The ideal gas law is used to calculate the dependence of the individual component densities on the temperature and pressure:

$$\rho_i = \frac{P}{R_i T} \tag{4.11}$$

where, R_i is the specific gas constant of component i. Alternately, given the density at a temperature T_0, the density at any temperature T would be given by:

$$\rho_i = \frac{\rho_0 T_0}{T} \tag{4.12}$$

These ρ_i's can be combined with the mass fractions to calculate the mixture density:

$$\frac{1}{\rho} = \sum_{i=1}^{n} \frac{y_i}{\rho_i} \tag{4.13}$$

The temperature dependence, on the other hand, of the thermal conductivity of the individual components is calculated using Sutherland's law [97]:

$$\frac{\kappa_i}{\kappa_{i,0}} = \left(\frac{T}{T_0}\right)^{\frac{3}{2}} \cdot \frac{T_0 + S}{T + S} \tag{4.14}$$

where, S is the Sutherland constant and $\kappa_{i,0}$ is the known component thermal conductivity at a temperature T_0. The component thermal conductivities are then used along with the mass fractions to compute the mixture thermal conductivity using a semi-empirical formula [97]:

$$\kappa = \sum_{i=1}^{n} \frac{x_i \kappa_i}{\sum_{j=1}^{n} x_j \eta_{ij}} \tag{4.15}$$

$$\eta_{ij} = \frac{\left(1 + \left(\kappa_i/\kappa_j\right)^{\frac{1}{2}} \left(M_j/M_i\right)^{\frac{1}{4}}\right)^2}{\left(8 + 8M_i/M_j\right)^{\frac{1}{2}}}$$

where, x and M are the component mole fraction and molecular weights, respectively. The mole fractions are calculated directly from the mass fractions and molecular weights:

$$x_i = \frac{y_i/M_i}{\sum_{j=1}^{n}\left(y_j/M_j\right)}$$

In contrast to other fluid properties, the variation of specific heats with change in temperature is usually smaller. Hence, no temperature dependence for values of specific heat is considered in the simulations. The mixture specific heat hence is calculated simply as a function of the component mass fractions and the known reference specific heats:

$$C_p = \sum_{i=1}^{n} C_{p_i} y_i \tag{4.16}$$

As mentioned earlier, the assumption of all the components being present in dilute quantities implies that the component binary diffusion coefficients are independent of the composition and are to be specified for every component with respect to the carrier species only. It does however show a strong variation with change in temperature. The Chapman and Cowling correlation for the binary diffusion coefficient derived from kinetic theory considerations is as follows [98]:

$$D = \frac{1.8337 \times 10^{16}\, T^{\frac{3}{2}} [(M_1 + M_2)/M_1 M_2]^{\frac{1}{2}}}{P \sigma_{12}^2 \Omega_D} \tag{4.17}$$

where, σ_{12} is the effective collision diameter and Ω_D is the diffusion collision integral. Details about computing these values and tabulated values for common gaseous components can be found in [97].

4.3.3 Modeling sub-pore transport

Three physical mechanisms are modeled within the sub-pore system – energy diffusion, mass diffusion and adsorption of species onto the sub-pore surface. The governing equations for the two diffusion processes are of the same form as described earlier for the macro-pore system. Details concerning specifically to diffusion within the sub-pore system, and the reaction kinetics equations are described next.

4.3.3.1 Mass transport

The presence of channels of varying sizes necessitates accounting for different mechanisms that can be responsible for diffusive process. Diffusion of species in porous solids is often accounted for by three different mechanisms – bulk diffusion, Knudsen diffusion and surface diffusion. Brief descriptions of these mechanisms are provided here.

- *Bulk diffusion:* transport resulting due to existing concentration gradients caused by the inter-molecular collisions of the diffusing species
- *Knudsen diffusion:* transport due to collision of diffusing molecules with the solid surface; its effects become significant as the pore channel size approaches the mean free path of the molecular species because the molecule-wall collisions will occur more frequently than inter-molecular collisions
- *Surface diffusion:* transport of molecules along the surface of the pore channels.

Among these, the bulk and Knudsen diffusion effects are the most significant and are accounted for in the current study. The effects of surface diffusion are ignored since the main interest of the current study is transport in the pore space of the sub-pore geometry.

Fickian formulation is assumed to be valid for unsteady diffusion and can be used for both the bulk and Knudsen diffusion process. Hence, the governing equation for mass diffusion solved within the sub-pore system is the same as the one used in the macro-pore diffusion (given in Eq. (4.10)).

The inclusion of two (or more) mechanisms in the diffusion process requires suitable modification to the diffusion coefficient term used in the governing equation. In order to account for the Knudsen diffusion effects that might become important in the smaller channels, the Bosanquet formula is used to compute the effective diffusion coefficient [99]:

$$\frac{1}{D_{eff}} = \frac{1}{D_{bulk}} + \frac{1}{D_{Kn}} \tag{4.18}$$

where, D_{bulk} and D_{Kn} are bulk and Knudsen diffusion coefficients, respectively. The resistances to diffusion due to different mechanisms can be in general compared to electrical resistance networks and the above formulation is a result of the same [100]. The above expression defaulting to the smaller of the two values if the other coefficient is relatively large – hence the effective diffusion coefficient would become very close to the value of D_{Kn} at very small scales and to D_{bulk} in large channels.

The equation for D_{bulk} was provided earlier. On similar lines, the formulation for D_{Kn} is also computed based on kinetic theory considerations [98] and is given below:

$$D_{Kn} = \frac{d_{pore}}{3}\sqrt{\frac{8R_uT}{\pi M}} \tag{4.19}$$

The existence of Knudsen effects is due to the increase in molecule-wall collisions as the channel size decreases. As the channel size approaches the mean free path of the molecules, molecule-wall collisions occur far more frequently than the inter-molecular collisions and the use of D_{Kn} described above accounts for the diffusion occurring due to these collisions. The value of D_{Kn} is dependent on the pore channel diameter, d_{pore}. The dependence on the gas temperature is an order smaller when compared to the bulk diffusion coefficient.

4.3.3.2 Energy transport

The effect of small channels on the energy transfer phenomenon is similar to that on mass transport. Assuming that the Fourier law of heat conduction can still be used in the same form, a modified thermal conductivity of the gas is used to account for the gas presence in constricted channels. The value of the mixture thermal conductivity calculated as described earlier is used as the 'bulk' value κ_{bulk} and the influence of the Knudsen number Kn is included. The reduced gas thermal conductivity computed for the simplest case of gas between two plates separated by a small distance (from kinetic theory of gases) is given by Zhang [101] and Ferkl et al. [102]:

$$k_{gas} = \frac{k_{bulk}}{1 + Kn \cdot \frac{2 - \alpha_T}{\alpha_T} \cdot \frac{9\gamma - 5}{\gamma + 1}} \tag{4.20}$$

where, α_T is the thermal accommodation coefficient, γ is the ratio of specific heats and Kn is the Knudsen number. Knudsen number is a non-dimensional quantity defined as the ratio of the mean free path of the gas molecules to a representative physical length scale of interest (in this case, the diameter of the pore channel). The thermal accommodation coefficient α_T is defined as the ratio of energy differences before after collision of a gas molecule with a wall and hence its value depends on the gas/surface pair. A specular reflection leads to a value of 0 while a diffuse one gives a value of 1. The actual value of α_T lies in this range of 0 to 1 and is to be determined experimentally [103]. Usually this data is however difficult

to measure and it is common practice to use an approximate value for this quantity. In all the calculations presented in this paper, a value of α_T = 0.85 is used. Essentially, modifying the thermal conductivity using the expression above can be interpreted as the inclusion of a temperature jump condition due to the small scale nature of the channels under consideration and hence called the "temperature jump approximation" in the continuum and free regimes. On the other hand, in the transition regime, the expression can be interpreted as a result of the change in the mean free path of the molecules due to their increased collisions with the walls [101].

4.3.3.3 Surface reaction kinetics

The rate equation describing the adsorption and desorption phenomena can be derived from a first-principles based approach and subsequent calibration of parameters or alternately from experimentally obtained rate equations directly. In the following description, the derivation for a generic reaction kinetics equation is presented.

A first-principles derivation will involve combining the molecular rate of impact on the channel walls and a sticking probability based on physical considerations [104]. In the following derivation, let θ be the fraction of adsorption sites covered with the adsorbed molecules.

From kinetic theory, the rate of molecular collisions per unit time per unit area of the channel surface is given by:

$$F = \frac{p}{\sqrt{2\pi m R_u T}} \tag{4.21}$$

where, p is the partial pressure of the adsorbing species and m is the mass of a single molecule. This can be combined with a sticking probability S to give the total rate at which molecules will get adsorbed on the adsorbent surface. The sticking probability is expressed in an Arrhenius form and involves a function of the current surface coverage, $f(\theta)$.

$$S = f(\theta) \cdot \exp\left(-\frac{E_{ads}}{R_u T}\right) \tag{4.22}$$

where, E_{ads} is the activation energy required for adsorption, T is the gas temperature, θ is the surface coverage and $f(\theta)$ is the function defining the dependence of sticking probability on the surface coverage. The value of S represents a probability and hence will always lie in the range $0 \leq S \leq 1$. The above form of S considers its dependence on two factors – the existing coverage of adsorption sites with the adsorbent molecules θ and the existence of any activation energy barriers for the adsorption reaction to occur.

Finally, the rate of adsorption R_{ads}, expressed as rate of change of θ, can be written as a product of the molecular wall impact rate and the sticking probability (Eqs. (4.21) and (4.22)):

$$R_{ads} = F \cdot S \cdot \frac{1}{N_s} = \frac{p}{\sqrt{2\pi m R_u T}} \cdot \frac{1}{N_s} \cdot f(\theta) \cdot \exp\left(-\frac{E_{ads}}{R_u T}\right) \tag{4.23}$$

The additional term N_s represents the number of adsorption sites per unit area.

Once an adsorbent molecule has adsorbed to the surface, it tries to detach itself by means of vibrations. This is a function of the temperature at which the adsorbed molecule exists which is the same as the surface temperature T_s. Including an activation energy barrier for the desorption process as well, the following Arrhenius form for the rate of desorption is obtained:

$$R_{des} = g_1(\theta) \cdot g_2(T) \cdot \exp\left(-\frac{E_{des}}{R_u T_s}\right) \tag{4.24}$$

where, E_{des} is the activation energy for desorption, $g_1(\theta)$ is a surface coverage dependent function describing the probability of encountering an adsorbed molecule and $g_2(T)$ is the probability of a molecule at temperature T detaching from the surface. The function $g_2(T)$ is often termed the pre-

exponential term and can be derived based on kinetic considerations [105] and is usually taken to be of the following form:

$$g_2(T) = \frac{e\chi k_B T}{\mathbb{h}} \cdot \exp\left(\frac{\Delta S}{R_u}\right) \tag{4.25}$$

where, χ is a pre-exponential correction term, k_B is the Boltzmann constant, $\mathbb{h}$ is the Planck's constant and ΔS is the entropy of reaction. The pre-exponential term above represents the frequency of vibration of the adsorbed molecule and is very difficult to measure experimentally. It is common practice to assume a value of 10^{13} Hz for this term (the above expression evaluates to this value if ΔS is assumed to be 0, i.e., for a reversible reaction), which represents the approximate vibration frequency of the adsorbed molecules.

The final form of the rate equation, which gives the rate of change of θ, is a summation of the adsorption and desorption rates:

$$\frac{d\theta}{dt} = R_{ads} - R_{des}$$

$$\frac{d\theta}{dt} = \frac{p}{\sqrt{2\pi m R_u T}} \cdot \frac{1}{N_s} \cdot f(\theta) \cdot \exp\left(-\frac{E_{ads}}{R_u T}\right) - g_1(\theta) \cdot \frac{e\kappa k_B T}{\mathbb{h}} \cdot \exp\left(\frac{\Delta S}{R_u}\right) \cdot \exp\left(-\frac{E_{des}}{R_u T_s}\right) \tag{4.26}$$

The above general expression is now expanded for the specific case of a second-order reaction. An example of such a reaction would be the adsorption of CO_2 molecules onto a surface which has vacant amine sites. In this system, one CO_2 molecule requires the presence of two adjacent free amine sites. The CO_2 molecule eventually gets adsorbed onto one of the amine sites forming a carbamate ion, the other gets used up for the formation of a protonated amine. The following is the reaction mechanism:

$$2R_2NH + CO_2 \leftrightarrow R_2NH_2^+ + R_2NCO_2^- \tag{4.27}$$

For the functions $f(\theta)$ and $g(\theta)$, linear probability models are used. This means that it is assumed that the probability of finding a vacant amine site is equal to the fraction of unoccupied amine sites remaining on the adsorbent surface. If θ is defined the fraction of amine (adsorption) sites covered with CO_2 molecules only, then the fraction of covered sites is 2θ and the fraction of vacant sites is $(1-2\theta)$. Hence, the probability of finding two adjacent vacant sites is given by:

$$f(\theta) = (1-2\theta)^2 \tag{4.28}$$

and the probability of finding a carbamate ion next to a protonated amine site is given by:

$$g(\theta) = \theta^2 \tag{4.29}$$

Substituting the above expressions into Eq. (4.26) and combining terms for the sake of clarity, the following form is obtained:

$$\frac{d\theta}{dt} = K_{ads}(1-2\theta)^2 - K_{des}\theta^2 \tag{4.30}$$

where, K_{ads} and K_{des} corresponding to the adsorption and desorption rate constants given by:

$$\begin{aligned} K_{ads} &= \frac{p}{\sqrt{2\pi m R_u T}} \cdot \frac{1}{N_s} \cdot \exp\left(-\frac{E_{ads}}{R_u T}\right) \\ K_{des} &= \frac{e\kappa k_B T}{\mathbb{h}} \cdot \exp\left(\frac{\Delta S}{R_u}\right) \cdot \exp\left(-\frac{E_{des}}{R_u T_s}\right) \end{aligned} \tag{4.31}$$

4.3.4 Coupling schemes

In the sub-pore system, two types of coupling strategies are to be considered – first, the interaction of the different physical mechanisms that prevail in the sub-pore system and second, the interaction between the macro- and sub-pore systems.

The governing equation for the diffusive system (both mass and energy transport) are modified when solved in the sub-pore system compared to the macro-pore system. An additional source term is

introduced to include the effect of the surface reaction kinetics. This source term accounts for any addition/loss of mass/energy due to the adsorption and desorption processes.

The interaction between the macro- and sub-pore system, in comparison, is much more involved owing to the issues related to conservation (of mass or energy). It is necessary that the amount of flux (mass or energy) into or out of the sub-pore system occurring at the macro-/sub-pore interface is correctly reflected in both the sub-pore and the macro-pore systems. In order to ensure this, a Neumann boundary condition is used at the macro-/sub-pore interface and is to be satisfied in both the macro- and sub-pore systems. On the sub-pore surface and at the farther end of the sub-pore system (smallest channels), a zero gradient boundary condition is used.

4.3.5 Numerical implementation details

The sub-pore geometry consists of channels of varying sizes and it is necessary to formulate the discretized version of the governing equations in a way that the physical conservation laws are always satisfied. In order to accomplish this, a finite volume formulation is used that conserves the mass flux across the cross-sectional surfaces of the 1D cylindrical structures that make up the sub-pore geometry. The implementation details of the numerics within the sub-pore system are discussed here.

Figure 4.2 presents a schematic representation of a single cell within the sub-pore system, shown for the purpose of explaining the nomenclature and general formulation. Within the sub-pore system, the value of the coordinate ξ starts at 0 at the macro-pore/sub-pore interface and increases with increasing levels. For this cell, the total change in the quantity of interest ϕ in the fixed cell volume $\mathbb{V}$ is a result of the net change in the quantity due to fluxes observed at the east and west faces - J_e and J_w, respectively, and any source $\dot{\omega}$ present within the cell. J_e and J_w are both defined to be positive in the direction of increasing ξ. Expressing the fluxes in terms of diffusivity and a gradient across the cell faces, the following expression is obtained:

$$\Delta(\mathbb{V}_i\phi_i) = J_{e_i} - J_{w_i} + \omega_i = A_{e_i}\alpha_{e_i}\left.\frac{\partial\phi}{\partial\xi}\right|_{e_i}\Delta t - A_{w_i}\alpha_{w_i}\left.\frac{\partial\phi}{\partial\xi}\right|_{w_i}\Delta t + \omega_i \tag{4.32}$$

The variable ϕ above represents the variable of interest per unit volume – that is, it will be replaced by ρy_c and $\rho C_p T$ for species and energy diffusion formulations, respectively. This is assuming that the variable values are stored at the cell centroid. The diffusivities and gradients in the above expression are to be computed as average values at the faces. In order to do this, the average cell sizes on west (Δ_w) and east (Δ_e) faces are first calculated:

$$\Delta_{w_i} = \frac{\Delta\xi_{i-1} + \Delta\xi_i}{2}; \Delta_{e_i} = \frac{\Delta\xi_i + \Delta\xi_{i+1}}{2} \tag{4.33}$$

Δ_w and Δ_e can then be used to calculate the values of the gradient and other variables at the west and east faces, respectively. Using a linear interpolation scheme, the following expressions are obtained.

$$\begin{gathered}\alpha_{w_i} = \frac{\alpha_{i-1}\Delta\xi_i + \alpha_i\Delta\xi_{i-1}}{2\Delta_{w_i}}; \alpha_{e_i} = \frac{\alpha_{i+1}\Delta\xi_i + \alpha_i\Delta\xi_{i+1}}{2\Delta_{e_i}} \\ \left.\frac{\partial\phi}{\partial\xi}\right|_{w_i} = \frac{\phi_i - \phi_{i-1}}{\Delta_{w_i}}; \left.\frac{\partial\phi}{\partial\xi}\right|_{e_i} = \frac{\phi_{i-1} - \phi_i}{\Delta_{e_i}}\end{gathered} \tag{4.34}$$

The areas A_w and A_e would correspond to the total amount of areas the cell is interacting with on the east and west directions. The two area values may or may not be equal – four such scenarios may be encountered and will be discussed shortly.

The formulation in Eq. (4.32) above is assembled for the entire hierarchical system within a single sub-pore. Similar formulations will need to be constructed for all the sub-pores existing in the porous medium. A fully implicit treatment is used for the main variables within ϕ – that is, for the mass fraction and temperature values for species and energy diffusion, respectively. The values of the other physical constants such as density, thermal conductivity and specific heat are calculated based on the mass fraction

and temperature values computed at the previous time-step – this means that the computation of these values are always lagging the quantity of interest in getting updated. This is a reasonable assumption given the small time-steps necessary to resolve the physics occurring at these length scales and hence the variation in the properties can be assumed to be insignificant between one time-step to another.

Constructing the matrix for the above mentioned diffusion system and using a fully implicit formulation, a tri-diagonal system of the following form is obtained:

$$\begin{pmatrix} C_{p_0} & C_{e_0} & 0 & & & & \\ C_{w_1} & C_{p_1} & C_{e_1} & \cdots & & 0 & \\ 0 & C_{w_2} & C_{e_2} & & & & \\ & \vdots & & \ddots & & \vdots & \\ & & & & C_{p_{n_i-2}} & C_{e_{n_i-2}} & 0 \\ & 0 & & \cdots & C_{w_{n_i-1}} & C_{p_{n_i-1}} & C_{e_{n_i-1}} \\ & & & & 0 & C_{w_{n_i}} & C_{p_{n_i}} \end{pmatrix} \begin{pmatrix} \phi_0 \\ \phi_1 \\ \phi_2 \\ \vdots \\ \phi_{n_i-2} \\ \phi_{n_i-1} \\ \phi_{n_i} \end{pmatrix} = \begin{pmatrix} R_0 + R_{BC} \\ R_1 \\ R_2 \\ \vdots \\ R_{n_i-2} \\ R_{n_i-1} \\ R_{n_i} + R_{BC} \end{pmatrix} \tag{4.35}$$

In the formulation above, it is seen that the index numbering starts with 0 instead of 1. The index 0 represents the parent macro-pore cell that is included in the solution of the sub-pore system. By including the macro-pore cell also in the sub-pore system, an implicit coupling with the macro-pore system is established which satisfies the conservation laws directly. This avoids any need of explicit checks to ensure conservation and/or use of limiters to do the same.

Three sets of constants are identified – the coefficients corresponding to west (w), current (p) and the east (e) cells. The expressions for these are as follows:

$$C_{p_i} = \rho_i \mathbb{V}_i + \frac{\left(\rho_{w_i}\alpha_{w_i}A_{w_i}\right)}{\Delta_{w_i}}\Delta t + \frac{\left(\rho_{e_i}\alpha_{e_i}A_{e_i}\right)}{\Delta_{e_i}}\Delta t$$

$$C_{w_i} = -\frac{\left(\rho_{w_i}\alpha_{w_i}A_{w_i}\right)}{\Delta_{w_i}}\Delta t \tag{4.36}$$

$$C_{e_i} = -\frac{\left(\rho_{e_i}\alpha_{e_i}A_{e_i}\right)}{\Delta_{e_i}}\Delta t$$

$$R_i = \rho_i \mathbb{V}_i \phi_i^n + \omega_i$$

The term on the RHS R_i is modified by addition of the term R_{BC} to include the desired boundary conditions at the macro-pore cell and the last cell of the sub-pore system. The source term ω_i that is part of R_i is included to establish a coupling with the reaction kinetics that occurs during the time-step in the given cell. Depending on the reaction rates, the total source/sink term for the mass and energy equations are calculated and used in the diffusion equation formulation.

For time integration, a second-order accurate Crank-Nicholson can also be used instead of the first-order accurate Euler method used above. However, owing to the small time-steps that need to be used in these simulations, the effect on time accuracy of the solutions will be insignificant.

Next, the different scenarios arising due to differently sized cells in the sub-pore system are described. To help describe the different formulations, a single sub-pore system present underneath a macro-cell and zoomed-in views of the different cases are shown in Figure 4.3. As shown in Figure 4.3(a), the sub-pore system consists of two levels with two branches present at the base of the first level. The spatial discretization within the cylindrical structures is also shown for the purpose of clarity.

- *Case 1: Same sized (level) cells on either side* – this is the simplest case in which the adjacent cells on both the west and east faces belong to the same level and hence have the same size as the current cell (shown in Figure 4.3(b)). In this case, the areas A_e and A_w will be equal to the cross-

sectional area of the cell itself while the diffusivity and the gradients are calculated as simple averages computed at the face.

$$A_w = A_e = A_i$$

- *Case 2: Larger neighboring cell on the west side* – this scenario is for the first cell of every level within the sub-pore system. The first cell at every level will be smaller than the cell that precedes it – this can be either a cylindrical cell of the previous level or the macro-cell with which the first sub-pore cell is interacting (shown in Figure 4.3(c)). The difference in the cell sizes will affect the calculation of the gradient and the face-averaged values, however, the area of interaction is still equal to the cross-sectional area of the cell itself.

- *Case 3: Smaller neighboring cell at the east face* – the last cell of every level branches into a number of smaller cells which belong to the next level (shown in Figure 4.3(d)). Hence, the east face area A_e will be equal to the sum of areas of all the smaller cells that branch out from the current cell.

$$A_e = n_b A_{i+1}$$

- *Case 4: Macro-pore cell at the west face* – the first cell of every sub-pore has a macro-pore cell at its west face (shown in Figure 4.3(e)). This case is similar to case 3 described above and hence the formulation details are the same.

4.3.6 Assumptions

The proposed sub-pore methodology involves the use of numerous assumptions. These are summarized below since it is important to realize the conditions under which the results of such a methodology are valid and also will assist improvements in the future by overcoming certain limitations of the current model.

1. The porous geometry that exists underneath the surface and comprises of the sub-pore system is made up of a hierarchical network of porous channels.
2. To keep the mathematical models tractable, the porous channels are assumed to be cylindrical in nature allowing the use of governing equations formulated only for one dimension. This significantly reduces the computational expense and also simplifies the system.
3. For the diffusion equations, a Fickian form of governing equation is applicable at all the length scales that are involved. This includes the scales where the Knudsen effects dominate due to the small size of the channels. This allows use of the standard numerical techniques applicable for macro-diffusion and hence the entire range of length scales can be modeled in the same system of equations.
4. The surface kinetics assume that the adsorption is purely a surface phenomenon (no volume filling and/or solid-state diffusion is considered).
5. The surface reaction does not alter the nature of the surface as far as diffusion is concerned and the original sub-pore geometry can be used for entire duration of simulation.

4.4 Sub-pore methodology application

The sub-pore modeling methodology described thus far is now applied to a set of model reaction-diffusion problems. The problems are chosen so as to highlight the different capabilities that the developed framework offers and demonstrate its usefulness in specific scenarios.

A schematic representation of the general problem set-up used is shown in Figure 4.4. All the problems considered are two-dimensional. A particle exhibiting macro-porosity is placed at the center of a square domain. The macro-porosity is accounted for by the immersed boundary method while any unresolved pore channels are accounted for by the sub-pore system. The domain consists of a two-component

gaseous mixture – a secondary species (species A) that is present in relatively dilute concentration and the remaining portion of the mixture is composed of a carrier species (species B). The outer bounds of the domain are set as constant value Dirichlet boundaries for species mass fractions as well as temperature, essentially representing infinite sources of the gaseous mixture of a particular composition, and energy. The particle pore space is initially filled up entirely with the species B while the space outside of the particle is maintained initially at the same concentration level as the domain boundaries. Starting from this initial field, species A is allowed to diffuse into the particle pore (both macro- and sub-) space and subsequently adsorb onto the sub-pore surface.

The properties of species A and B are chosen to be those of carbon-dioxide (CO_2) and nitrogen (N_2), respectively. This is in view of the main application problem considered – CO_2 adsorption in amine-impregnated meso-porous silica particles. This choice of the component properties aids in better understanding of the underlying physics and helps in relating the trends observed in the different simulations to the CO_2 adsorption problem.

In the results presented, the transient profiles of concentration and adsorption levels are plotted and used for the analysis of the related physics. The averaging of the concentration is performed for – (1) all of the macro-pore space, (2) all of sub-pore space, (3) the entire particle pore space (both macro- and sub-pores) and (4) all channels of a particular level in the sub-pore system. The adsorption profiles on the other hand are presented in terms of the amount of surface coverage θ and the averaging is performed for – (1) all the sub-pore surface area for the entire particle and (2) all sub-pore surface area belonging to a particular level in the sub-pore system. Both the concentration and adsorption profiles are expected to asymptote to their respective saturation levels when the simulations are performed for a sufficiently long duration. Since saturation (or attaining steady-state) is of interest, it is necessary to define this term. In all the discussions, a process (mass transport or adsorption) is said to be saturated if the quantity of interest (concentration or surface coverage, respectively) attains a value of 95% of the saturated state.

4.5 Macro-pore/sub-pore interchangeability

The proposed framework is capable of extracting results at the level of individual pore channel sizes and the related physical phenomena occurring in multi-scale reaction-diffusion problems in porous media. Validating the results of this framework however is problematic because no previous experimental or numerical results are available which present data in such detail. In order to overcome this issue, a number of test simulations have been conducted on the developed framework for verification. This includes trivial tests like comparing the numerical solutions with analytical derivations by separating the diffusion and adsorption systems.

In addition to these, a special test problem is created that presents a stringent check regarding the correctness of the physics being modeled in the sub-pore system. Since the IBM framework that is used to model the macro-pores has been validated and applied for a wide variety of cases in the past [95, 96], a test problem is used wherein the macro-pores can be alternately modeled to be part of the sub-pore system, allowing comparison of results obtained from simulations with and without macro-pore modeling.

A square-shaped solid porous medium is placed at the center of the square domain (in the problem set-up described earlier). The solid medium exhibits porosity owing to the existence of pore channels that open up at the outer surface of the medium. Two pore channel sizes exist in the medium – larger channels of diameter 2 microns and smaller channels of diameter 1 microns. The side length of the outer domain is 100 microns while that of the solid medium is 50 microns. Dirichlet boundary conditions used at the domain boundaries correspond to 0.15 mass fraction of species A. The initial field also consists of 0.15 fraction of species A in the region outside of the particle while within the particle pore space, the concentration level of species A is 0. Simulations are performed until the particle pore space gets saturated with species A (i.e., reaches a mass fraction of 0.15).

Two types of simulations are considered depending on the way the pore channels in the solid medium are modeled:

- *With macro-pores* – the larger channels are modeled as macro-pores while the smaller ones are modeled in the sub-pore system that exists underneath the macro-pore surface (see Figure 4.5(a))
- *Without macro-pores* – both the pore channel sizes are modeled in the sub-pore system itself and hence no macro-porosity exists in the medium (see Figure 4.5(b)).

To ensure similarity between the two simulations, the individual porosity contributions by the two channel sizes are maintained to be the same between the two cases.

The transient profiles of species A concentrations averaged over both the channel sizes (that is the full particle pore space) and the individual channel sizes obtained from these simulations are presented in Figure 4.6. In general, the presented comparisons show very good agreement. The largest difference between the two simulations for the full particle profiles is around 5%. This can be attributed to the marked differences existing between the two simulations. For instance, when the larger channel is modeled as a macro-pore, it is solved as a two-dimensional channel rather than as a one-dimensional channel when modeled as part of the sub-pore system. Also, when the larger channels are modeled in the sub-pore system, they are created uniformly on the entire outer surface of the solid, whereas in the macro-pore simulations, there are a finite number of openings into the larger channels. Given these differences, the comparisons are very good. Similar comments can be made about the profiles presented for the individual channel sizes.

4.6 Reaction-diffusion in porous circular particle

Next, a general reaction-diffusion system is considered involving diffusion and adsorption in a porous particle. The particle is assumed to be circular in shape and has a diameter of 100 microns. Other details of the problem set-up remain the same. The square domain, having a side-length of 200 microns, is

discretized using a grid size of 100 cells in each direction – i.e., there are 50 grid points across the particle diameter. The macro-porous particle exhibits a porosity of around 0.40 and a specific surface area of 458 m^2/kg. Channels of size 8 microns or larger are resolved at the macro-pore level. For the sub-pore system, since the PSD to be satisfied is not known, the geometry is created similar to the ad-hoc geometry mentioned earlier. This means that the branching structure is a constant across all level with structures at every level branching into the same number of smaller level structures. The parameters used for this sub-pore geometry are listed in Table 4.1. The contributions of channels of different sizes to the overall volume (PSD) and area of the sub-pores is plotted in Figure 4.7. It is observed that while the smallest channels contribute to less than 1% of the total sub-pore volume, the contribution to sub-pore surface area is more than 10%. At the other end of the spectrum, the largest channels contribute to 60% of the volume but a relatively smaller 30% of the surface area.

Table 4.2 lists the range of values used for different parameters in the simulations. These values are decided based on conditions used in CO_2 adsorption experiments conducted by Lee et al. [106]. The values for activation energies are obtained by comparing the experimental and first-principles based rate equations. A broader range for activation energies is used to ensure that a wider time scale range is obtained for the adsorption process.

The resulting diffusion and adsorption time scales can show a large variation depending on the combination of parameters used. The simulations can hence be classified into three regimes based on the relative time scales of the two processes: (1) adsorption is very fast compared to diffusion (diffusion-limited), (2) adsorption and diffusion time scales are comparable and (3) diffusion is very fast compared to adsorption (adsorption-limited). In the following discussion, simulations performed to determine the time scales of the individual processes by way of pure diffusion and adsorption simulations are presented first. This aids in identifying the base simulation parameters based on which parametric variation studies can be performed later.

4.6.1 Pure diffusion

In order to establish the time scales of the individual physical mechanisms, simulations are performed with the full particle (macro- and sub-pores) but solving only the mass transport governing equations in the sub-pores. This helps determine the amount of time taken for saturation of the entire particle pore space for the selected geometry. The simulation parameters used in this simulation are listed in Table 4.3.

Figure 4.8(a) presents the concentration profiles averaged over the pore space in the macro- and sub-pores of the particle. It is observed that the time to saturation is approximately 85 ms. A zoomed in view of the first 10 ms is presented in Figure 4.8(b) which shows a region of sharp increase during the initial period, followed by a region where the growth rate is much slower. In order to explain this behavior, the concentration profiles averaged on a per-level basis are presented in Figure 4.8(c). To highlight the differences in the concentration levels as the time taken, the plot is presented on a log-log scale. It is observed that the overall saturation behavior of the entire sub-pore space is similar to that of the largest channels (level 1) during the initial period (till around 0.1 ms). This indicates that the saturation is occurring mainly because of the filling up of the macro-pores and the largest channels in the sub-pore system (level 1). The concentration values in other levels are at least at a couple of orders lower in this initial period. Once this initial filling process is complete (after around 0.1 ms), the smaller channels (levels 2, 3, 4 and 5) begin to saturate thus slowing down the overall saturation rate considerably.

4.6.2 Pure adsorption

Simulations are next performed to determine the time scales expected from the adsorption/desorption process. The system parameters used are provided in Table 4.4. For these parameters, the reaction kinetics equation is integrated in time for different combinations of E_{ads} and E_{des}. First, the results obtained for different values of ΔE, defined as $E_{des} - E_{ads}$, are discussed. The value of ΔE is changed by changing the value of E_{des} while maintain E_{ads} at a constant value. The results from simulations performed for

three different values of ΔE are plotted in Figure 4.9. It is observed that a larger value of ΔE leads to a larger surface coverage at saturation, termed hereafter as equilibrium surface coverage. This is a result of the higher activation energy for the desorption process which means that desorption process is much harder to achieve and hence larger amount of adsorption will be observed at equilibrium. Also, the time to saturation increases with increasing ΔE showing an increase of around an order between ΔE = 5 kJ/mol and 15 kJ/mol cases.

Another possible parametric variation is to keep the value of ΔE a constant but modifying the values of E_{ads} and E_{des}. Results obtained for three such combinations are plotted in Figure 4.10. In contrast to the varying ΔE simulations, the equilibrium coverage is observed to remain a constant due to the constant value of ΔE in the current simulations. The time taken to attain the equilibrium value however does show a strong dependence on the values of E_{ads} and E_{des}. It is observed that the jump in saturation time is around two orders between each simulation (a change of 10 kJ/mol in both E_{ads} and E_{des} values).

It can be concluded from these two sets of simulations that an increase in the value of ΔE results in an increase in both the equilibrium surface coverage and time to saturation while increasing the activation energies and keeping the ΔE a constant results in increase in time to saturation only.

All the cases discussed so far exhibit an adsorption time scale of less than 1 ms whereas as seen earlier, the mass transport is expected to take around 85 ms for saturation. Hence, these simulations are part of the first of the three time-scale based regimes described earlier, i.e., adsorption being – (1) very fast, (2) comparable and (3) very slow – compared to diffusion. Three combinations of E_{ads} and E_{des}, obtained using the general trends observed in the earlier simulations, are hence used so as to obtain adsorption time scales falling under the three regimes mentioned above. These are listed in Table 4.5 along with the adsorption time scales observed in the pure adsorption simulations. The adsorption profiles obtained are presented in Figure 4.11. It is observed that the time scales between the different cases shows orders of

magnitude difference with the case B exhibiting a saturation time comparable to that of diffusion process (around 60 ms).

4.6.3 Canonical cases

The pure diffusion and adsorption simulations described thus far provided adequate information regarding the individual time scales for the mass transport and surface reaction processes. The three cases provided in Table 4.5 present adsorption equation parameters for the three simulations, one each of which lies in the three regimes. The other simulation parameters are the same as for pure diffusion simulations presented in Table 4.3. In this section, simulations performed with all the three physical mechanisms – mass and energy transport, and surface adsorption – acting in the sub-pore system are discussed. These simulations aid in determining the utility of the developed framework for problems falling under the different regimes.

The concentration profiles obtained for the three simulations along with the result from the pure diffusion simulation is presented in Figure 4.12(a). The abscissa is plotted on a log scale to allow a better comparison of the initial transient. Cases A and B show very different characteristics compared to the pure diffusion case. Compared to pure diffusion, the concentration profiles grow at a much slower rate after the initial 0.1 ms. The two cases themselves start showing differences in the growth rate after around 5 ms. Hence, the effect of the adsorption process on the mass transport is significant when the adsorption time scale is much smaller or comparable to the diffusion time scale (cases A or B, respectively). On the other hand, the concentration profile for case C shows a very close match with the pure diffusion case throughout the simulation time indicating that the mass transport is independent of the adsorption in this regime.

In Figure 4.12(b), the adsorption profiles for the three cases are plotted along with the corresponding pure adsorption cases for comparison. Similar to the observations made earlier, the cases A and B show

significant differences between the pure adsorption simulations while case C compares very well. The differences in the initial period (first 50 ms) is attributed to the lesser concentration of adsorbate molecules in the sub-pore space compared to the pure adsorption simulation (where the concentration is fixed at 0.15).

It is clear that accounting for all the physical mechanisms in the sub-pore system has significant effect on the results for the cases where the adsorption time scale is comparable (case A) to or much smaller than the diffusion time scale (case A - diffusion-limited) whereas relatively insignificant impact on cases where the diffusion is much faster than adsorption (case C – adsorption-limited). In fact, for case C the concentration level can be assumed to be at the steady state level and the pure adsorption simulations can be used instead to obtain adsorption profiles.

4.6.4 CO_2 adsorption in amine-impregnated meso-porous silica

For the specific problem of modeling CO_2 adsorption using amine-impregnated meso-porous silica, pure diffusion and adsorption calculations are now performed to determine the time scales governing these processes. The simulation parameters used thus far are already chosen to closely reflect the CO_2 adsorption case (see Table 4.3) and hence the same values are used for these calculations as well. For the reaction kinetics, a rate equation formulated by Lee et al. [106] based on experimental measurements for CO_2 adsorption on amine-impregnated silica particles is used.

4.6.4.1 Estimating diffusion time scale

The meso-porous silica particles used for CO_2 adsorption are known to contain channels going down all the way to around 30 nm (after filling up with the amine polymers). A characteristic of these particles is the enormous area contained in the smaller channels. The sub-pore geometry for this problem should reflect this contribution of the smaller channels. It is hence desirable that the sub-pore geometry used for this problem exhibits these properties.

The parameters used for the sub-pore geometry in the earlier calculations (listed in Table 4.1) increased the specific surface area from 458 m^2/kg to 10000 m^2/kg. While this is acceptable for the CO_2 adsorption problem, the contribution of the smaller channels to the overall surface area is not as large as in meso-porous silica. Hence, in the following calculations, same geometry parameters are used except that the number of branches at every level, n_b, is increased from 5 to 10. The resulting contributions to the area and volume of the porous medium are plotted in Figure 4.13 along with a comparison with the earlier geometry. It is observed that with $n_b = 5$, the surface area is mainly due to the smaller channels while the pore volume is accounted for by the larger channels.

To establish the effect of the different branching structure on the mass transport process, pure diffusion simulations are performed with the new sub-pore geometry. Figure 4.14 shows the concentration profiles averaged over the macro-pore, sub-pore and the entire particle pore spaces for the initial 300 ms of simulation time. It is observed that the diffusion process for this geometry is much slower compared to the $n_b = 5$ simulations. The corresponding plot for the old sub-pore geometry was provided in Figure 4.8(b), in which profiles for the initial 10 ms were plotted. Comparing the two plots, the exact values of the concentration after the initial rapid growth and the growth rate observed afterwards are very different. However, the general trends observed in the earlier simulations are repeated – a rapid initial growth region followed by a prolonged period of slow growth. The slower growth rate is a result of the distribution of channel sizes in the current geometry. Since the contribution to the volume by the smallest channels is negligible in the original geometry, the overall CO_2 saturation level does not depend on the filling up of the smallest pores. On the other hand, in the current simulation the contribution of the smallest channels is nearly 10% and hence their saturation affects the overall saturation level in a substantial way. Since the smallest channels are the slowest to saturate, the growth rate is slower for the current simulation.

The slow nature of growth for the current simulation necessitates the use of extrapolation to get an estimate of the diffusion time scale for the new geometry. The trends observed in the pure diffusion simulations performed earlier, which have been run till the particle pore space is saturated, can be used in the extrapolation strategy for the current simulation. If the slopes of the concentration profiles are assumed to be constant after the initial rapid growth, a linear extrapolation can be used to obtain an estimate the time to saturation. This operation can be performed on any of the profiles available – macro-pore space only, sub-pore space only or the entire particle (macro- + sub-) pore space. The value so obtained can then be compared to the actual saturation time observed in the simulations.

This exercise is performed for both the calculations (i.e., $n_b = 5$ and $n_b = 10$) and the results are presented in Table 4.6. Times calculated based on all the three available concentration profiles are shown and it is seen that all of these values are roughly in the same time range. From the $n_b = 5$ case, the actual times to saturation are observed to be around 4 times larger than the extrapolated values, the reason for which is the asymptotic nature of the profile as the saturation levels are approached. A similar behavior is expected for the $n_b = 10$ simulation as well. Hence, even if a conservative estimate is used, the time scale for diffusion for the new geometry is expected to be in excess of 20000 ms.

4.6.4.2 Estimating adsorption time scale

Next, pure adsorption calculations are performed by solving the rate equation proposed by Lee et al. [106] based on experimental measurements of CO_2 adsorption on amine-impregnated meso-porous silica. The overall form of the experimental rate equation is very similar to kinetics equation derived based on first-principles that was discussed earlier. The simulations are performed at the steady-state conditions of the pure diffusion calculations – i.e., the ambient pressure and temperature are 101.3 kPa and 300K, respectively, and the mass fraction of CO_2 is maintained at 0.15. The adsorption profile obtained by solving the rate equation is plotted in Figure 4.15 in terms of the surface coverage with CO_2 molecules.

The equilibrium surface coverage is observed to be 0.083 and the time taken to reach 95% of this value (i.e., 0.079) is approximately 175 ms.

Hence, for the CO_2 adsorption on amine-impregnated meso-porous silica, it is concluded that the diffusion time scale is indeed very large compared to the adsorption time scale and hence the system falls under the diffusion-limited regime.

4.6.5 Base simulation – Diffusion-limited case

Having identified the regimes where the inclusion of sub-pore system is particularly necessary, the focus is now shifted to the diffusion-limited regime in which the CO_2 adsorption problem is expected to fall under. The case A simulation discussed earlier which falls in this regime is chosen to be the base simulation of interest and will be used for other parametric studies later on. In this section, results obtained for case A (termed 'base simulation' hereafter) will be discussed in greater detail.

In Figure 4.16(a), the transient concentration profiles for the entire particle, averaged over macro-pore space, sub-pore space and the entire pore (macro- and sub-) space of the particle for the entire simulation time. It can be observed that initially (around 50 ms), the sub-pore space lags the macro-pore space in the saturation levels owing to the fact that the sub-pore system feeds on the macro-pore space for transport of mass. However, after this initial period the macro- and sub-pore spaces show very close concentration levels. In Figure 4.16(b), transient profile of total surface coverage of the sub-pore surface with adsorbate (species A) molecules for the entire simulation time is presented. The behavior is observed to be similar to the concentration profiles discussed earlier – a sharp initial growth region followed by a prolonged region of slower adsorption. The value of surface coverage at steady state is observed to be around 0.022 (or 2.2%).

To explore the initial transient behavior further, the concentration and adsorption profiles obtained for the first 50 ms are plotted in Figure 4.17(a) and Figure 4.17(b), respectively. Here, it can be observed that

there are two different growth rate regions – the initial 0.1 ms, showing a steep growth and after 5 ms, showing a relatively smaller growth rate (which is also clearly noticeable in Figure 4.16(a, b)). This change in growth rate is a result of the coupling between adsorption and diffusion processes. During the initial 0.1 ms, since the initial mass fraction of species A is 0 in the particle pore space, the filling up of pore space is rapid. As the concentration level increases, the adsorption rate increases consequently exhibiting a strong coupling which dictates the overall growth rate of both concentration and adsorption levels. This second upward slope continues until the entire particle pore space is saturated with the same concentration levels as the ambient conditions. Another peculiar feature in these profiles is the near zero-growth period which intersperses the two growth rate regions. Explaining this phenomenon requires analyzing the effects of individual physical mechanisms on the system behavior which will be done in a later section.

To understand the behavior of both the diffusion and adsorption processes in relation to channels of different sizes, the results are now presented by performing the averaging for every level of the sub-pore system. As mentioned earlier, level 1 represents the largest channel (4 microns) and level 5 represents the smallest channel (100 nm). Concentration and adsorption profiles presented in Figure 4.18 for the base simulation show the relative times to saturation for channels of different sizes. It is observed that the largest levels are the fastest to attain saturation due to their direct interaction with the macro-pores. On the other hand, the smaller channels show the slowest growth in concentration values owing to two factors. Firstly, Knudsen effects result in slower diffusion rates in the smaller channels. Secondly, the interaction of the smaller channels is only with channels that are of comparable size, which all are still at relatively low concentrations. Hence, saturation of the larger channels acts as a precursor to the saturation process of the smaller channels. With respect to adsorption, again the larger channels show the fastest rate of adsorption due to the higher partial pressures of species A in these pores while the smallest channels are the slowest.

A zoomed in view of the initial transient profiles of concentration and adsorption are presented in Figure 4.19. Due to the larger differences in the concentration values and large initial gradients, the plot is presented on a log-log scale. This plot helps emphasize the process of filling up of the larger channels earlier than the smaller ones and the eventual saturation of the smaller levels to reach the same concentration values as the larger channels.

4.6.6 Effect of sub-pore model

The next set of results presented is from simulations performed to establish the effect of introduction of the sub-pore model on the current problem. Four simulations are used which are variations of the base simulation, i.e., all the simulation parameters are the same as the base simulation, except for the exclusion of certain physical mechanisms as described here:

- *Case 1*: Without the sub-pore model – the sub-pore model is turned off completely and hence the transport of species in the particle is computed in the macro-pores only
- *Case 2*: Sub-pore model with mass transport only – the sub-pore model is included, but only mass transport equations are solved for within the sub-pore system thus allowing diffusion of mass into both the macro- and sub-pores
- *Case 3*: Sub-pore model with mass diffusion and surface adsorption – the sub-pore model is included, but only the mass transport and reaction kinetics equations are solved for within the sub-pore system thus allowing species diffusion and subsequent adsorption in the sub-pores
- *Case 4*: Include the entire sub-pore model – the sub-pore model is included and all the physical mechanisms are solved for in the sub-pore system i.e., mass and energy diffusion with adsorption on the sub-pore surface.

In Figure 4.20(a), the concentration levels of species A averaged over the entire particle pore space is plotted. It is observed that case 1 shows the fastest saturation, taking less than 2 ms while the rest of cases are at least a couple of orders slower. The introduction of sub-pore system (cases 2, 3 and 4) hence affects the mass transport process substantially. A zoomed-in view of the initial 50 ms of simulation time is presented in Figure 4.20(b). Due to the large differences in the time scales, the abscissa is plotted on a log scale. Introducing the sub-pore system affects the concentration growth rate noticeably around 0.1 ms. The explanation for the presence of two different growth rates and the intermediate near-zero growth period is already provided earlier. Including solution to energy diffusion within the sub-pore system (case 4) is observed to help make the saturation quicker. This is because of the additional heat release due to the surface reaction increases the pore space temperature. The higher temperature results in both faster diffusion and adsorption quickening the overall saturation.

To analyze the effect of including the solution to energy equation in the sub-pore system on the adsorption process (i.e., heat generation process due to the surface reaction), adsorption profiles obtained from cases 3 and 4 are presented in Figure 4.21. Overall, the surface coverage shows a lower value for case 4 throughout the simulation time owing to the higher temperature in the particle pore space which results in lower surface coverage. Also, case 4 shows a drop in the surface coverage after the initial rapid growth period. This is again a result of the higher pore space temperature. As explained earlier, the initial rapid growth period is followed by a near-zero growth period both in the concentration and adsorption profiles. Inclusion of heat of reaction and solution to energy equation however increases the temperature which decreases the local equilibrium surface coverage value resulting in lowering of the surface coverage. Once the concentration level again increases, the surface coverage also shows a similar trend.

4.6.7 Parametric studies

Having established the established the relative impact of different physical mechanisms on the overall system behavior, the focus is now shifted to simulations performed to assess the effect of variation of certain parameters. For all the simulations presented in these, one of the parameters is varied and comparisons are made to the base simulations. As for the base simulation, all the three physical mechanisms are included for all the calculations.

4.6.7.1 Effect of changing activation energies

The effect of changing the activation energies is assessed by comparing a set of simulations performed by maintaining a constant E_{ads} while modifying the E_{des} value so that the value of $\Delta E = E_{des} - E_{ads}$ changes. The values used for activation energies are chosen so that the simulations are still in the diffusion-limited regime.

Simulations for three different values of ΔE are considered for this study – 5, 10 and 15 kJ/mol. The ΔE = 5 kJ/mol case corresponds to the base simulation explained in detail earlier. In Figure 4.22, the concentration and adsorption profiles obtained for the three simulations are presented. The species A concentration levels show fastest saturation for the smallest ΔE, i.e., the base simulation. The saturation trend exhibited by the adsorption profiles is similar to the mass transport process and as expected, the equilibrium value of surface coverage is observed to be higher for larger value of ΔE. Also, the increase in ΔE results in a larger dip in the adsorption profile during the initial period of the simulation. This is an result of the larger temperature values because of larger amounts of adsorption for higher values of ΔE.

4.6.7.2 Effect of ambient temperature

The ambient temperature is part of both the diffusion and reaction system. In mass and energy transport equations, the ambient temperature affects the values of mass diffusion coefficient and the thermal conductivity. In the reaction kinetics equation, temperature exhibits a very strong dependence through the

Arrhenius terms in both the adsorption and desorption rates. Additionally, the desorption rate coefficient varies directly as the temperature while the adsorption rate coefficient shows an inverse dependence on the square root of temperature (see Eq. (4.31)). Thus, an increase in temperature is expected to increase the desorption rate coefficient and decrease the adsorption rate coefficient. The effect of temperature on these coefficients is however much smaller than the effect on the exponential (Arrhenius) terms.

Simulations are performed for three values of ambient temperature – 300 (base simulation), 350 and 400 K. In Figure 4.23, results obtained for the three simulations are plotted. It is observed that the increase in temperature decreases the times to saturation for both the mass transport and adsorption profiles. This is a consequence of the higher diffusion coefficient values and desorption rates. Also, the increased desorption rate and decreased adsorption rate reduces the equilibrium surface coverage.

4.6.7.3 Effect of ambient pressure

The final parametric study considered is the variation of the ambient pressure. The ambient pressure in comparison to temperature has a much smaller effect, especially on the diffusion equation. The reaction system though shows a much stronger dependence – the adsorption rate varies as the partial pressure of the adsorbent species and hence as the ambient pressure. Three values of ambient pressure are considered – 50, 101.3 (base simulation) and 200 kPa. The corresponding concentration and adsorption profiles obtained are shown in Figure 4.24. A lower value of partial pressure is expected to result in a lower value of equilibrium surface coverage as well as faster time to attain this value. Consequently, the concentration levels in the particle space attain saturation faster as seen in Figure 4.24(a). Another feature observed is that the initial rapid growth period results in higher values of both concentration and adsorption levels owing to the larger partial pressures of species A. The time to saturation for the 50 kPa case is however smaller, which eventually results in the concentration levels in the pore space saturating earlier than at higher pressures.

4.7 Summary and conclusions

In the current chapter, a new methodology for solving multi-scale, reaction-diffusion problems in porous media is described. In order to account for the multitude of length scales present in typical porous media, the framework approaches the multi-scale nature of the problem by a dual modeling strategy based on the pore sizes. The larger pores, termed the macro-pores, are resolved directly using the traditional numerical techniques while the smaller unresolved pores are modeled using a novel "sub-pore" methodology the details of which form the main subject of the chapter.

The sub-pore system is composed of a network of pores that is constructed underneath the entire macro-pore solid surface within which the relevant physical phenomena are modeled. A hierarchical structure is assumed with the larger pores branching into smaller ones and so on. Such a definition allows tailoring the sub-pore system to satisfy desired geometrical characteristics such as pore size distribution and specific surface area. In the sub-pore system, three physical mechanisms are accounted for – transport of mass and energy, and the surface adsorption. Numerical implementation is simplified by using cylindrical pore structures in the sub-pore system so as to allow one-dimensional assumption. Governing equations are formulated for the diffusion and reaction systems separately and solved in using a finite volume approach. A combination of boundary condition setting is used to strongly couple the macro- and sub-pore system to ensure conservation laws are satisfied. The effects of surface adsorption are included in the mass and energy diffusion equations using source terms.

Numerous carefully designed test simulations are performed both to verify the correctness of the proposed methodology and to highlight different aspects of this framework to problems of practical interest. It is demonstrated that the sub-pore methodology accurately captures the physics relevant at the scales composing the sub-pore system and in fact, can be used to represent pore channels of all sizes existing in the medium. This implies that the sub-pore methodology can be used to simulate the entire pore channel network existing underneath porous media thus rendering the proposed framework a very powerful tool

which is applicable to a much wider range of applications. The various examples discussed help showcase the powerful nature of the developed framework and consequently establish the utility of such a framework for general reaction-diffusion problems involving porous media.

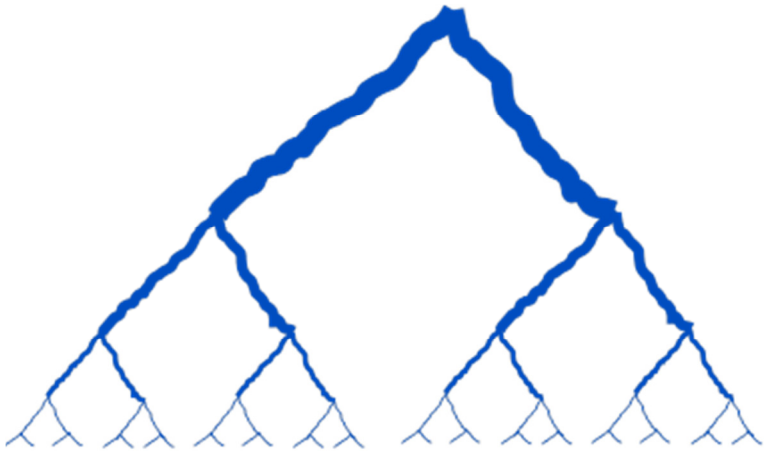

(a)

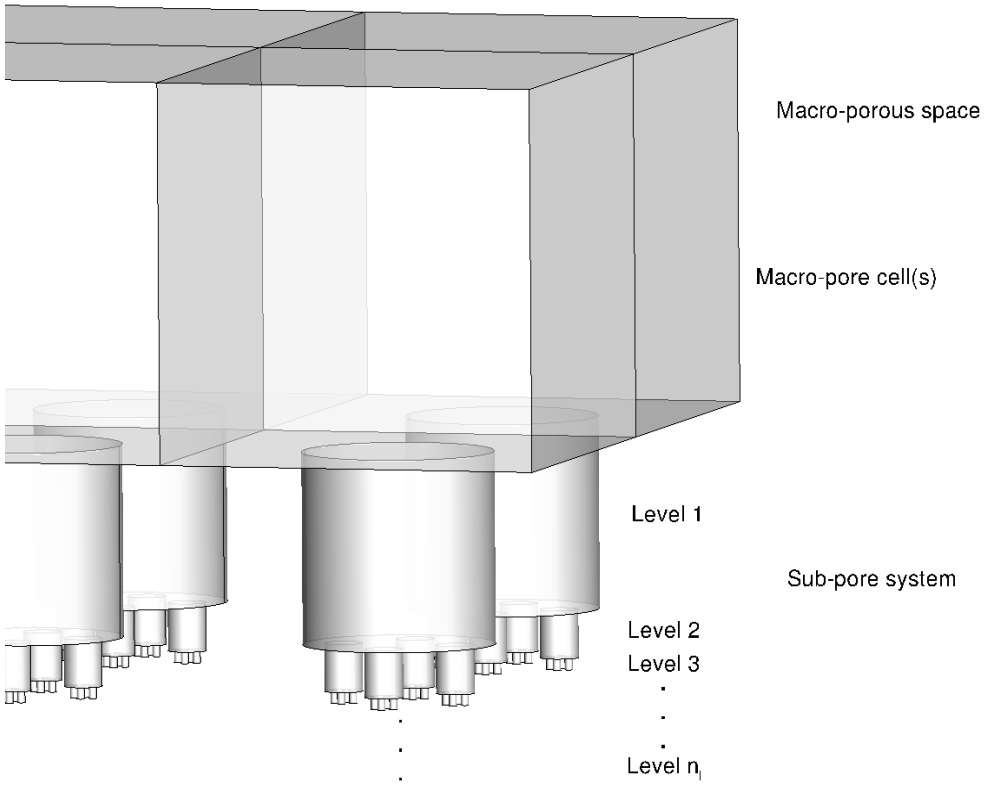

(b)

Figure 4.1 A representation of the (a) pore branching structure and (b) hierarchical system composed of cylindrical structures used in the sub-pore system

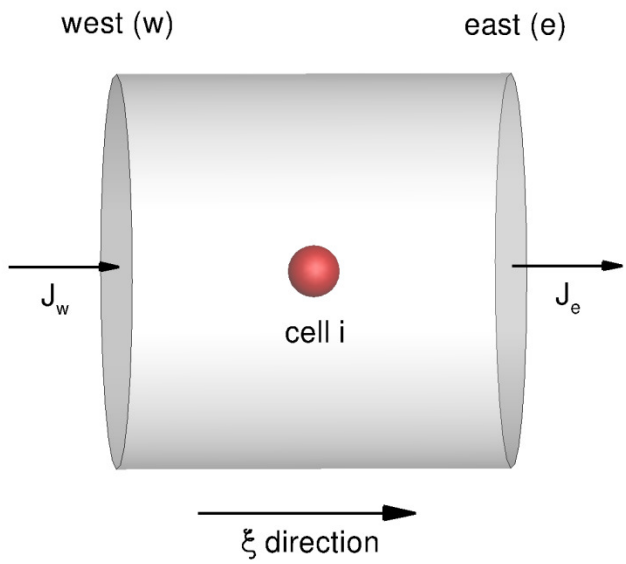

Figure 4.2 A single cell representation within the sub-pore system

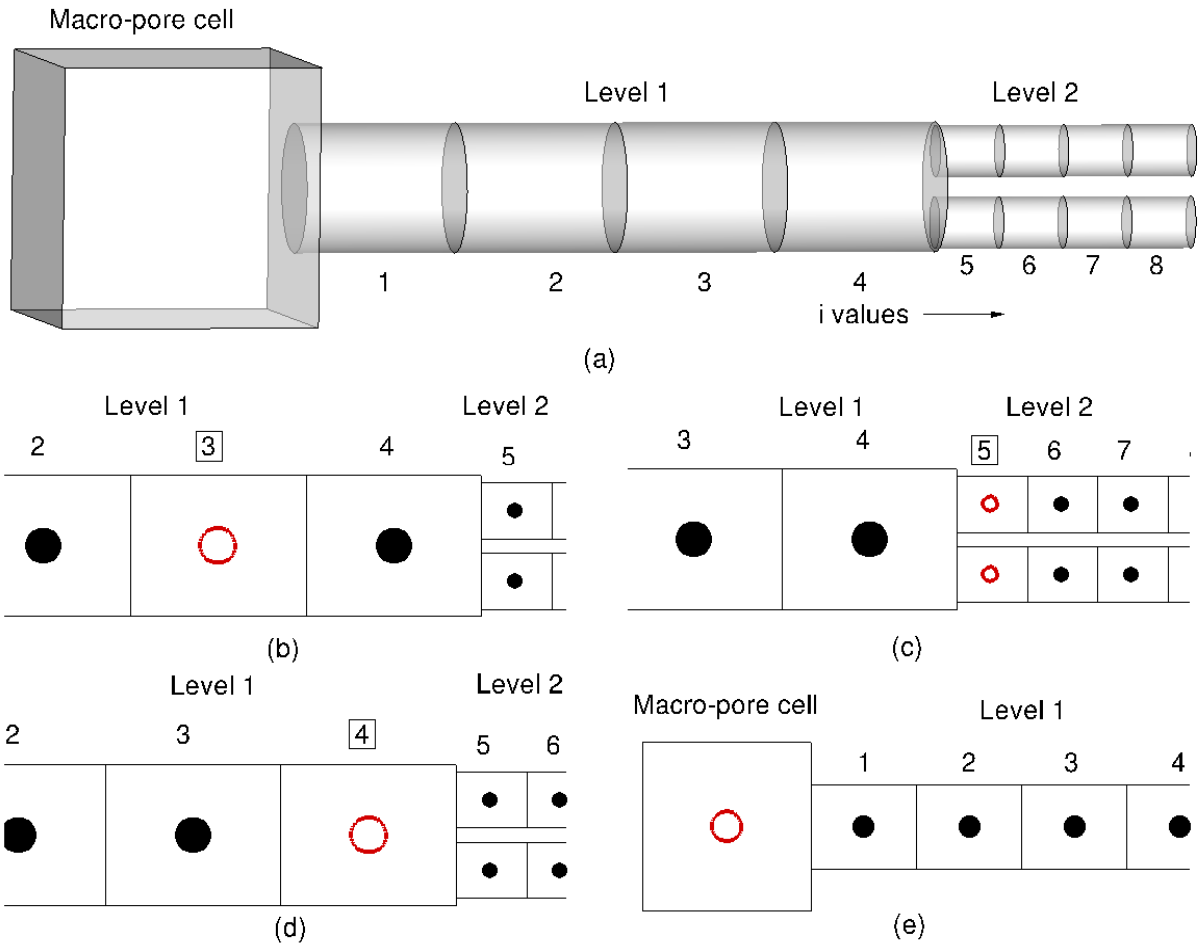

Figure 4.3 A schematic representing the cells within the sub-pore system and the interaction with the macro-pore system

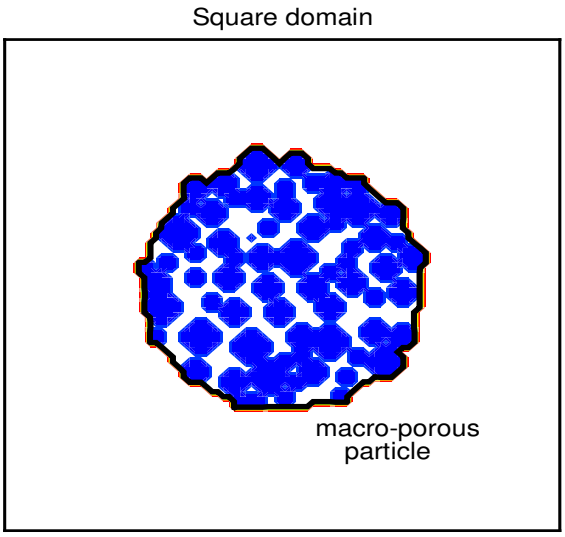

Figure 4.4 A representative sketch of the problem set-up used in all the calculations. The colored region represents the solid volume. The particle shape is only representative – in the presented calculations, both circular and square shaped particles have been used)

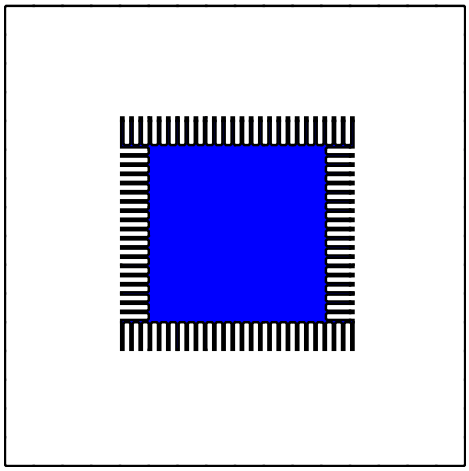

(a)

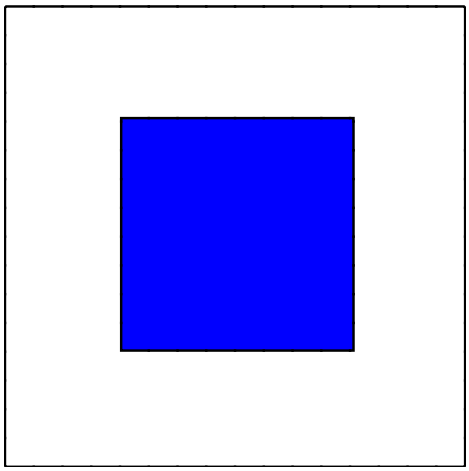

(b)

Figure 4.5 The macro-pore geometries used for simulation (a) with macro-pores – the larger channels being modeled as macro-pores and (b) without macro-pores – both the channel sizes are modeled in the sub-pore system

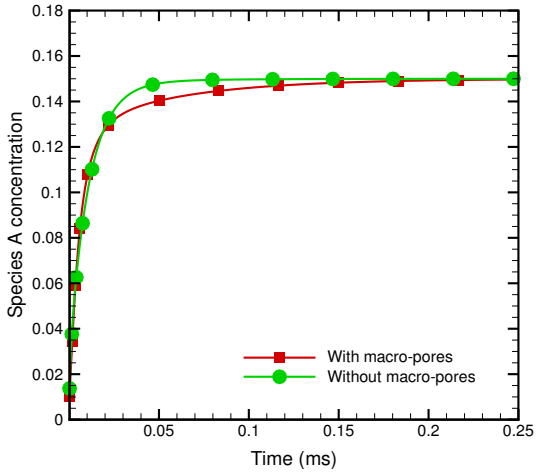

(a)

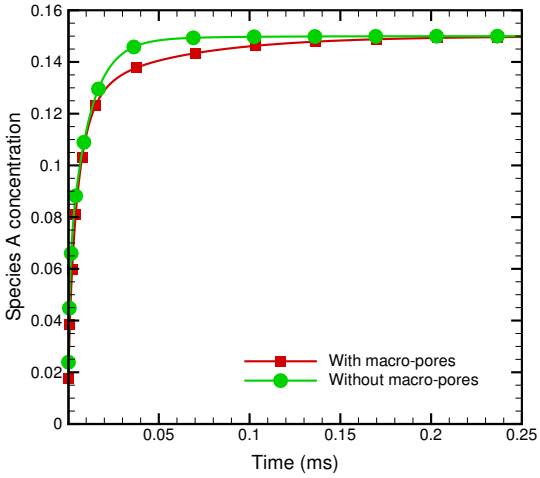

(b)

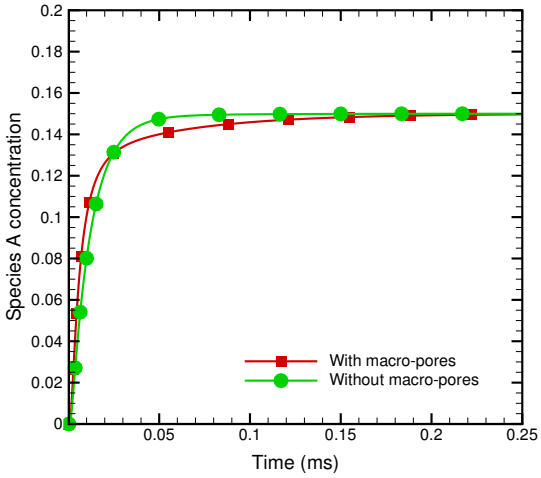

(c)

Figure 4.6 Concentration profiles obtained for (a) the entire particle pore space, (b) all the larger channels (2 microns) and (b) all the smaller channels (1 micron)

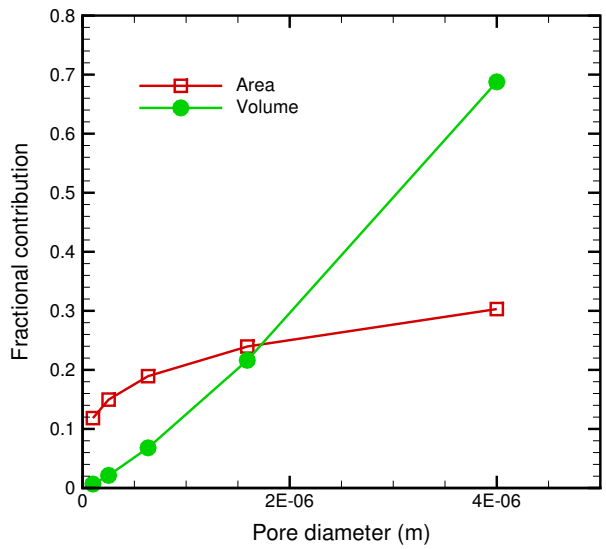

Figure 4.7 Contributions of channels of different sizes to the overall volume and area of the sub-pore geometry

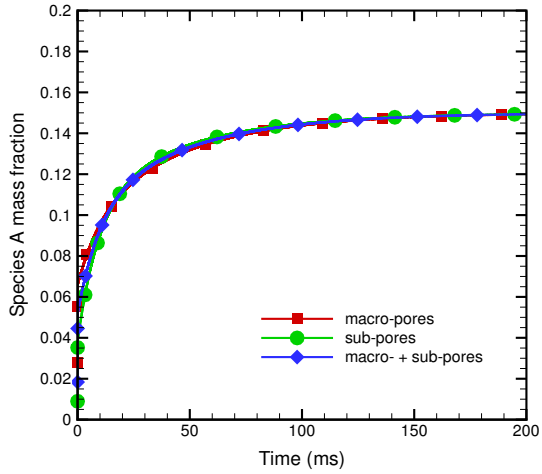

(a)

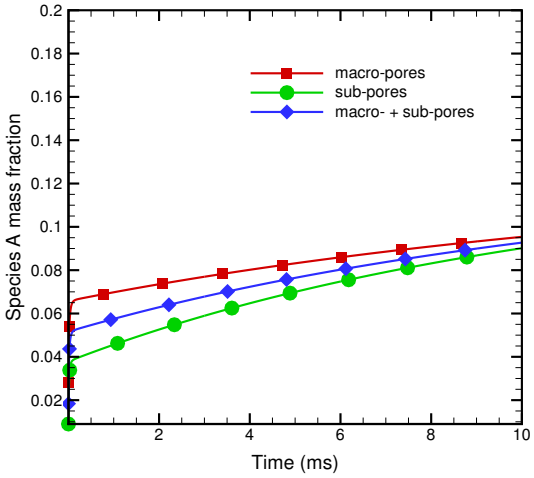

(b)

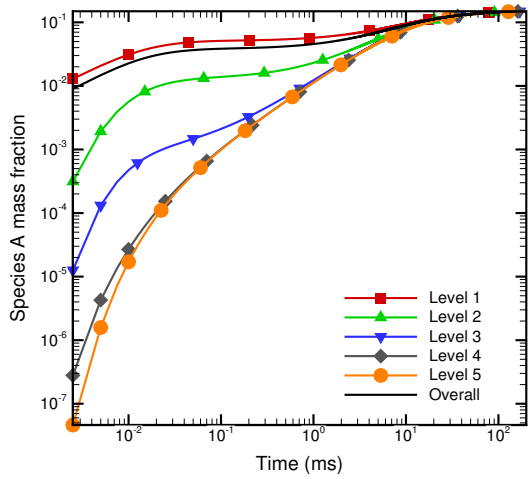

(c)

Figure 4.8 Concentration profiles obtained from the pure diffusion simulation plotted for (a) the full simulation time (b) the first 10 ms and (c) the full simulation time, averaged on a per-level basis

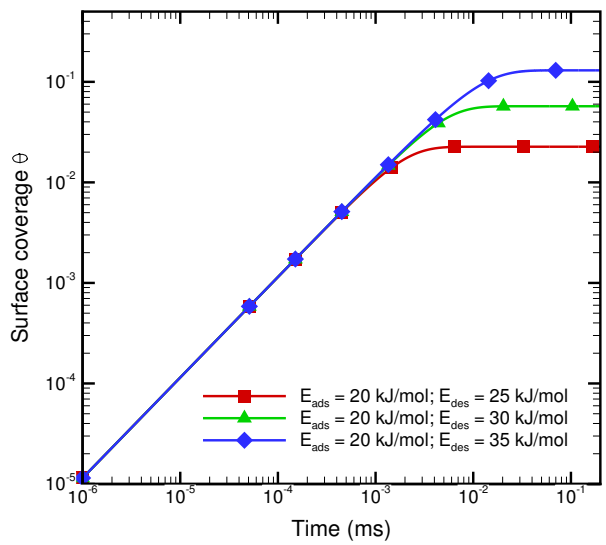

Figure 4.9 Adsorption profiles obtained for three different value of E_{des} while keeping E_{ads} constant in pure adsorption calculations

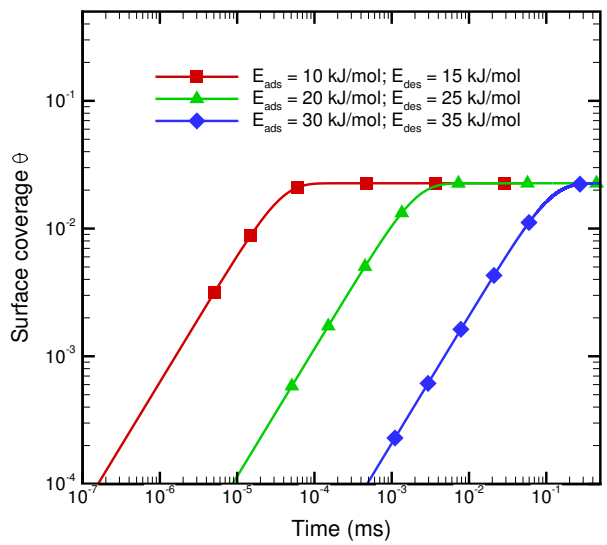

Figure 4.10 Adsorption profiles obtained for different values of E_{ads} and E_{des} while keeping the ΔE constant

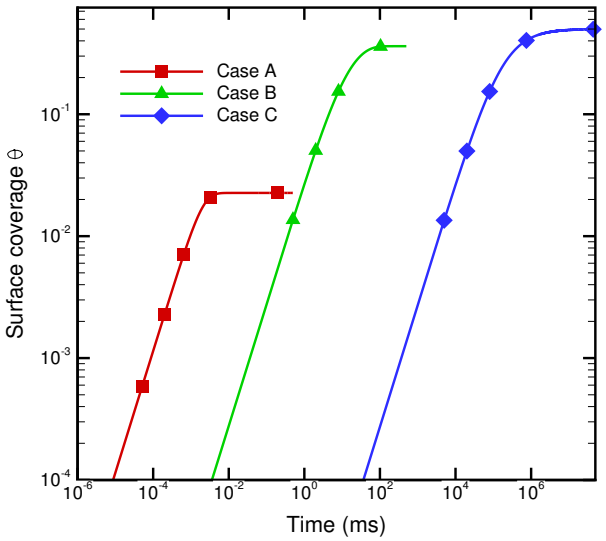

Figure 4.11 Adsorption profiles obtained from pure adsorption calculations for simulations in the three different regimes

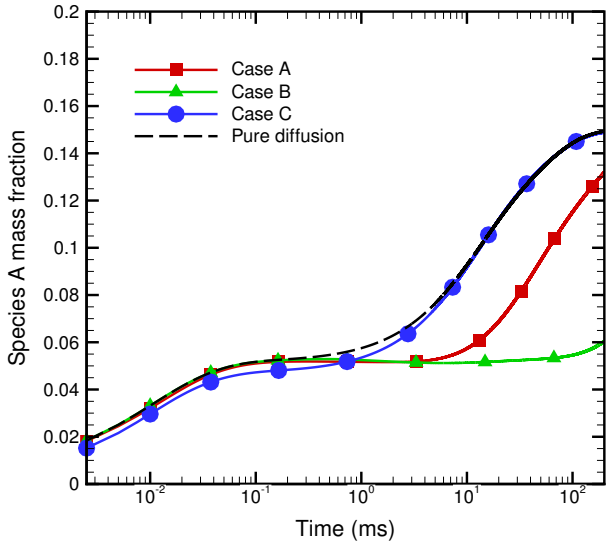

(a)

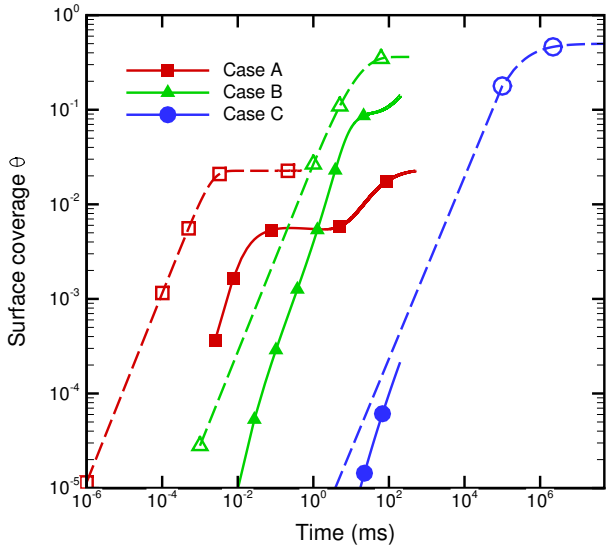

(b)

Figure 4.12 Comparison of transient profiles for (a) concentration and (b) adsorption for the three canonical cases (in (b), the dashed lines with hollow symbols are from the corresponding pure adsorption simulations presented earlier)

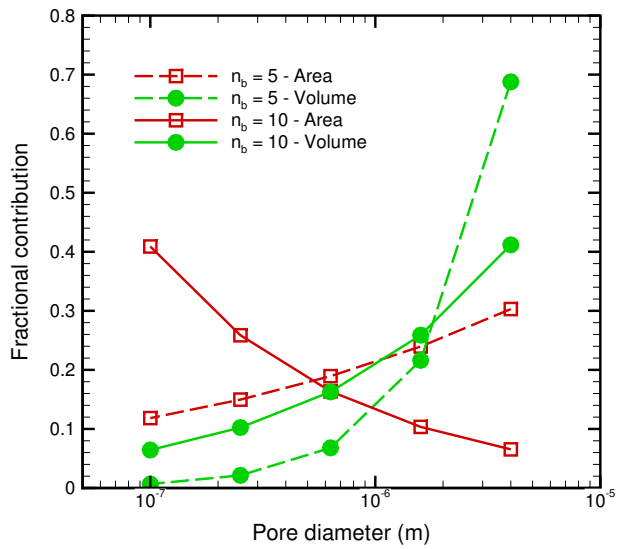

Figure 4.13 Area and volume contributions of a sub-pore geometry with n_b = 10, compared to the geometry used in earlier calculations with n_b = 5

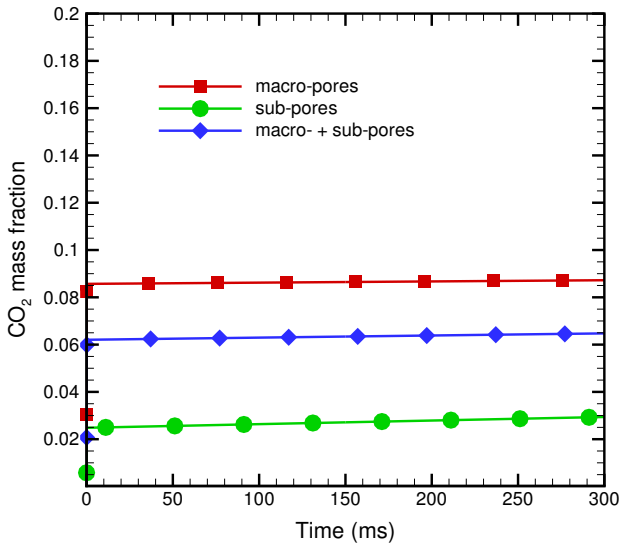

Figure 4.14 Averaged concentration levels in different regions of the particle pore space for the first 300 ms of simulation time

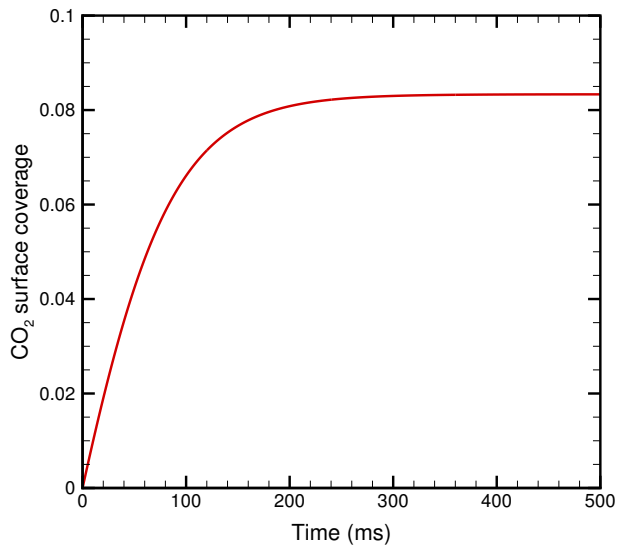

Figure 4.15 CO_2 adsorption profile obtained for pure adsorption calculation using the experimental rate equation proposed by Lee et al. [106]

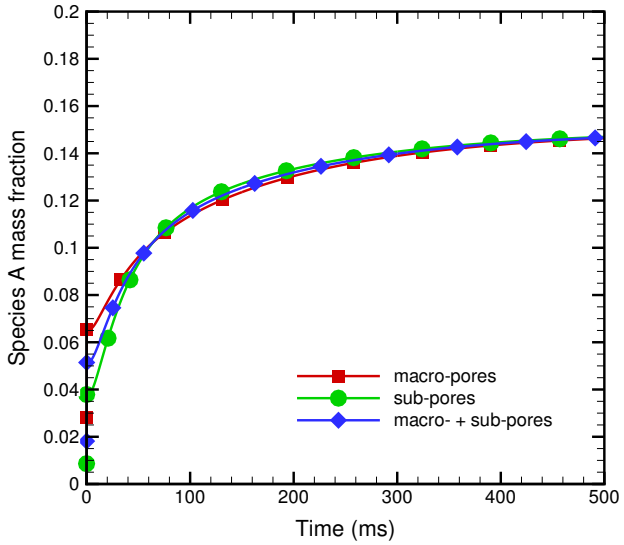

(a)

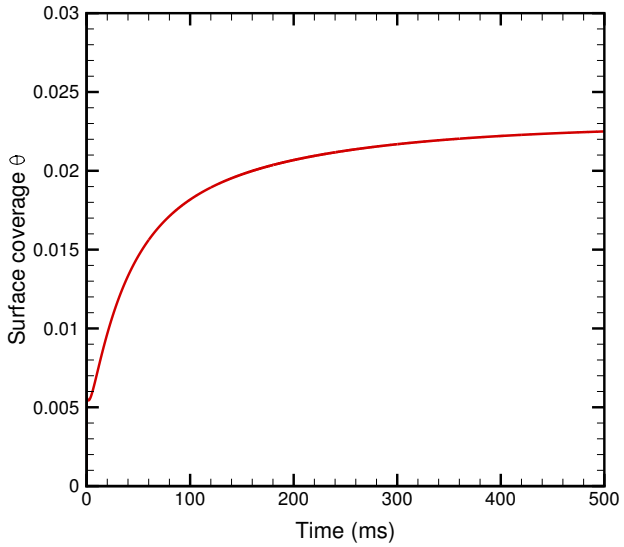

(b)

Figure 4.16 Transient profiles of (a) concentration and (b) adsorption obtained for the base simulation for full simulation time

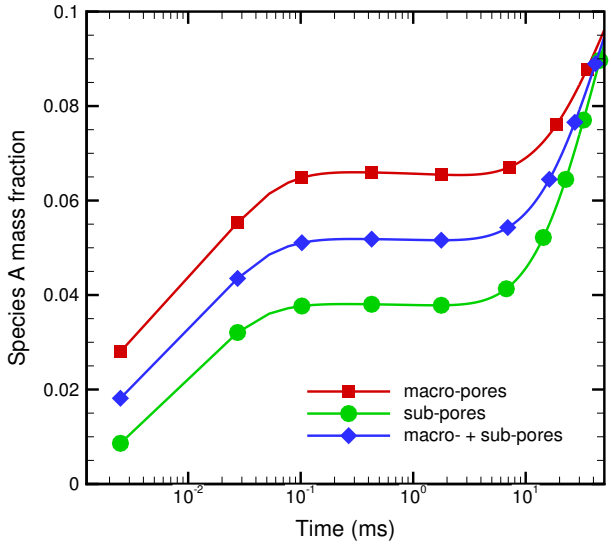

(a)

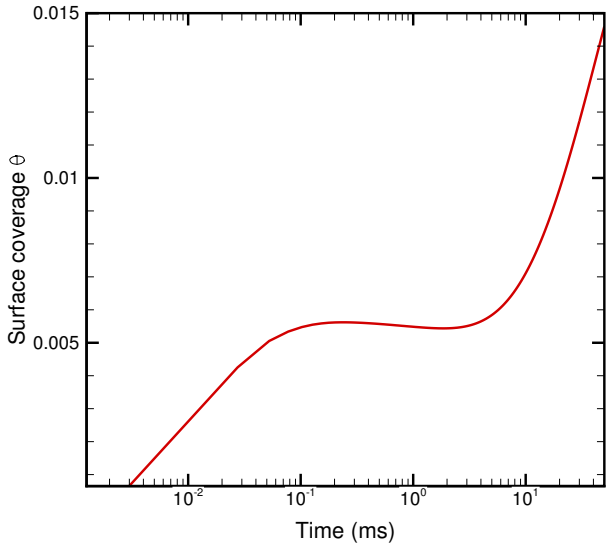

(b)

Figure 4.17 Transient profiles of (a) concentration and (b) adsorption plotted for the initial 50 ms for the base simulation

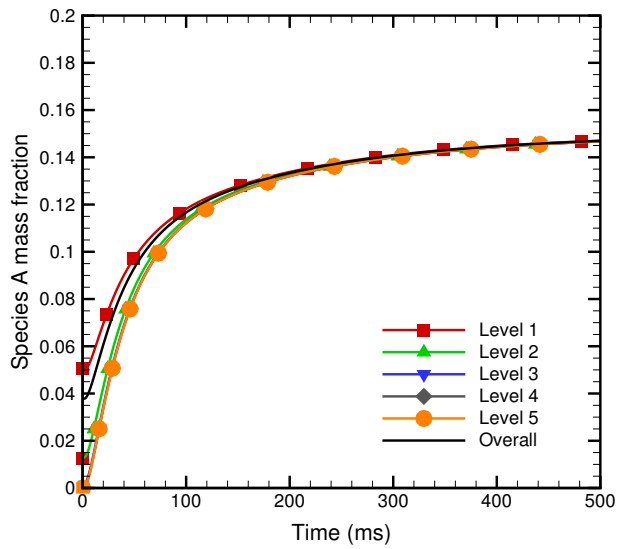

(a)

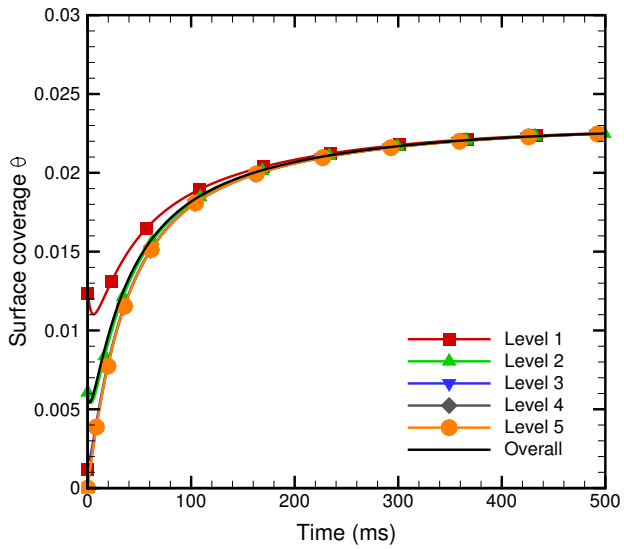

(b)

Figure 4.18 Transient profiles of (a) concentration and (b) adsorption averaged on a per-level basis for the full simulation time for the base simulation

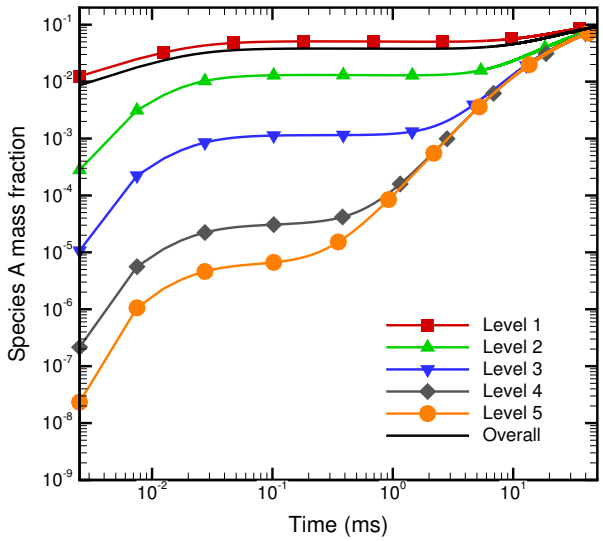

(a)

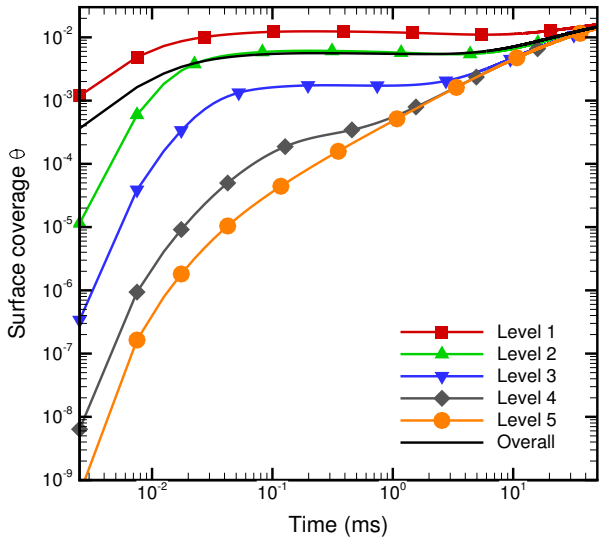

(b)

Figure 4.19 Transient profiles of (a) concentration and (b) adsorption averaged on a per-level basis for the initial 50 ms for the base simulation

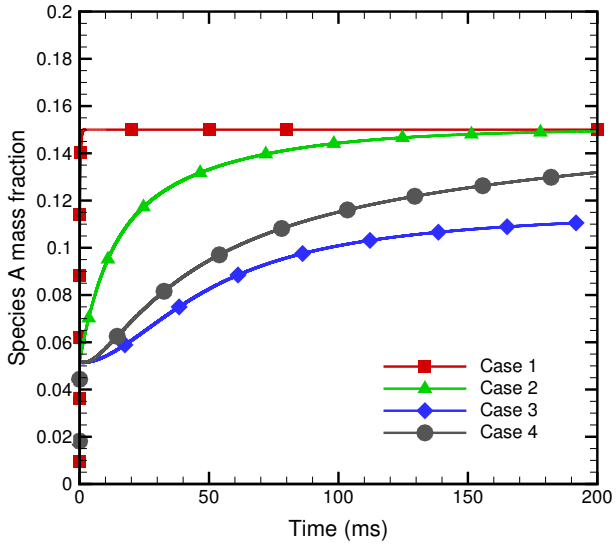

(a)

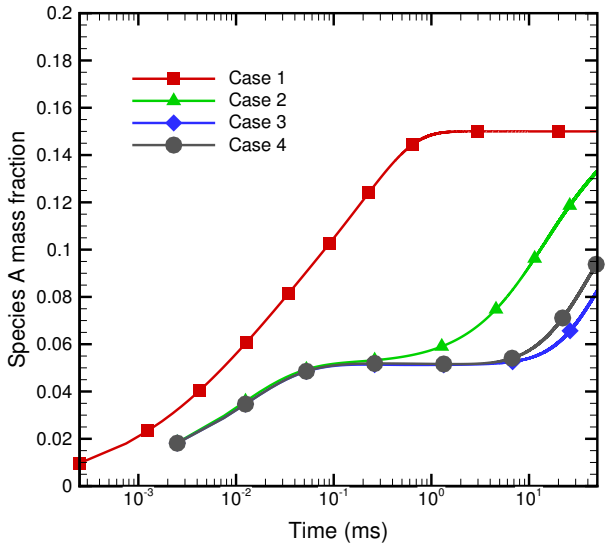

(b)

Figure 4.20 Transient profiles of concentration in the entire particle pore space for simulations with different mechanisms excluded for (a) the full simulation time and (b) the first 50 ms

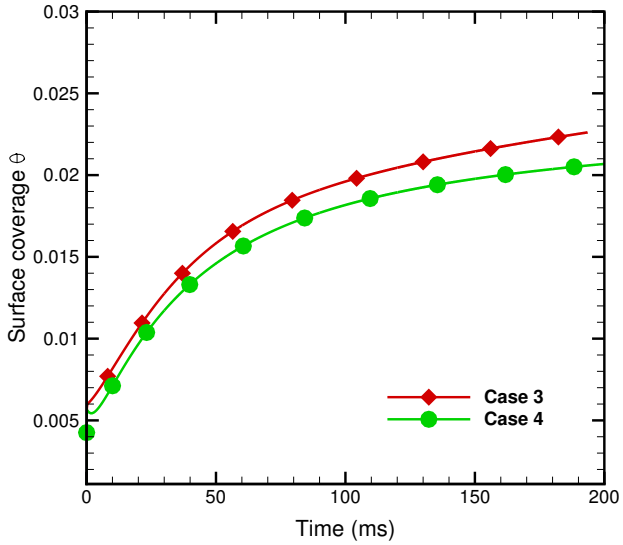

(a)

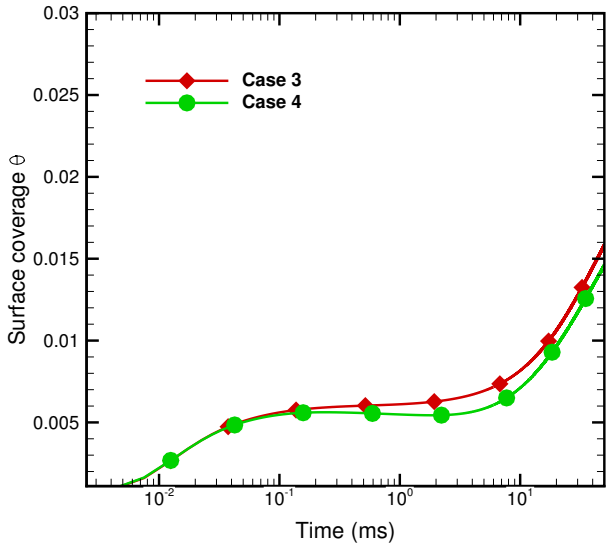

(b)

Figure 4.21 Adsorption profiles obtained for cases 3 and 4 for (a) full simulation time and (b) first 50 ms

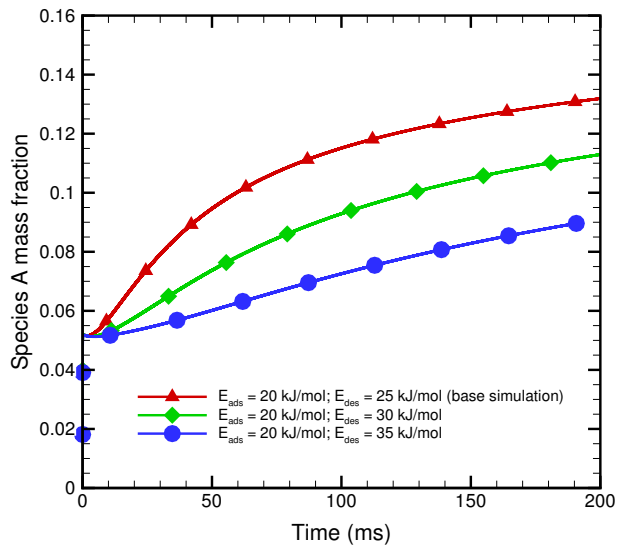

(a)

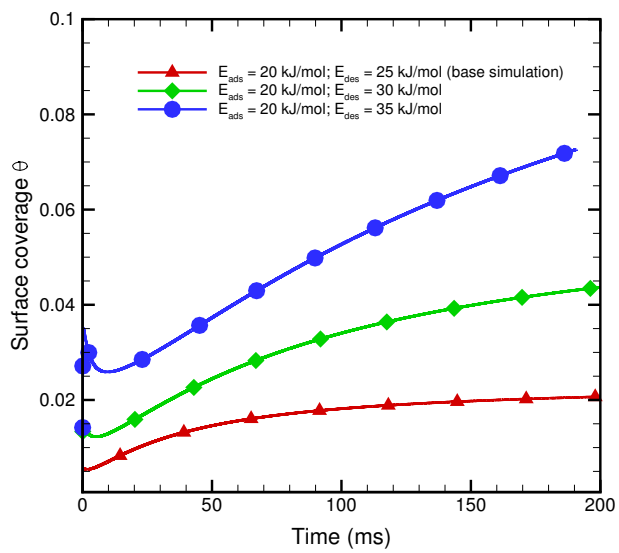

(b)

Figure 4.22 Transient profiles of (a) concentration and (b) adsorption obtained for different values of ΔE

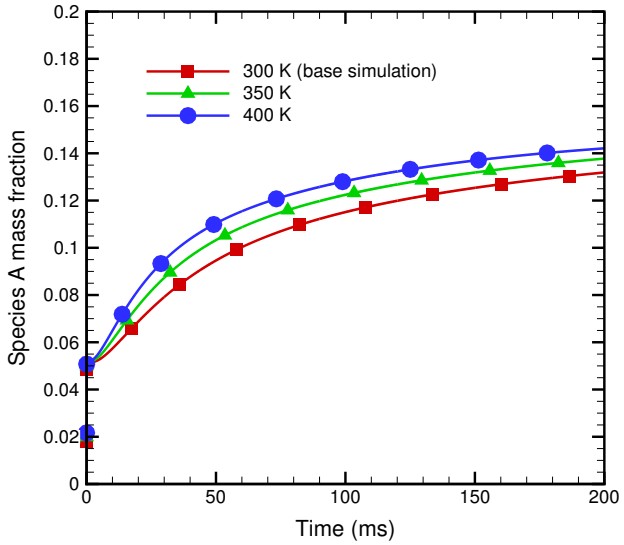

(a)

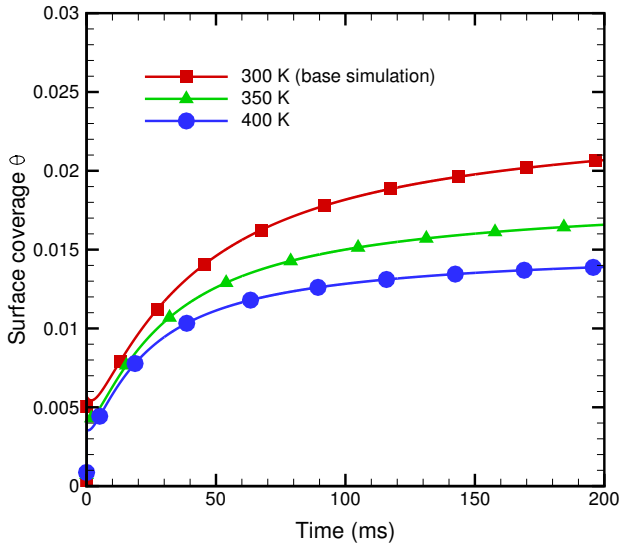

(b)

Figure 4.23 Transient profiles of (a) concentration and (b) adsorption obtained for three different values of ambient temperature

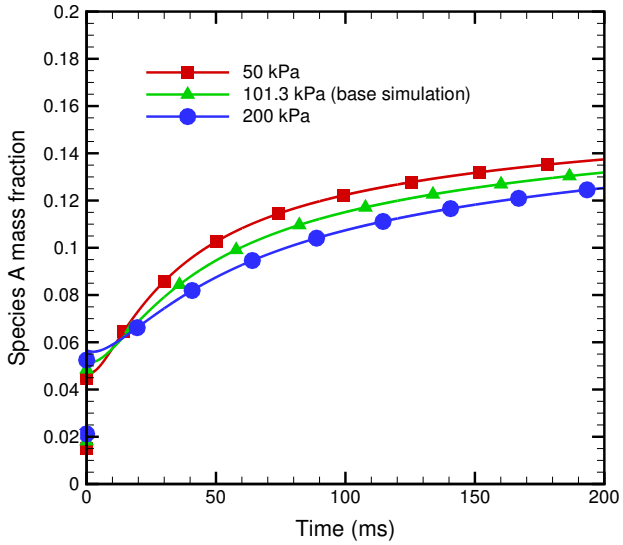

(a)

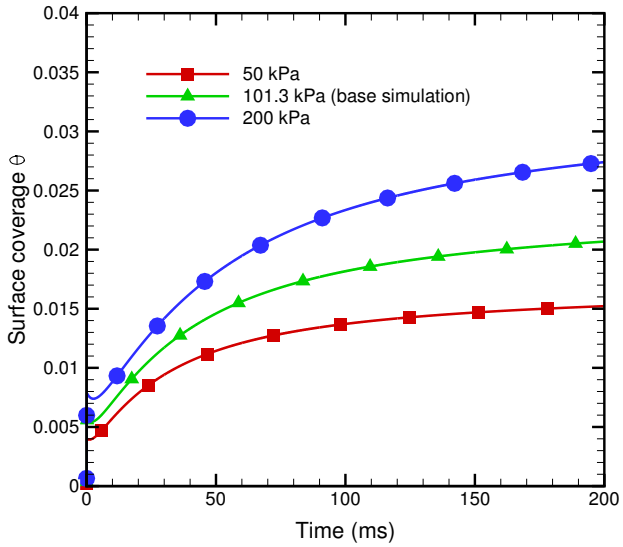

(b)

Figure 4.24 Transient profiles of (a) concentration and (b) adsorption obtained for different values of ambient pressure

Table 4.1 Parameters used for sub-pore geometry creation for the circular porous particle

Quantity	**Value**
Channel size range	100 nm – 4 µm
Number of levels, n_l	5
Number of branches, n_b	5
Specific surface area, A_s	10000 m^2/kg

Table 4.2 Range of simulation parameters used in the different calculations

Quantity	**Value**
Ambient temperature	300-400 K
Ambient pressure	50-200 kPa
Species A mass fraction – ambient	0.15
Species A mass fraction – domain boundaries	0.15
Adsorption activation energy E_{ads}	20-58 kJ/mol
Desorption activation energy E_{des}	25-122 kJ/mol
Entropy of reaction ΔS	-30 J/mol/K
Heat of adsorption	-60 kJ/mol

Table 4.3 Simulation parameters used in the pure diffusion calculation

Quantity	**Value**
Ambient temperature	300 K
Ambient pressure	101.3 kPa
Species A mass fraction – ambient	0.15
Species A mass fraction – domain boundaries	0.15

Table 4.4 Range of simulation parameters used in the pure adsorption calculations

Quantity	**Value**
Ambient temperature	300 K
Ambient pressure	101.3 kPa
Species A mass fraction – ambient	0.15
Adsorption activation energy E_{ads}	20-58 kJ/mol
Desorption activation energy E_{des}	25-122 kJ/mol
Entropy of reaction ΔS	-30 J/mol/K

Table 4.5 Approximate time scales and regimes for different combinations of activation energies

Case	E_{ads} **value (kJ/mol)**	E_{des} **value (kJ/mol)**	**Approx. time scale (ms)**	**Time scale comparison**
A	20	25	10^{-2}	Diffusion-limited
B	35	60	10^{2}	Comparable
C	58	122	10^{6}	Adsorption-limited

Table 4.6 Comparison of saturation times by using extrapolation with the observed values for pure diffusion

Simulation	**Pore space**	**Growth rate $\Delta y_{CO2} / \Delta t$ (in ms^{-1})**	**Extrapolated time to saturation (in ms)**	**Observed time to saturation**
$n_b = 5$	Macro-pores	2.93×10^{-3}	26.1	90.1
	Sub-pores	5.16×10^{-3}	20.1	82.44
	Macro- + sub-pores	4.05×10^{-3}	22.3	85.42
$n_b = 10$	Macro-pores	5.14×10^{-6}	11053.7	-
	Sub-pores	1.52×10^{-5}	7728.9	-
	Macro- + sub-pores	9.00×10^{-6}	8932.4	-

Chapter 5
Summary and Conclusions

The work performed in this dissertation has resulted in development of the numerical tools necessary to model complex heat and mass transfer processes in porous media. In particular, the focus of the current study is on the reaction-diffusion problems involving porous sorbent particles. A characteristic of such problems is the multi-scale and multi-physics nature of the system. A pore channel size based dual approach is proposed to account for the wide range of length scales involved – the larger pore channels, called macro-pores, are resolved using conventional numerical techniques while the smaller unresolved pore channels, called sub-pores, are modeled using a novel sub-pore methodology.

The first part of the dissertation focused on development of simulations tools necessary to account for the macro-pores and the relevant physics at these scales. Though the macro-pores are relatively larger in size, they are composed of an intricate network of porous microstructures and it is a computational challenge to account for such a geometry. An immersed boundary method (IBM) approach is developed for this purpose. IBM is a boundary non-conforming approach which allows significant reduction in grid generation for simulation of flows in and around arbitrarily complex surface contours. The IBM approach is implemented in the non-staggered, curvilinear grid framework of an in-house code GenIDLEST and utilizes efficient algorithms for search, locate and interpolate operations. The implementation also scales very well for large problems showing an efficiency of nearly 80% on 1024 cores. A number of validation and verification simulations are also performed to test the developed framework.

The developed IBM framework is then applied to complex porous media geometries. In order to create surface contours that are representative of the realistic porous media, a stochastic reconstruction procedure is utilized. The reconstruction technique is based on the simulated annealing algorithm and performs randomized pixel swaps till the desired statistical descriptors (the 2-point auto-correlation function, for the examples shown in this work) are satisfied. Simulations are performed through two-

dimensional channels consisting of the porous sections. The pressure drops computed across the porous sections are compared against analytical solutions obtained from Darcy-Forcheimmer equation for a number of porosities and flow velocities. The results agree very well for lower particle Reynolds numbers, but show increased deviations at higher values demonstrating the need for DNS calculations for such flow conditions in porous media. The developed framework is also applied to pure diffusion problems in three-dimensional spherical porous particles and the saturation times are computed for different particle porosities thus demonstrating the capability to perform simulations through complex network of larger 'macro-pore' channels in a relatively straight-forward manner.

In order to account for the unresolved pore channels, a sub-pore modeling methodology is developed in this work. The sub-pores, representing all the smaller channels that are unaccounted for in the macro-pore model, also are composed of intricate network of microstructures. The physical mechanisms important at these smaller scales are taken into account by including the Knudsen effects in the diffusion of mass and energy. The smaller channels also contribute the most to the overall surface area of the porous medium under consideration and hence a reaction kinetics model is included to account for the surface adsorption process. The sub-pore geometry is constructed as a system of hierarchical pores, similar to fractal structures, and is made up of straight cylindrical pore channels. This allows use of one-dimensionality in the governing equations and simplifies the formulations considerably. Source terms are used to couple the diffusion equations with the surface reaction model while an implicit formulation is used to couple the macro-pore and the sub-pore systems thus ensuring conservation.

The entire framework developed, wherein the macro-pores are modeled using IBM while the sub-pores are accounted for by the sub-pore methodology, is then applied to a number of test simulations to demonstrate the applicability in problems of practical interest. Three regimes based on the time scales of individual mechanisms – diffusion and reaction – are determined: (1) diffusion-limited, where adsorption is much faster than diffusion, (2) diffusion and adsorption have comparable time scales and (3)

adsorption-limited, where diffusion is much faster than adsorption. The developed framework is shown to be important for problems in the first two regimes, i.e., when the adsorption is either very fast or is comparable to the diffusion process. The particular problem of CO_2 adsorption in meso-porous silica is determined to be diffusion-limited. Further simulations are performed to explore the system behavior of a model diffusion-limited problem and are followed by parametric studies. It is also demonstrated that the macro-pores can be alternately modeled within the sub-pore system, thus eliminating the need of using IBM for macro-pore modeling completely. Though this implies use of one-dimensionality and the other simplifications used in the development of sub-pore model such as neglecting the convection effects, this is a very attractive option especially for large-scale, low fidelity simulations involving reaction-diffusion systems. For example, in discrete element method (DEM) simulations wherein millions of particles are usually tracked, the sub-pore model developed can be used to completely model the porous microstructures existing inside the particles.

In summary, different computational tools necessary to model general reaction-diffusion systems in complex porous media are developed. The framework is general in nature and can be applied to cases where the entire porous network is modeled using a combination of the macro-pore and sub-pore methodologies or, alternately modeling the entire network either in the sub-pore system or on the hand, directly using the IBM approach.

Bibliography

1. Samanta, A., et al., *Post-combustion CO2 capture using solid sorbents: a review.* Industrial & Engineering Chemistry Research, 2011. **51**(4): p. 1438-1463.
2. Gullett, B. and K. Bruce, *Pore distribution changes of calcium-based sorbents reacting with sulfur dioxide.* AIChE journal, 1987. **33**(10): p. 1719-1726.
3. Punjak, W., M. Uberoi, and F. Shadman, *High-temperature adsorption of alkali vapors on solid sorbents.* AIChE Journal, 1989. **35**(7): p. 1186-1194.
4. Peskin, C.S., *Flow patterns around heart valves: A numerical method.* Journal of Computational Physics, 1972. **10**(2): p. 252-271.
5. Mittal, R. and G. Iaccarino, *Immersed boundary methods.* Annu. Rev. Fluid Mech., 2005. **37**: p. 239-261.
6. Peskin, C.S., *Numerical analysis of blood flow in the heart.* Journal of Computational Physics, 1977. **25**(3): p. 220-252.
7. Lai, M.-C. and C.S. Peskin, *An Immersed Boundary Method with Formal Second-Order Accuracy and Reduced Numerical Viscosity.* Journal of Computational Physics, 2000. **160**(2): p. 705-719.
8. Peskin, C.S., *The immersed boundary method.* Acta Numerica, 2002. **11**: p. 479-517.
9. Mohd-Yusof, J., *Development of immersed boundary methods for complex geometries.* Center for Turbulence Research, Annual Research Briefs, 1998.
10. Fadlun, E.A., et al., *Combined Immersed-Boundary Finite-Difference Methods for Three-Dimensional Complex Flow Simulations.* Journal of Computational Physics, 2000. **161**(1): p. 35-60.
11. Kim, J., D. Kim, and H. Choi, *An Immersed-Boundary Finite-Volume Method for Simulations of Flow in Complex Geometries.* Journal of Computational Physics, 2001. **171**(1): p. 132-150.

12. Gilmanov, A., F. Sotiropoulos, and E. Balaras, *A general reconstruction algorithm for simulating flows with complex 3D immersed boundaries on Cartesian grids.* Journal of Computational Physics, 2003. **191**(2): p. 660-669.

13. Balaras, E., *Modeling complex boundaries using an external force field on fixed Cartesian grids in large-eddy simulations.* Computers & Fluids, 2004. **33**(3): p. 375-404.

14. Gilmanov, A. and F. Sotiropoulos, *A hybrid Cartesian/immersed boundary method for simulating flows with 3D, geometrically complex, moving bodies.* Journal of Computational Physics, 2005. **207**(2): p. 457-492.

15. Udaykumar, H.S., et al., *A Sharp Interface Cartesian Grid Method for Simulating Flows with Complex Moving Boundaries.* Journal of Computational Physics, 2001. **174**(1): p. 345-380.

16. Ye, T., et al., *An Accurate Cartesian Grid Method for Viscous Incompressible Flows with Complex Immersed Boundaries.* Journal of Computational Physics, 1999. **156**(2): p. 209-240.

17. Roman, F., et al., *An improved immersed boundary method for curvilinear grids.* Computers & Fluids, 2009. **38**(8): p. 1510-1527.

18. Gilmanov, A. and S. Acharya, *A computational strategy for simulating heat transfer and flow past deformable objects.* International Journal of Heat and Mass Transfer, 2008. **51**(17-18): p. 4415-4426.

19. Ge, L. and F. Sotiropoulos, *A numerical method for solving the 3D unsteady incompressible Navier–Stokes equations in curvilinear domains with complex immersed boundaries.* Journal of Computational Physics, 2007. **225**(2): p. 1782-1809.

20. Borazjani, I., *Numerical investigation of the hydrodynamics of carangiform swimming in the transitional and inertial flow regimes.* Journal of experimental biology, 2008. **211**(10): p. 1541-1558.

21. Borazjani, I. and F. Sotiropoulos, *Numerical investigation of the hydrodynamics of anguilliform swimming in the transitional and inertial flow regimes.* Journal of Experimental Biology, 2009. **212**(4): p. 576-592.

22. Borazjani, I., L. Ge, and F. Sotiropoulos, *Curvilinear immersed boundary method for simulating fluid structure interaction with complex 3D rigid bodies.* Journal of Computational Physics, 2008. **227**(16): p. 7587-7620.

23. Kim, J. and H. Choi, *An immersed-boundary finite-volume method for simulation of heat transfer in complex geometries.* KSME international journal, 2004. **18**(6): p. 1026-1035.

24. Pacheco, J., et al., *Numerical simulations of heat transfer and fluid flow problems using an immersed-boundary finite-volume method on nonstaggered grids.* Numerical Heat Transfer, Part B: Fundamentals, 2005. **48**(1): p. 1-24.

25. Pan, D., *An immersed boundary method on unstructured Cartesian meshes for incompressible flows with heat transfer.* Numerical Heat Transfer, Part B: Fundamentals, 2006. **49**(3): p. 277-297.

26. Iaccarino, G. and S. Moreau, *Natural and Forced Conjugate Heat Transfer in Complex Geometries on Cartesian Adapted Grids.* Journal of Fluids Engineering, 2006. **128**(4): p. 838-846.

27. Kang, S., G. Iaccarino, and F. Ham, *DNS of buoyancy-dominated turbulent flows on a bluff body using the immersed boundary method.* Journal of Computational Physics, 2009. **228**(9): p. 3189-3208.

28. Tafti, D.K., *GenIDLEST - A scalable parallel computational tool for simulating complex turbulent flows*, in *ASME-FED*2001, Proceedings of the ASME Fluids Engineering Division: New York, NY 10016-5990, United States. p. 347-356.

29. Tafti, D.K., *Time-accurate techniques for turbulent heat transfer analysis in complex geometries*, in *Computational fluid dynamics and heat transfer - Emerging topics*, R.S. Amano and B. Sunden, Editors. 2009.

30. Sewall, E.A. and D.K. Tafti, *A time-accurate variable property algorithm for calculating flows with large temperature variations.* Computers & Fluids, 2008. **37**(1): p. 51-63.

31. Allievi, A. and R. Bermejo, *A generalized particle search–locate algorithm for arbitrary grids.* Journal of Computational Physics, 1997. **132**(2): p. 157-166.

32. Stauffer, D. and A. Aharony, *Introduction to percolation theory*. 1994: CRC press.

33. Kang, S., et al., *Prediction of wall-pressure fluctuation in turbulent flows with an immersed boundary method.* Journal of Computational Physics, 2009. **228**(18): p. 6753-6772.

34. Viswanath, K., et al., *Straight-line climbing flight aerodynamics of a fruit bat.* Physics of Fluids (1994-present), 2014. **26**(2): p. 021901.

35. Borazjani, I., et al., *A parallel overset-curvilinear-immersed boundary framework for simulating complex 3D incompressible flows.* Computers & fluids, 2013. **77**: p. 76-96.

36. Borazjani, I., *Fluid–structure interaction, immersed boundary-finite element method simulations of bio-prosthetic heart valves.* Computer Methods in Applied Mechanics and Engineering, 2013. **257**: p. 103-116.

37. Park, J., K. Kwon, and H. Choi, *Numerical solutions of flow past a circular cylinder at Reynolds numbers up to 160.* Journal of Mechanical Science and Technology, 1998. **12**(6): p. 1200-1205.

38. Dennis, S. and G.-Z. Chang, *Numerical solutions for steady flow past a circular cylinder at Reynolds numbers up to 100.* J. Fluid Mech, 1970. **42**(3): p. 471-489.

39. Lima E. Silva, A.L.F., A. Silveira-Neto, and J.J.R. Damasceno, *Numerical simulation of two-dimensional flows over a circular cylinder using the immersed boundary method.* Journal of Computational Physics, 2003. **189**(2): p. 351-370.

40. Bharti, R.P., R. Chhabra, and V. Eswaran, *A numerical study of the steady forced convection heat transfer from an unconfined circular cylinder.* Heat and mass transfer, 2007. **43**(7): p. 639-648.

41. Lange, C., F. Durst, and M. Breuer, *Momentum and heat transfer from cylinders in laminar crossflow at* $10^{-4} \leqslant Re \leqslant 200$. International Journal of Heat and Mass Transfer, 1998. **41**(22): p. 3409-3430.

42. Leontini, J.S., *Wake state and energy transitions of an oscillating cylinder at low Reynolds number.* Phys. Fluids, 2006. **18**(6): p. 067101.

43. Nonino, C., et al., *Conjugate forced convection and heat conduction in circular microchannels.* International Journal of Heat and Fluid Flow, 2009. **30**(5): p. 823-830.

44. Kays, W.M., M.E. Crawford, and B. Weigand, *Convective heat and mass transfer*. Vol. 3. 1993: McGraw-Hill New York.

45. Philip, J.R., *Flow in Porous Media.* Annual Review of Fluid Mechanics, 1970. **2**(1): p. 177-204.

46. Zick, A.A. and G.M. Homsy, *Stokes flow through periodic arrays of spheres.* Journal of Fluid Mechanics, 1982. **115**: p. 13-26.

47. Rahimian, M.H. and A. Pourshaghaghy, *Direct simulation of forced convection flow in a parallel plate channel filled with porous media.* International Communications in Heat and Mass Transfer, 2002. **29**(6): p. 867-878.

48. Morais, A.F., et al., *Non-Newtonian Fluid Flow through Three-Dimensional Disordered Porous Media.* Physical Review Letters, 2009. **103**(19): p. 194502.

49. Hill, R.J., D.L. Koch, and A.J.C. Ladd, *The first effects of fluid inertia on flows in ordered and random arrays of spheres.* Journal of Fluid Mechanics, 2001. **448**(2): p. 213-241.

50. Smolarkiewicz, P.K. and C. Larrabee Winter, *Pores resolving simulation of Darcy flows.* Journal of Computational Physics, 2010. **229**(9): p. 3121-3133.

51. Ovaysi, S. and M. Piri, *Direct pore-level modeling of incompressible fluid flow in porous media.* Journal of Computational Physics, 2010. **229**(19): p. 7456-7476.

52. Andrade, J.S., Jr., et al., *Inertial Effects on Fluid Flow through Disordered Porous Media.* Physical Review Letters, 1999. **82**(26): p. 5249-5252.

53. Jaganathan, S., H. Vahedi Tafreshi, and B. Pourdeyhimi, *A realistic approach for modeling permeability of fibrous media: 3-D imaging coupled with CFD simulation.* Chemical Engineering Science, 2008. **63**(1): p. 244-252.

54. Li, H., C. Pan, and C.T. Miller, *Pore-scale investigation of viscous coupling effects for two-phase flow in porous media.* Physical Review E, 2005. **72**(2): p. 026705.

55. Zhao, C.-Y., et al., *Numerical study of natural convection in porous media (metals) using Lattice Boltzmann Method (LBM).* International Journal of Heat and Fluid Flow, 2010. **31**(5): p. 925-934.

56. Ovaysi, S. and M. Piri, *Pore-scale modeling of dispersion in disordered porous media.* Journal of contaminant hydrology, 2011. **124**(1): p. 68-81.

57. Malico, I. and P.J.F. de Sousa, *Modeling the pore level fluid flow in porous media using the immersed boundary method*, in *Numerical Analysis of Heat and Mass Transfer in Porous Media*. 2012, Springer. p. 229-251.

58. Zaretskiy, Y., et al., *Efficient flow and transport simulations in reconstructed 3D pore geometries.* Advances in Water Resources, 2010. **33**(12): p. 1508-1516.

59. Adler, P.M., C.G. Jacquin, and J.A. Quiblier, *Flow in simulated porous media.* International Journal of Multiphase Flow, 1990. **16**(4): p. 691-712.

60. Yeong, C.L.Y. and S. Torquato, *Reconstructing random media.* Physical Review E, 1998. **57**(1): p. 495-506.

61. Yeong, C.L.Y. and S. Torquato, *Reconstructing random media. II. Three-dimensional media from two-dimensional cuts.* Physical Review E, 1998. **58**(1): p. 224-233.

62. Politis, M.G., et al., *A hybrid process-based and stochastic reconstruction method of porous media.* Microporous and Mesoporous Materials, 2008. **110**(1): p. 92-99.

63. Mittal, R. and G. Iaccarino, *Immersed boundary methods*, in *Annual Review of Fluid Mechanics*. 2005, Annual Reviews: Palo Alto. p. 239-261.

64. Torquato, S., *Statistical description of microstructures.* Annual review of materials research, 2002. **32**(1): p. 77-111.

65. Čapek, P., et al., *Stochastic reconstruction of particulate media using simulated annealing: improving pore connectivity.* Transport in Porous Media, 2009. **76**(2): p. 179-198.

66. Norberg, C., *An experimental investigation of the flow around a circular cylinder: influence of aspect ratio.* Journal of Fluid Mechanics, 1994. **258**: p. 287-316.

67. Zhang, H.-Q., et al., *On the transition of the cylinder wake.* Physics of Fluids, 1995. **7**(4): p. 779-794.

68. Barkley, D. and R.D. Henderson, *Three-dimensional Floquet stability analysis of the wake of a circular cylinder.* Journal of Fluid Mechanics, 1996. **322**: p. 215-241.

69. Poulikakos, D. and K. Renken, *Forced convection in a channel filled with porous medium, including the effects of flow inertia, variable porosity, and Brinkman friction.* Journal of Heat Transfer, 1987. **109**(4): p. 880-888.

70. Thies-Weesie, D.M.E. and A.P. Philipse, *Liquid Permeation of Bidisperse Colloidal Hard-Sphere Packings and the Kozeny-Carman Scaling Relation.* Journal of Colloid and Interface Science, 1994. **162**(2): p. 470-480.

71. Adler, P.M., *Fractal porous media III: Transversal Stokes flow through random and Sierpinski carpets.* Transport in Porous Media, 1988. **3**(2): p. 185-198.

72. Zeng, Z. and R. Grigg, *A Criterion for Non-Darcy Flow in Porous Media.* Transport in Porous Media, 2006. **63**(1): p. 57-69.

73. Larson, R. and J. Higdon, *Microscopic flow near the surface of two-dimensional porous media. Part 2. Transverse flow.* Journal of Fluid Mechanics, 1987. **178**(1): p. 119-136.

74. Koch, D.L. and A.J.C. Ladd, *Moderate Reynolds number flows through periodic and random arrays of aligned cylinders.* Journal of Fluid Mechanics, 1997. **349**: p. 31-66.

75. Ruthven, D.M., *Principles of adsorption and adsorption processes*. 1984, New York: Wiley.

76. Do Duong, D., *Adsorption analysis: equilibria and kinetics*. Vol. 2. 1998: Imperial College Press.

77. Smit, B. and T.L. Maesen, *Molecular simulations of zeolites: adsorption, diffusion, and shape selectivity.* Chemical reviews, 2008. **108**(10): p. 4125-4184.

78. James, S.L., *Metal-organic frameworks.* Chemical Society Reviews, 2003. **32**(5): p. 276-288.

79. Yang, H., et al., *Progress in carbon dioxide separation and capture: A review.* Journal of Environmental Sciences, 2008. **20**(1): p. 14-27.

80. Li, J.-R., et al., *Carbon dioxide capture-related gas adsorption and separation in metal-organic frameworks.* Coordination Chemistry Reviews, 2011. **255**(15–16): p. 1791-1823.

81. Sumida, K., et al., *Carbon dioxide capture in metal–organic frameworks.* Chemical reviews, 2011. **112**(2): p. 724-781.

82. Ropp, D.L., J.N. Shadid, and C.C. Ober, *Studies of the accuracy of time integration methods for reaction–diffusion equations.* Journal of Computational Physics, 2004. **194**(2): p. 544-574.

83. Hundsdorfer, W. and J.G. Verwer, *Numerical solution of time-dependent advection-diffusion-reaction equations*. Vol. 33. 2003: Springer.

84. Knoll, D.A., et al., *On balanced approximations for time integration of multiple time scale systems.* Journal of Computational Physics, 2003. **185**(2): p. 583-611.

85. Simons, G.A., *Char Gasification: Part I. Transport Model.* Combustion Science and Technology, 1979. **20**(3-4): p. 107-116.

86. Dullien, F.A., *Porous media: fluid transport and pore structure*. 1991: Academic press.

87. Thiele, E., *Relation between catalytic activity and size of particle.* Industrial & Engineering Chemistry, 1939. **31**(7): p. 916-920.

88. Wheeler, A., *Reaction rates and selectivity in catalyst pores.* Advances in Catalysis, 1951. **3**(5): p. 433-439.

89. Johnson, M.F. and W.E. Stewart, *Pore structure and gaseous diffusion in solid catalysts.* Journal of Catalysis, 1965. **4**(2): p. 248-252.

90. Feng, C. and W.E. Stewart, *Practical models for isothermal diffusion and flow of gases in porous solids.* Industrial & Engineering Chemistry Fundamentals, 1973. **12**(2): p. 143-147.

91. Simons, G.A. and M.L. Finson, *The Structure of Coal Char: Part I—Pore Branching.* Combustion Science and Technology, 1979. **19**(5-6): p. 217-225.

92. Simons, G.A. *The pore tree structure of porous char*. in *Symposium (International) on Combustion*. 1982. Elsevier.

93. Yu, B., *Analysis of flow in fractal porous media.* Applied Mechanics Reviews, 2008. **61**(5): p. 050801.

94. Yu, B. and J. Li, *Some fractal characters of porous media.* Fractals, 2001. **9**(03): p. 365-372.

95. Nagendra, K., D.K. Tafti, and K. Viswanath, *A new approach for conjugate heat transfer problems using immersed boundary method for curvilinear grid based solvers.* Journal of Computational Physics, 2014. **267**(0): p. 225-246.

96. Nagendra, K. and D.K. Tafti, *Flows Through Reconstructed Porous Media Using Immersed Boundary Methods.* Journal of Fluids Engineering, 2014. **136**(4): p. 040908.

97. White, F.M. and I. Corfield, *Viscous fluid flow*. Vol. 2. 1991: McGraw-Hill New York.

98. Chapman, S. and T.G. Cowling, *The mathematical theory of non-uniform gases: an account of the kinetic theory of viscosity, thermal conduction and diffusion in gases*. 1970: Cambridge university press.

99. Youngquist, G.R., *SYMPOSIUM ON FLOW THROUGH POROUS MEDIA Diffusion and Flow of Gases in Porous Solids.* Industrial & Engineering Chemistry, 1970. **62**(8): p. 52-63.

100. Kärger, J., D.M. Ruthven, and D.N. Theodorou, *Diffusion in nanoporous materials*. 2012: John Wiley & Sons.

101. Zhang, Z.M., *Nano/microscale heat transfer*. 2007: McGraw-Hill New York.

102. Ferkl, P., et al., *Heat transfer in one-dimensional micro-and nano-cellular foams.* Chemical Engineering Science, 2013. **97**: p. 50-58.

103. Arkilic, E.B., K.S. Breuer, and M.A. Schmidt, *Mass flow and tangential momentum accommodation in silicon micromachined channels.* Journal of Fluid Mechanics, 2001. **437**: p. 29-43.

104. Barnes, G. and I. Gentle, *Interfacial science: an introduction*. 2011: Oxford University Press.

105. Kolasinski, K.K., *Surface science: foundations of catalysis and nanoscience*. 2012: John Wiley & Sons.

106. Lee, A., et al., *A model for the adsorption kinetics of CO2 on amine-impregnated mesoporous sorbents in the presence of water*, in *Pittsburgh Coal Conference*2011: Pittsburgh.